Statistical Uncertainty Analysis for Image Processing Algorithms in Metric Vision Systems

Doctoral Thesis

Ewald Fauster

Institute for Automation
Department Product Engineering
University of Leoben
Leoben, Austria

March, 2008

Supervisors:

O.Univ.-Prof. Dipl.-Ing. Dr.techn. Paul O'Leary
University of Leoben, Austria

Ao.Univ.-Prof. Mag.rer.nat. Dr.techn. Anton Gfrerrer
Graz University of Technology, Austria

Dedicated to my grandfather,
Peter Fauster.

I declare in lieu of oath, that I wrote this thesis and performed the associated research myself, using only literature cited in this volume.

Leoben, March 2008 Ewald Fauster

Acknowledgements

First of all, I would like to thank Prof. Paul O'Leary for the possibility to compose this thesis and for his support throughout the years at the Institute for Automation. Secondly, I owe special thanks to Prof. Anton Gfrerrer for becoming the co-supervisor of the thesis and for his valuable contributions to this work.

I am especially grateful to Peter Schalk for the thousands of fruitful and entertaining discussions and the pleasurable working atmosphere in our office.

Moreover, I would like to thank the team at the Institute for Automation, Doris Widek, Beate Oswald, Matthew Harker, Ronald Ofner, Gerold Probst, Gerhard Rath, Mario Sorger and Gernot Wally as well as my former colleagues Norbert Koller, Ingo Reindl, Michael Reiter, Christian Sallinger and Mark Tratnig for their great support and the countless small things, which are always of inestimable value.

Parts of the research work for this thesis were performed at the Polymer Competence Center Leoben GmbH (PCCL, Austria) within the framework of the K_{plus}-program of the Austrian Ministry of Traffic, Innovation and Technology. The PCCL is funded by the Austrian Government and the State Governments of Styria and Upper Austria.

I would like to express my gratitude to my former project leader, Zoltan Major, as well as my former colleagues at the PCCL, Michael Jerabek and Robin Steinberger.

I am deeply grateful to my parents for having let me go the path I have chosen and for supporting me all the time. I would also like to thank my brother Manfred and my sisters, Karin and Barbara, for contributing to where I stand now.

After all, I wish to express my gratitude to Katharina for her great mental support, for her trust in my abilities and for untiringly encouraging me during the last months. You are the inspiration for my life.

Abstract

The work presented in this thesis addresses image processing algorithms as well as methods of statistical uncertainty analysis related to metric vision systems.

The term *metric vision* covers the optical measurement of quantitative information for geometric objects, such as position, orientation, dimensions and shape. Thereby, three tasks are of particular interest: (1) estimation of plane-to-plane homographies based on point correspondences, (2) fitting of geometric models to sets of data points perturbed by measurement noise, and (3) derivation of measurement results from the model parameters.

In order to specify the uncertainty associated with the measurement results of metric vision systems, two different methods of uncertainty analysis are investigated: a statistical and an analytical approach. The statistical method is based on evaluating data of repeated but independent measurements, whereby the analytical estimates are computed by application of the law of first order error propagation to the particular steps of the evaluation procedure.

In the present work, the algorithms for fitting lines as well as pairs of parallel lines to sets of noisy data points are analyzed in detail concerning first order estimation of error propagation. Furthermore, the direct linear transformation (DLT) algorithm for computing the parameters of plane-to-plane homographies based on point correspondences is analyzed. All of the analytically computed uncertainty estimates are numerically verified with Monte-Carlo simulations.

The methods of statistical uncertainty analysis described in this thesis are of general validity for metric vision systems. In order to illustrate the applicability of the approaches, the image processing algorithms of a video-extensometer system are examined. The system is designed to measure the deformation of polymer materials during tensile testing. The images acquired during the tests are evaluated offline. At first, points of interest are extracted using gradient-based techniques followed by center-of-gravity calculation. As a result, sets of data points are obtained at sub-pixel accuracy. Linear geometric models, concretely lines as well as pairs of parallel lines, are approximated to the sets of noisy data points by means of least-squares estimation of the model parameters. The measurement results, in particular the longitudinal as well as the transversal specimen dimensions, are derived from the fitted geometric models.

Kurzfassung

Die hier präsentierte Arbeit befasst sich mit Auswertungsalgorithmen sowie Methoden der statistischen Unsicherheitsanalyse von metrischen Bildverarbeitungssystemen.

Mit dem Begriff der *metrischen Bildverarbeitung* wird die Messung quantitativer Informationen von geometrischen Objekten, wie Position, Orientierung, Dimensionen und Form, bezeichnet. Dabei sind drei Aufgaben von besonderem Interesse: (1) die Ermittlung der Parameter von Homographien auf Basis von Punktkorrespondenzen, (2) die Anpassung von geometrischen Modellen an Sätze verrauschter Datenpunkten, und (3) die Ableitung von Messergebnissen aus den Modellparametern.

Zur Angabe der zu den Ergebnissen von metrischen Bildverarbeitungssystemen gehörenden Unsicherheit werden zwei Methoden der Unsicherheitsanalyse untersucht: ein statistischer und ein analytischer Ansatz. Die statistische Methode basiert auf der Auswertung von unabhängigen Wiederholungsmessungen, die analytische Abschätzung erfolgt über die Anwendung des Gesetzes der Fehlerfortpflanzung erster Ordnung auf die einzelnen Schritte des Auswertealgorithmus.

In der vorliegenden Arbeit werden die Algorithmen zur Anpassung von Geraden sowie Paare parelleler Geraden an Sätze von verrauschten Datenpunkten hinsichtlich Fehlerfortpflanzung erster Ordnung detailliert analysiert. Weiters wird der DLT Algorithmus zur Bestimmung von Homographieparametern auf Basis von Punktkorrespondenzen untersucht. Alle analytisch berechneten Unsicherheitsabschätzungen werden anhand von Monte-Carlo Simulationen numerisch verifiziert.

Die in dieser Arbeit beschriebenen Methoden der statischen Unsicherheitsanalyse sind von allgemeiner Gültigkeit für metrische Bildverarbeitungssysteme. Um die Anwendbarkeit dieser Ansätze zu veranschaulichen wurden die Bildverarbeitungsalgorithmen eines Video-Extensometer Systems untersucht. Das System ist für die Messung der Deformation von Kunststoffmaterialien bei Zugversuchen ausgelegt. Die während der Versuche aufgenommenen Bilder werden offline ausgewertet. Zunächst werden Datenpunkte mittels gradienten-basierten Methoden und anschließender Berechnung von Intensitätsschwerpunkten ermittelt. Damit werden Sätze von Datenpunkte mit Subpixel-Genauigkeit gewonnen. Lineare geometrische Modelle, konkret Geraden sowie Paare von parellelen Geraden, werden an die Sätze verrauschter Datenpunkte mittels Verfahren der kleinsten Fehlerquadrate angepasst. Die Messergebnisse, speziell die longitudinale und transversale Prüfkörperdeformation, werden schließlich aus den Parametern der approximierten geometrischen Modelle abgeleitet.

Symbols and Notations

Notation of probability density functions:

$\mathcal{P}(x, \mu_x, \sigma_x)$	general notation of a univariate probability density function
$\mathcal{N}(x, \mu_x, \sigma_x)$	a univariate Gaussian (normal) probability density function
$\mathcal{P}(\boldsymbol{x}, \boldsymbol{\mu}_{\boldsymbol{x}}, \Lambda_{\boldsymbol{x}})$	general notation of a multivariate probability density function
$\mathcal{N}(\boldsymbol{x}, \boldsymbol{\mu}_{\boldsymbol{x}}, \Lambda_{\boldsymbol{x}})$	a multivariate Gaussian (normal) probability density function

Symbols used in uncertainty analysis:

$\mathrm{E}(f(x))$	the expectation value of a function $f(x)$
$\mathrm{V}(f(x))$	the variance of a function $f(x)$
μ_x	notation of a sample mean value
σ_x, σ_x^2	notation of sample standard deviation value and sample variance
$\boldsymbol{\mu}$	a sample mean vector, i.e. a vector of mean values
Λ	a covariance matrix

Notations arising for Taylor series expansions:

$\mathrm{T}_n(f(\boldsymbol{x}))$	an n'th order Taylor series expansion for a function $f(\boldsymbol{x})$
$\mathrm{R}_n(f(\boldsymbol{x}))$	the remainder term associated with a Taylor series $\mathrm{T}_n(f(\boldsymbol{x}))$
J	a Jacobian matrix, i.e. a matrix of first order partial derivatives
H	a Hessian matrix, i.e. a matrix of second order partial derivatives

Symbols concerning matrix decompositions:

Ω	matrix square root
G	triangular matrix representing the result of a Cholesky decomposition
V, D	components of an eigen-decomposition
U, S, V	components of a singular value decomposition

Matrix symbols for linear transformations of the projective plane:

T	matrix representing a translational transformation
R	matrix representing a rotational transformation
H	matrix representing a general homography

Table of Contents

Acknowledgements iii

Abstract iv

Kurzfassung v

Symbols and Notations vi

Table of Contents vii

I Introduction and Basic Principles 1

1 Introduction 2
1.1 Outline of the Thesis . . . 4
1.2 Original Work . . . 5

2 Basics of Statistics and Measurement Uncertainty 6
2.1 Definitions of Basic Statistical Terms . . . 6
2.1.1 Random Variables . . . 6
2.1.2 Random Vectors . . . 9
2.1.3 Gaussian Distributions . . . 10
2.2 Basics of Measurement Accuracy and Uncertainty . . . 12
2.2.1 The True Value of a Measurement . . . 12
2.2.2 Measurement Accuracy, Precision and Trueness . . . 12
2.3 Analysis of Measurement Uncertainty . . . 13
2.3.1 The Statistical Approach . . . 14
2.3.2 Computation of Multivariate Random Data . . . 15
2.3.3 The Analytical Approach . . . 17

3 Representation of Uncertain Geometric Primitives 20
3.1 Planar Projective Geometry . . . 20
3.1.1 Representation of Points . . . 21
3.1.2 Representation of Lines . . . 21

3.1.3 Interrelations of Special Line Pairs . . . 23
3.1.4 The Duality Principle of the Projective Plane . . . 24
3.1.5 Representation of Conics . . . 25
3.2 Uncertainty associated with Geometric Primitives . . . 29
3.2.1 The Covariance Matrix of a Point . . . 29
3.2.2 The Covariance Matrix of a Line . . . 30
3.3 Visualization of Uncertain Geometric Primitives . . . 31
3.3.1 Points and Lines of the Affine Plane . . . 31
3.3.2 Points and Hyperplanes in n Dimensions . . . 33
3.3.3 Plotting Confidence Envelopes of Planar Points and Lines . . . 34

II Uncertainty Analysis of Metric Vision Tasks 35

4 Fitting of Linear Geometric Models 36
4.1 Fitting a Line to a Set of Uncertain Data Points . . . 37
4.1.1 The Fitting Algorithm . . . 37
4.1.2 First Order Error Propagation for the Fitting Algorithm . . . 38
4.1.3 Error Propagation for Derived Quantities . . . 42
4.1.4 Numerical Verification . . . 43
4.2 Fitting a Pair of Parallel Lines to two Sets of Uncertain Data Points . . . 47
4.2.1 The Fitting Algorithm . . . 47
4.2.2 First Order Error Propagation for the Fitting Algorithm . . . 49
4.2.3 Error Propagation for Derived Quantities . . . 52
4.2.4 Numerical Verification . . . 54

5 Geometric Transformations of the Projective Plane 57
5.1 Estimation of Plane-to-Plane Homographies . . . 58
5.1.1 The Direct Linear Transformation Algorithm . . . 58
5.1.2 First Order Error Propagation for the DLT Algorithm . . . 59
5.1.3 First Order Error Propagation for a Point Transformation . . . 62
5.1.4 Numerical Verification . . . 63

6 First Order Error Propagation for Non-Linear Functions 68
6.1 The Approximation Error in Results of First Order Error Propagation . . . 69
6.1.1 Nature and Statistical Model of the Uncertain Input Data . . . 69
6.1.2 Taylor Series Expansion . . . 70
6.1.3 The Confidence Interval Associated with First Order Estimates of Error Propagation . . . 71
6.2 Analysis of Non-Linear Functions . . . 73
6.2.1 The Euclidean Distance between two Uncertain Points . . . 73
6.2.2 Numerical Verification . . . 78

6.2.3 Computation of Inhomogeneous Point Coordinates . . . 79
6.2.4 The Variance of an Inhomogeneous Point Coordinate . . . 81
6.2.5 The Covariance of two Inhomogeneous Point Coordinates . . . 82
6.2.6 Numerical Verification . . . 85
6.3 Summary . . . 86

III Application and Conclusion **87**

7 A Video-Extensometer System for Tensile Testing **88**
7.1 Image Acquisition Setup and Configurations . . . 89
7.1.1 Acquisition Configurations . . . 90
7.2 Evaluation Algorithm . . . 91
7.2.1 Extracting the Sets of Data Points . . . 92
7.2.2 Rectification of the Data Points . . . 94
7.2.3 Computation of the Specimen Dimensions . . . 96
7.2.4 Derivation of the Strain Characteristics . . . 97
7.2.5 Exemplary Measurement Results . . . 97
7.3 Derivation of the Measurement Accuracy . . . 98
7.3.1 Monte-Carlo Simulations . . . 99
7.3.2 First Order Estimation of Error Propagation . . . 101
7.3.3 The High-Resolution Configuration . . . 101
7.3.4 Computation of Strain Values . . . 102
7.4 Conclusions . . . 103

8 Summary, Conclusions and Future Work **104**
8.1 Summary . . . 104
8.2 Conclusions . . . 105
8.3 Future Work . . . 105

Appendix **107**

A Derivation of Statistical Quantities **107**
A.1 Variance and Covariance . . . 107
A.2 Covariance Matrix . . . 107
A.3 Sample Variance and Sample Covariance . . . 108
A.4 Sample Covariance Matrix . . . 109

B Algebraic and Central Moments **110**
B.1 The First Algebraic Moment . . . 110
B.2 The Second Central Moment . . . 111

B.3 The Third Central Moment 111
B.4 The Fourth Central Moment 112

C The Pseudo-Inverse Matrix **113**

List of Figures **116**

List of Tables **118**

Author's Publications **119**

References **121**

Part I

Introduction and Basic Principles

Chapter 1

Introduction

Metric vision systems are designed to measure quantitative information of geometric objects based on optical measurement approaches. Thereby, the measurement results are obtained by application of digital image processing techniques.

In fact, a measurement result is incomplete, if there is no specification of the error associated with it. The DIN 55350 standard states that measurement accuracy comprises two criteria: precision and trueness. The term precision specifies the ability of a measurement system to indicate a particular value (not necessarily the true value) upon repeated but independent measurement of a specific quantity. Thus, the random deviation of a measurement sample with respect to the sample mean is called the *precision error*.

By contrast, trueness refers to the accordance of the average sample value indicated by the measurement system with the true value of the measurand. Any deviation of the average value indicated by the measurement system from the true value must be considered to be systematic and is termed *bias error*.

The discipline *uncertainty analysis* solely addresses statistical deviations. Systematic influences on a measurement should be avoided in principle. If this cannot be achieved, appropriate correction techniques are to be applied [20].

In this work, two methods for estimating measurement uncertainty are examined: a statistical and an analytical approach. The statistical method is based on evaluating either data acquired from repeated but independent measurements, i.e. real measurement data, or synthetically generated data. By contrast, the analytical approach is based on successive application of the law of first order error propagation to the particular steps of the evaluation algorithms.

Two problems typically arising in metric vision systems are investigated in detail concerning statistical as well as analytical estimation of error propagation: (1) fitting of lines as well as parallel lines to sets of noisy data points; and (2) computation of plane-to-plane homographies based on point correspondences. The analytically computed uncertainty estimates are numerically verified with Monte-Carlo simulations.

The motivation for this work has arisen from the need for contactless methods for the measurement of polymer materials during tensile testing. Typically implemented approaches for measuring the deformation of the samples under test are considered unsuitable:

- measurement of the testing machine's crosshead motion is error-prone, as the specimen deformation is superimposed by the resilience of the clamping and charging construction;
- the operation of strain gauges for measuring large series of samples is impractical due to the laborious specimen instrumentation;
- mechanical extensometer systems are to be applied directly onto the specimen and therefore influence the characteristics of the material under test.

As a result, contact-free deformation measurement approaches are desirable. In this context, there are two types of measurement systems to be distinguished: (1) systems for measuring global material characteristics; and (2) systems capable of measuring full-field deformations.

Global tensile properties can be measured by means of video-extensometer systems or laser extensometer systems. Video-extensometer systems are commonly offered as an extension of the equipment of testing machines [4, 5], but scientific considerations on evaluation algorithms as well as measurement accuracy are barely to find.

The measurement principle of laser extensometers is based on the diverse reflectivity of the specimen surface and the measurement marks applied to the material [2, 14]. These systems are inflexible compared to video-extensometer systems with respect to the diversity of evaluation possibilities at measurements on modern testing machines.

Full-field deformation measurement is commonly addressed with digital image correlation systems or laser speckle interferometers [1, 3, 6]. Digital image correlation systems require a stochastic colour pattern to be applied to the surface of the material. Deformation of the material causes variation of the colour pattern. The deformation distribution is determined by evaluating the images acquired during the test by means of image correlation techniques.

Laser speckle interferometers exploit the speckle effect caused by coherent laser light projected onto the optically rough surface of the samples under test. Deformation of the material leads to phase changes of the laser light reflected by the surface. The deformation of the specimen is measured by evaluating these phase variations. As a result of the high sensitivity inherent to the measurement principle, the application of laser speckle interferometers is restricted to very small specimen deformations.

In this thesis, a video-extensometer system is presented, that is capable of measuring the full 3-dimensional deformation of the samples under test. The system is flexible with respect to the application to different types of specimen and material properties. Particular interest is laid on uncertainty analyses concerning the digital image processing algorithms for evaluating the images acquired during the tensile tests. Furthermore, the measurement uncertainty associated with the results obtained by the video-extensometer system is derived.

1.1 Outline of the Thesis

The thesis is structured in three parts. In the first part, statistical basics as well as geometric primitives together with their associated uncertainties are introduced. The second part comprises three chapters focussing on typical problems arising in metric vision tasks. The last part of the thesis addresses the application of the video-extensometer system to tensile testing of polymer material.

Part I:
At the beginning of Chapter 2, statistical basics essential for understanding the principles and tools presented in the course of the thesis are recalled. Furthermore, the term *measurement uncertainty* is specified and two basic principles for analyzing measurement uncertainty - a statistical and an analytical approach - are presented.

Points, lines and conics - representing the most basic geometric primitives - are described in Chapter 3 within the context of *planar projective geometry*. Subsequently, the covariance matrices of points and lines are discussed, as they provide a means to describe the uncertainty associated with these geometric objects. Moreover, algorithms required to visualize confidence envelopes of points and lines are derived.

Part II:
The uncertainty of lines as well as pairs of parallel lines fitted to sets of noisy data points is addressed in Chapter 4. The fitting algorithms are presented, followed by numerical as well as analytical uncertainty analyses for the particular steps of the fitting procedures.

In Chapter 5, the *direct linear transformation* (DLT) algorithm for estimating plane-to-plane homographies is treated. After a brief derivation of the algorithm, a procedure for computing the first order estimate of the uncertainty associated with the homography parameters is presented. The analytical results are numerically verified by Monte-Carlo simulations.

The error inherent to first order estimates of the uncertainty associated with outcomes of non-linear functions, such as the computation of the Euclidean distance between two points, is investigated in Chapter 6. A procedure for analytically computing the approximation error associated with these first order estimates is presented. The approach is based on the definition of Lagrange remainder terms associated with Taylor series truncated after the first order terms.

Part III:
In Chapter 7, the video-extensometer system is presented. At first, the hardware setup as well as the acquisition configurations of the measurement system are outlined. Furthermore, the evaluation algorithms are described and a number of uncertainty analyses are presented. Thereby, the measurement accuracy achievable with the particular acquisition configurations of the video-extensometer system is derived by analysis of repeated measurements as well as analytic estimations based on the law of first order error propagation.

1.2 Original Work

Aside from the development of the video-extensometer measurement system, the original contributions of the work presented in this thesis are related with the determination of measurement uncertainty:

1. The uncertainty analyses undertaken in this thesis are all based on sets of data points extracted from images acquired with the video-extensometer system. It is shown by means of Monte-Carlo simulations, that the covariances between the particular data points are to be incorporated for the uncertainty analyses. As a result, fully occupied covariance matrices are determined from the sets of data points extracted in the acquired images. These are then propagated to the uncertainty associated with the results of the particular evaluation procedures.

2. A procedure for analytically estimating the uncertainty (in terms of covariance matrices) associated with a line as well as a pair of parallel lines fitted to sets of noisy data points is presented. Therein, any possibly existing covariances between the data points are taken into account by incorporating fully occupied covariances matrices associated with the sets of data points.

3. The computation of plane-to-plane homographies based on point correspondences is investigated concerning first order error propagation. An analytical estimation of the covariance matrix associated with the homography parameters is derived, in which any possibly existing covariances between the points incorporated in the computation are taken into account.

4. Application of the law of first order error propagation to functions non-linear in the input parameters inevitably leads to approximation errors. A procedure for analytically computing this approximation error is presented. The procedure is based on the definition of Lagrange remainder terms associated with Taylor series truncated after the first order terms.

Chapter 2

Basics of Statistics and Measurement Uncertainty

At the beginning of this chapter, statistical basics are recalled as they are of essential significance for understanding the principles and tools presented in the course of this thesis. Subsequently, a number of fundamental terms of the measurement engineering discipline, namely the true value of a measurement, measurement accuracy, precision and trueness, is described.

Furthermore, the term measurement uncertainty is derived and two basic principles for analyzing measurement uncertainty - a statistical and an analytical approach - are presented. The statistical approach can be evaluated based on natural (i.e. real measurement) data or on synthetical (i.e. randomly generated) data. The generation of multivariate random numbers following a specific probability distribution can, especially when handling high-dimensional data, lead to numerical problems. Thus, three different approaches for generating multivariate random data are presented and compared. Finally, the analytical approach for analyzing measurement uncertainty, namely first order estimation of error propagation, is outlined based on the case of explicit functions.

2.1 Definitions of Basic Statistical Terms

2.1.1 Random Variables

In the mathematical discipline of stochastics, a real random variable is defined as a scalar-valued function relating results of a random experiment to real numbers. The outcomes of a random experiment are termed realizations of the random variable. In the following, random variables are denoted by uppercase symbols (e.g. X), whereas the corresponding lowercase letter (e.g. x) is employed to represent a realization of the random variable.

A random variable is mainly characterized by means of the underlying probability density function. In fact, a probability density function specifies probabilities for the occurrence of a realization of the random variable. A probability density function is characterized by algebraic as well as central moments (see e.g. [40]).

Algebraic moments are defined as expectation values $\mathrm{E}(X^n)$, with n denoting the order of the moment. The most important parameter of a probability density function is the first algebraic moment, which is called the expectation value $\mathrm{E}(X)$ at the same time. It is defined as the arithmetic mean of all theoretically possible realizations of the random variable X.

Moreover, central moments are defined as expectation values $\mathrm{E}\left((X - \mathrm{E}(X))^n\right)$, where n again defines the order of the moment. Obviously, the first central moment is of no relevance, because it is zero by definition. The second central moment:

$$\mathrm{V}(X) = \mathrm{E}\left((X - \mathrm{E}(X))^2\right), \tag{2.1}$$

is termed the variance and is a measure of the width of the probability density function. Hence, it specifies the statistical variation of a random variable around the expectation value. As derived in Appendix A.1, it can also be computed as:

$$\mathrm{V}(X) = \mathrm{E}\left(X^2\right) - \mathrm{E}(X)^2. \tag{2.2}$$

2.1.1.1 Estimation of Expectation Value and Variance

As already mentioned, the definition of the expectation value (as well as the definition of the variance) require knowledge of all theoretically possible realizations (the basic population) of a random experiment. In practice, only a finite number of n_R realizations of an experiment is available. In other words, the available data represents a finite subset of the basic population. This subset is termed a sample with n_R specifying the sample size.

Hence, the expectation value of the random variable can only be estimated. The strong law of large numbers (see e.g. [49]) gives a justification for estimating parameters of a random experiment from a sample population. The law is formulated as:

$$\mathrm{P}\left(\lim_{n_R \to \infty} \frac{1}{n_R} \sum_{i=1}^{n_R} x_i = \mathrm{E}(X)\right) = 1, \tag{2.3}$$

and states that if n_R independent samples of a random experiment are available, the arithmetic mean of the samples converges with increasing n_R towards the expectation value $\mathrm{E}(X)$ at a probability of 1. According to this law, the expectation value of the random experiment may be estimated by the arithmetic mean μ_x of the samples, i.e. the sample mean,

$$\mu_x = \frac{1}{n_R} \sum_{i=1}^{n_R} x_i. \tag{2.4}$$

Furthermore, an unbiased estimate for the variance of a random experiment is computed

by the sample variance σ_x^2 as:

$$\sigma_x^2 = \frac{1}{n_R - 1} \sum_{i=1}^{n_R} (x_i - \mu_x)^2 . \tag{2.5}$$

The sample variance is normalized by the factor $\frac{1}{n_R - 1}$ instead of $\frac{1}{n_R}$ to take into account that one degree of freedom for the estimation is required for μ_x. Thus, Equation (2.1) defines the best unbiased estimate for the variance of the random variable. Notice that:

$$\sigma_x^2 = \frac{1}{n_R - 1} \left(\sum_{i=1}^{n_R} x_i^2 - \frac{1}{n_R} \left(\sum_{i=1}^{n_R} x_i \right)^2 \right) , \tag{2.6}$$

provides a more efficient method for computing the sample variance (see Appendix A.3 for the derivation of the formula), as it avoids the effort of prior computing the sample mean. The non-negative square root of the sample variance denotes the sample standard deviation σ_x.

2.1.1.2 Covariance and Sample Covariance

A measure of the linear interrelation of two random variables X and Y is defined by the covariance,

$$\mathrm{Cov}(X, Y) = \mathrm{E}\left((X - \mathrm{E}(X)) (Y - \mathrm{E}(Y)) \right) . \tag{2.7}$$

As derived in Appendix A.1, the covariance can also be computed as:

$$\mathrm{Cov}(X, Y) = \mathrm{E}\left(XY \right) - \mathrm{E}(X)\mathrm{E}(Y). \tag{2.8}$$

In the practical case where there are n_R discrete values for x_i and y_i, the sample covariance may be computed to estimate the covariance of the two random variables:

$$\sigma_{xy} = \frac{1}{n_R - 1} \left(\sum_{i=1}^{n_R} (x_i - \mu_x) (y_i - \mu_y) \right) , \tag{2.9}$$

which again (see Appendix A.3) may be alternatively computed as:

$$\sigma_{xy} = \frac{1}{n_R - 1} \left(\sum_{i=1}^{n_R} (x_i y_i) - \frac{1}{n_R} \sum_{i=1}^{n_R} x_i \sum_{i=1}^{n_R} y_i \right) . \tag{2.10}$$

2.1.2 Random Vectors

A random vector is a vector of scalar-valued random variables associated with the same random experiment. The outcomes of the random experiment are called again realizations of the random experiment, [25].

In the following, random vectors are denoted by uppercase bold symbols (e.g. $\boldsymbol{X}$), whereas the corresponding lowercase bold letters (e.g. $\boldsymbol{x}$) are employed to term realizations of the random vector. The dimensionality of the random vector is specified by n, and the individual random variables X_i, $i = 1 \dots n$ are collected in a column vector.

The expectation vector $\mathrm{E}(\boldsymbol{X})$ of a random vector is obtained by computing and collecting the individual expectation values of the random variables X_i, $i = 1 \dots n$:

$$\mathrm{E}(\boldsymbol{X}) = \begin{bmatrix} \mathrm{E}(X_1) & \mathrm{E}(X_2) & \dots & \mathrm{E}(X_n) \end{bmatrix}^T. \tag{2.11}$$

Recalling the definition of the variance of a scalar-valued random variable in Equation (2.1), we can obtain the analogon for a random vector as:

$$\mathrm{V}(\boldsymbol{X}) = \mathrm{E}\left((\boldsymbol{X} - \mathrm{E}(\boldsymbol{X}))\,(\boldsymbol{X} - \mathrm{E}(\boldsymbol{X}))^T \right), \tag{2.12}$$

which can be alternatively computed (cf. Appendix A.2) as:

$$\mathrm{V}(\boldsymbol{X}) = \mathrm{E}\left(\boldsymbol{X}\boldsymbol{X}^T\right) - \mathrm{E}(\boldsymbol{X})\mathrm{E}(\boldsymbol{X})^T. \tag{2.13}$$

As the random vector $\boldsymbol{X}$ as well as its expectation vector $\mathrm{E}(\boldsymbol{X})$ are n-dimensional column vectors, $\mathrm{V}(\boldsymbol{X})$ is an $n \times n$ matrix, which is structured as follows:

$$\mathrm{V}(\boldsymbol{X}) = \begin{bmatrix} \mathrm{V}(X_1) & \mathrm{Cov}(X_1, X_2) & \dots & \mathrm{Cov}(X_1, X_n) \\ \mathrm{Cov}(X_2, X_1) & \mathrm{V}(X_2) & \dots & \mathrm{Cov}(X_2, X_n) \\ \vdots & \vdots & \ddots & \vdots \\ \mathrm{Cov}(X_n, X_1) & \mathrm{Cov}(X_n, X_2) & \dots & \mathrm{V}(X_n) \end{bmatrix}. \tag{2.14}$$

The variances of the individual random variables X_i, $i = 1 \dots n$ are located along the main diagonal, whereas the off-diagonal elements contain the covariances specifying the interdependencies of the random variables. As a result, the matrix is called the covariance matrix (sometimes also variance-covariance matrix) of the random vector. Reflecting that $\mathrm{Cov}(X_1, X_2) = \mathrm{Cov}(X_2, X_1)$, it is clear, that covariance matrices are symmetric by nature.

2.1.2.1 Estimation of Expectation Vector and Covariance Matrix

In practice, when a finite number of realizations of the random vector is available, the expectation vector as well as the covariance matrix of the random experiment can only be estimated by the sample mean vector respectively the sample covariance matrix.

Given a population of n_R sample vectors $\boldsymbol{x}_i$, $i = 1 \dots n_R$ of a random experiment, then the sample mean vector $\boldsymbol{\mu}_{\boldsymbol{x}}$ is computed as:

$$\boldsymbol{\mu}_{\boldsymbol{x}} = \frac{1}{n_R} \sum_{i=1}^{n_R} \boldsymbol{x}_i. \tag{2.15}$$

The sample covariance matrix $\Lambda_{\boldsymbol{x}}$ is given as:

$$\Lambda_{\boldsymbol{x}} = \frac{1}{n_R - 1} \sum_{i=1}^{n_R} \left(\left(\boldsymbol{x}_i - \boldsymbol{\mu}_{\boldsymbol{x}} \right) \left(\boldsymbol{x}_i - \boldsymbol{\mu}_{\boldsymbol{x}} \right)^T \right), \tag{2.16}$$

which can be reformulated (see Appendix A.4) as:

$$\Lambda_{\boldsymbol{x}} = \frac{1}{n_R - 1} \left(\sum_{i=1}^{n_R} \left(\boldsymbol{x}_i {\boldsymbol{x}_i}^T \right) - \frac{1}{n_R} \sum_{i=1}^{n_R} \boldsymbol{x}_i \sum_{i=1}^{n_R} {\boldsymbol{x}_i}^T \right) \tag{2.17}$$

$$= \frac{1}{n_R - 1} \left(\sum_{i=1}^{n_R} \left(\boldsymbol{x}_i {\boldsymbol{x}_i}^T \right) - n_R \boldsymbol{\mu}_{\boldsymbol{x}} {\boldsymbol{\mu}_{\boldsymbol{x}}}^T \right). \tag{2.18}$$

The sample covariance matrix holds the sample variances along the main diagonal and the sample covariances in the off-diagonal elements:

$$\Lambda_{\boldsymbol{x}} = \begin{bmatrix} \sigma_{x_1}^2 & \sigma_{x_1 x_2} & \dots & \sigma_{x_1 x_n} \\ \sigma_{x_1 x_2} & \sigma_{x_2}^2 & \dots & \sigma_{x_2 x_n} \\ \vdots & \vdots & \ddots & \vdots \\ \sigma_{x_1 x_n} & \sigma_{x_2 x_n} & \dots & \sigma_{x_n}^2 \end{bmatrix}. \tag{2.19}$$

2.1.3 Gaussian Distributions

The great importance of Gaussian distributions is essentially a result of the fundamental *Central Limit Theorem*. Basically, it states that the sum of mutually independent (and, under some conditions, arbitrarily distributed) random variables, all of them exhibiting the same order of magnitude, can be well approximated by the normal density function. The approximation becomes better with increasing number of incorporated random variables.

2.1.3.1 The Univariate Gaussian Distribution

The probability density function of a univariate Gaussian distribution is defined as:

$$\mathcal{N}(x, \mu, \sigma) = \frac{1}{\sqrt{2\pi}\sigma} \mathrm{e}^{-\frac{(x-\mu)^2}{2\sigma^2}}. \tag{2.20}$$

Here, μ denotes the expectation value and σ refers to the standard deviation of the distribution. Further, x terms a realization of a random variable X that the Gaussian

distribution $\mathcal{N}(x, \mu, \sigma)$ is associated with. The probability density function exhibits a bell-shaped characteristic and is symmetric around the maximum located at the expectation value μ. The inflection points of the distribution are located at $\mu \pm \sigma$.

Following Sachs [49], the transition of X and its realizations x to another random variable Z and its realizations z according to $Z = \frac{X-\mu}{\sigma}$ results in the definition of the probability density of the standard normal distribution. It is characterized by an expectation value $\mu = 0$ and a standard deviation $\sigma = 1$:

$$\mathcal{N}(z, 0, 1) = \frac{1}{\sqrt{2\pi}} \mathrm{e}^{-\frac{z^2}{2}}. \tag{2.21}$$

2.1.3.2 Computation of Expectation Values

Recalling the analytical definition of the expectation value of a function $f(x)$ following a continuous probability density function $\mathcal{P}(x, \mu, \sigma)$,

$$\mathrm{E}(f(x)) = \int_{x=-\infty}^{\infty} f(x)\ \mathcal{P}(x, \mu, \sigma)\, \mathrm{d}x, \tag{2.22}$$

we can compute the first algebraic moment of a sample x following a univariate Gaussian distribution [26] as:

$$\mathrm{E}(x) = \int_{x=-\infty}^{\infty} x \frac{1}{\sqrt{2\pi}\sigma} \mathrm{e}^{-\frac{(x-\mu)^2}{2\sigma^2}}\, \mathrm{d}x = \mu. \tag{2.23}$$

Thus, the first algebraic moment is equal to the expectation value μ of the probability density function. Furthermore, the second central moment is given by:

$$\mathrm{E}\left((x - \mathrm{E}(x))^2\right) = \int_{x=-\infty}^{\infty} (x-\mu)^2 \frac{1}{\sqrt{2\pi}\sigma} \mathrm{e}^{-\frac{(x-\mu)^2}{2\sigma^2}}\, \mathrm{d}x = \sigma^2. \tag{2.24}$$

Thus, the second central moment of the univariate Gaussian distribution is equal to the variance σ^2 of the probability density function. In Appendix B, complete derivations of the two results above are provided.

2.1.3.3 The Multivariate Gaussian Distribution

Extending the univariate case specified in Equation (2.20), the probability density function of a multivariate Gaussian distribution [32] is given as:

$$\mathcal{N}(\boldsymbol{x}, \boldsymbol{\mu}, \Lambda) = \left((2\pi)^p |\Lambda|\right)^{-\frac{1}{2}} \mathrm{e}^{-\frac{1}{2}\left((\boldsymbol{x}-\boldsymbol{\mu})^T \Lambda^{-1} (\boldsymbol{x}-\boldsymbol{\mu})\right)}. \tag{2.25}$$

with the expectation vector $\boldsymbol{\mu}$ and the covariance matrix Λ. Furthermore, $|\Lambda|$ denotes the determinant of the covariance matrix and p refers to the dimensionality of the distribution. Note, that p is equal to the dimensionality of $\boldsymbol{\mu}$ as well as the size of Λ.

Analogous to the univariate formulation, the probability density of the multivariate standard normal distribution underlying a random vector $\boldsymbol{Z}$ with realizations $\boldsymbol{z}$ is defined as:

$$\mathcal{N}(\boldsymbol{z}, \boldsymbol{o}, \mathrm{I}_p) = (2\pi)^{-\frac{p}{2}} \, \mathrm{e}^{-\frac{1}{2}\boldsymbol{z}^T\boldsymbol{z}}, \tag{2.26}$$

with $\boldsymbol{o}$ being the zero expectation vector, and I_p denoting the $p \times p$ identity matrix.

2.2 Basics of Measurement Accuracy and Uncertainty

As outlined by Figliola [20], the term measurement accuracy refers to the ability of a measurement system to indicate the true value of the measurand exactly. By definition, measurement accuracy can only be determined when the true value is known. Hence, specifying the term measurement accuracy inevitably leads to the definition of the true value of a measurement.

2.2.1 The True Value of a Measurement

According to Schmidt [51], the *true value* $\tilde{x}$ of a measurement is defined as the actual value of the measurand taking into account the conditions prevalent at the time of its determination. Actually, the true value is an ideal value. It cannot (except for some calibration standards, which are known to be exact) be determined exactly, because there is no method to measure it without deviations. To overcome the discrepancy with the statement above, the idea of a quasi-true value (also called virtually true value) is introduced. A virtually true value is an approximation of the true value, which can be determined by measurement. It is common practice to use virtually true values for calibrating measurement systems. There, the quantity utilized for the calibration is determined with adequately high effort to approximate the true value of the calibration quantity as good as possible.

2.2.2 Measurement Accuracy, Precision and Trueness

As Schmidt [51] further outlines, the DIN 55350 standard states that measurement accuracy comprises two criteria: precision and trueness. The term precision specifies the ability of a measurement system to indicate a particular value (not necessarily the true value) upon repeated but independent measurement of a specific quantity. Hence, the *precision error* ε_i specifies the random deviation of a single sample x_i with respect to the sample mean:

$$\varepsilon_i = x_i - \mu_x. \tag{2.27}$$

By contrast, trueness refers to the accordance of the average sample value indicated by the measurement system with the true value of the measurand. Any deviation of the average value indicated by the measurement system from the true value must be considered to be systematic and is termed *bias error*. In other words, the difference of the sample mean μ_x

of a (repeatedly but independently measured) population of samples and the true value $\tilde{x}$ of the measured quantity defines the bias error δ_x:

$$\delta_x = \mu_x - \tilde{x}. \tag{2.28}$$

2.2.2.1 Illustration of Bias and Precision Errors

The concept of precision and bias errors is illustrated by means of an image processing example. A series of images of an approximately vertically oriented, unmoved straight object edge was acquired with an industrial camera. Then, each pixel row of the particular series images was evaluated independently to determine the location of a point on the object edge.

As a result, a population of measurement points was obtained for each single pixel row. Figure 2.1 illustrates a sample of the image series with the ideal location of the edge emphasized. Furthermore, a population of measurement points along a particular pixel row is shown in detail. Note that as a consequence of the evaluation procedure, the location of the data points is subject to measurement noise along the horizontal direction only.

As the statistical distribution underlying the measurement noise was assumed to be Gaussian, a normal distribution function with the sample mean μ_x and the sample standard deviation σ_x was computed. The bias error δ_x of the samples is illustrated as the difference of the sample mean and the true value, which is indicated as the exact location on the ideal object edge. Furthermore, the precision error ε_i of a single measurement sample is shown in Figure 2.1. Finally, as a measure of the random variation of the measured samples, the standard deviation σ_x of the population is emphasized.

2.3 Analysis of Measurement Uncertainty

In general, the true value of a measurand is unknown during a measurement. Thus, the magnitude of the total error in the measurement (i.e. the sum of bias and precision errors) cannot be determined exactly, it can only be estimated. As stated for example by Schmidt [51], an estimate of the error associated with a particular measurement is referred to as *measurement uncertainty*.

The discipline *uncertainty analysis* solely addresses statistical deviations. Systematic influences on a measurement should be avoided in principle. If this cannot be achieved, it is common practice to eliminate systematic measurement deviations by means of appropriate corrections, as is outlined e.g. by Figliola [20].

In the following, two different methods for estimating the precision error associated with a measurement are recalled - a statistical and an analytical approach [9]. To handle the general case, the approaches are outlined on the basis of multivariate data.

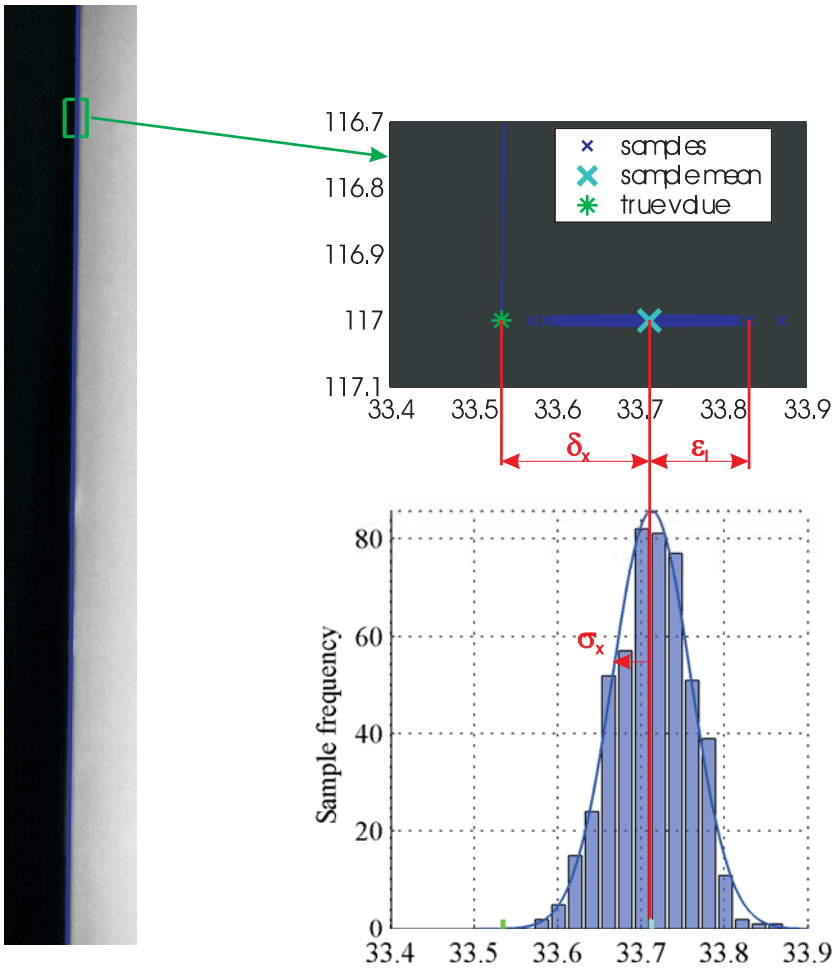

Figure 2.1: Illustration of the concept of precision and bias errors by means of an image processing example.

2.3.1 The Statistical Approach

The statistical approach for estimating the random error associated with a measurement is to make use of the law of large numbers: Given a population of n_R samples $\boldsymbol{y}_i$, the covariance matrix $\Lambda_{\boldsymbol{y}}$ can be estimated (cf. Equation (2.18)) according to:

$$\Lambda_{\boldsymbol{y}} = \frac{1}{n_R - 1} \left(\sum_{i=1}^{n_R} \left(\boldsymbol{y}_i \boldsymbol{y}_i{}^T \right) - n_R \boldsymbol{\mu}_{\boldsymbol{y}} \boldsymbol{\mu}_{\boldsymbol{y}}{}^T \right), \tag{2.29}$$

with $\boldsymbol{\mu}_{\boldsymbol{y}}$ denoting the sample mean vector. The samples $\boldsymbol{y}_i$ required for the estimation may be obtained either:

- naturally (i.e. by means of real measurements), or
- synthetically (i.e. by means of a simulation).

Estimating $\Lambda_{\boldsymbol{y}}$ using real measurement samples is really straightforward: The required samples $\boldsymbol{y}_i$ are obtained by means of repeated but independent measurements, and $\Lambda_{\boldsymbol{y}}$ is

computed according to Equation (2.18). In the following, this approach will be termed *repeated measurements method*.

The procedure of estimating the covariance matrix $\Lambda_{\boldsymbol{y}}$ by means of synthetical samples is referred to as *Monte-Carlo experiment*. Here, a population of random samples $\boldsymbol{y}_i$ is generated with the help of a random number generator, which is outlined in the following section. Then, the sample covariance matrix is computed according to Equation (2.18) again.

2.3.2 Computation of Multivariate Random Data

Since:

1. truly random numbers do not exist, and
2. analysis of well suited natural sources of random processes (e.g. a radioactive source of radiation) is a laborious task,

stochastic simulations have to rely on so-called *pseudo-random number generators*. This term refers to a class of deterministic algorithms generating periodic sequences of numbers, which approximate the properties of random variables [39, 38].

2.3.2.1 Univariate Gaussian Random Numbers

A univariate Gaussian random number y is typically computed as:

$$y = \mu + \sigma z. \tag{2.30}$$

Here, z is an outcome of a pseudo-random number generator for the standard normal distribution. The parameters μ and σ refer to the expectation value respectively the standard deviation of the Gaussian distribution which the sample y is intended to follow.

In other words, Equation (2.30) describes the transformation of a realization z of the standard normal distribution $\Phi(z, 0, 1)$ to y, a sample of the normal distribution $\Phi(y, \mu, \sigma)$.

2.3.2.2 Multivariate Gaussian Random Data

Analogous to Equation (2.30), a multivariate Gaussian random vector $\boldsymbol{y}$ is computed as:

$$\boldsymbol{y} = \boldsymbol{\mu} + \Omega\ \boldsymbol{z}. \tag{2.31}$$

The computation represents a transformation of an outcome $\boldsymbol{z}$ of a multivariate standard normal distribution $\Phi(\boldsymbol{z}, \mathbf{0}, \mathrm{I})$ to $\boldsymbol{y}$, a realization of the multivariate normal distribution $\Phi(\boldsymbol{y}, \boldsymbol{\mu}, \Lambda)$. Note that similarly to the univariate formulation requiring the non-negative square root σ of the variance σ^2, the multivariate computation incorporates a matrix Ω representing the matrix square root of the covariance matrix Λ.

2.3.2.3 Computing the Square Root of a Matrix

As is outlined by Golub and Van Loan [24], the matrix square root of a symmetric, positive-semidefinite[1] matrix Λ is defined as the unique positive-semidefinite matrix Ω, for which holds:

$$\Lambda = \Omega^2. \tag{2.32}$$

The matrix square root Ω is computed as the matrix product:

$$\Omega = \mathsf{USU}^T, \tag{2.33}$$

with U and S resulting from the singular value decomposition of a specific matrix G, which corresponds to the Cholesky triangle of the covariance matrix Λ. Thus:

$$\mathsf{G} = \mathsf{USV}^T. \tag{2.34}$$

2.3.2.4 Cholesky Decomposition

If Λ is a symmetric positive-definite matrix [48], then there is a unique lower triangular matrix G with positive diagonal entries, such that:

$$\Lambda = \mathsf{GG}^T. \tag{2.35}$$

This type of matrix factorization is called Cholesky decomposition [24]. Furthermore, G is termed the Cholesky triangle or, due to its structure, lower triangular square root matrix of Λ.

It is common practice to use G instead of Ω in Equation (2.31), as the unique positive-semidefinite property of Ω is of no relevance for the computation of multivariate random data.

[1] This is a natural property for a non-singular covariance matrix, although an infringement of the positive-semidefinite property can be caused by numerical effects, especially with matrices of large dimensions.

2.3.2.5 LDL^T Factorization

Another approach for factorizing a non-singular, symmetric matrix $\mathsf{\Lambda}$ is given by the LDL^T factorization, which represents a special case of the LU-decomposition [24]. Therein, $\mathsf{\Lambda}$ is decomposed into the matrix product:

$$\mathsf{\Lambda} = \mathsf{LDL}^T, \tag{2.36}$$

with the lower triangular matrix L, which exclusively holds ones along the main diagonal, as well as the diagonal matrix D. Compared to algorithms for calculating the Cholesky decomposition, this approach avoids the computation of square roots. Thus, the factorization is alternatively termed *square root free Cholesky decomposition*. The Cholesky triangle G can be obtained as:

$$\mathsf{G} = \mathsf{L}\mathsf{D}^{\frac{1}{2}}. \tag{2.37}$$

As D is diagonal with positive elements, $\mathsf{D}^{\frac{1}{2}}$ can be efficiently computed.

2.3.2.6 Choice of Algorithm

Concerning the computational costs, it is obvious that computing the unique matrix square root:

$$\mathsf{\Lambda} = \mathsf{G}\mathsf{G}^T = \left(\mathsf{U}\mathsf{S}\mathsf{V}^T\right)\left(\mathsf{U}\mathsf{S}\mathsf{V}^T\right)^T = \mathsf{U}\mathsf{S}^2\mathsf{U}^T = \left(\mathsf{U}\mathsf{S}\mathsf{U}^T\right)\left(\mathsf{U}\mathsf{S}\mathsf{U}^T\right) = \Omega^2, \tag{2.38}$$

is considerably more expensive than the other approaches. Both, the Cholesky decomposition as well as the LDL^T factorization, require an order of magnitude of $\frac{n^3}{3}$ floating point operations (flops), where n terms the size of the decomposed matrix [24]. To obtain the desired Cholesky triangle, the LDL^T factorization is followed by an additional computation step, which represents a triangular matrix multiplication (the effort for calculating $\mathsf{D}^{\frac{1}{2}}$ is neglected) requiring another $\frac{n^3}{3}$ flops. Thus, the Cholesky decomposition is computationally the most efficient of the three algorithms.

As a consequence, synthetical multivariate samples required for Monte-Carlo experiments are computed based on the Cholesky decomposition approach in the following.

2.3.3 The Analytical Approach

Given an explicit, C^1-continuous function,

$$\boldsymbol{y} = \boldsymbol{f}(\boldsymbol{x}), \tag{2.39}$$

whose vector of input data $\boldsymbol{x}$ is represented as a random vector with mean $\boldsymbol{\mu_x}$ and covariance matrix $\mathsf{\Lambda}_{\boldsymbol{x}}$. In order to estimate the covariance matrix associated with the vector of output variables, $\mathsf{\Lambda}_{\boldsymbol{y}}$, a Taylor series of the function $\boldsymbol{f}$ is expanded around $\boldsymbol{\mu_x}$ (see e.g. Clarke[8], Csurka et al.[13], Haralick[27] or Zhao et al.[57]) yielding:

$$\boldsymbol{y} = \boldsymbol{f}(\boldsymbol{x}) = \boldsymbol{f}(\boldsymbol{\mu_x}) + \mathsf{J}_{\boldsymbol{f}}\left(\boldsymbol{\mu_x}\right)\left(\boldsymbol{x} - \boldsymbol{\mu_x}\right) + \mathcal{O}\left(\| \boldsymbol{x} - \boldsymbol{\mu_x} \|^2\right), \tag{2.40}$$

with $\mathsf{J}_{\boldsymbol{f}}(\boldsymbol{\mu}_{\boldsymbol{x}})$ denoting the Jacobian matrix of $\boldsymbol{f}$ with respect to the input data $\boldsymbol{x}$, evaluated at $\boldsymbol{\mu}_{\boldsymbol{x}}$. Given the definition of a covariance matrix:

$$\Lambda_{\boldsymbol{y}} = \mathrm{E}\left(\left(\boldsymbol{y}-\boldsymbol{\mu}_{\boldsymbol{y}}\right)\left(\boldsymbol{y}-\boldsymbol{\mu}_{\boldsymbol{y}}\right)^{T}\right) \tag{2.41}$$

and substituting the approximation $\boldsymbol{\mu}_{\boldsymbol{y}} \approx \boldsymbol{f}(\boldsymbol{\mu}_{\boldsymbol{x}})$ (which only is exact for functions linear in $\boldsymbol{x}$) gives:

$$\Lambda_{\boldsymbol{y}} \approx \mathrm{E}\left(\left(\boldsymbol{f}(\boldsymbol{x})-\boldsymbol{f}(\boldsymbol{\mu}_{\boldsymbol{x}})\right)\left(\boldsymbol{f}(\boldsymbol{x})-\boldsymbol{f}(\boldsymbol{\mu}_{\boldsymbol{x}})\right)^{T}\right). \tag{2.42}$$

In order to obtain a first order estimation of the error propagation, the Taylor series given in Equation (2.40) is truncated after the first order term, which in turn is substituted in Equation (2.42):

$$\begin{aligned}
\Lambda_{\boldsymbol{y}} &\approx \mathrm{E}\left(\left(\mathsf{J}_{\boldsymbol{f}}(\boldsymbol{\mu}_{\boldsymbol{x}})\left(\boldsymbol{x}-\boldsymbol{\mu}_{\boldsymbol{x}}\right)\right)\left(\mathsf{J}_{\boldsymbol{f}}(\boldsymbol{\mu}_{\boldsymbol{x}})\left(\boldsymbol{x}-\boldsymbol{\mu}_{\boldsymbol{x}}\right)\right)^{T}\right) \\
&\approx \mathrm{E}\left(\mathsf{J}_{\boldsymbol{f}}(\boldsymbol{\mu}_{\boldsymbol{x}})\left(\boldsymbol{x}-\boldsymbol{\mu}_{\boldsymbol{x}}\right)\left(\boldsymbol{x}-\boldsymbol{\mu}_{\boldsymbol{x}}\right)^{T}\mathsf{J}_{\boldsymbol{f}}(\boldsymbol{\mu}_{\boldsymbol{x}})^{T}\right) \\
&\approx \mathsf{J}_{\boldsymbol{f}}(\boldsymbol{\mu}_{\boldsymbol{x}})\,\mathrm{E}\left(\left(\boldsymbol{x}-\boldsymbol{\mu}_{\boldsymbol{x}}\right)\left(\boldsymbol{x}-\boldsymbol{\mu}_{\boldsymbol{x}}\right)^{T}\right)\mathsf{J}_{\boldsymbol{f}}(\boldsymbol{\mu}_{\boldsymbol{x}})^{T} \\
&\approx \mathsf{J}_{\boldsymbol{f}}(\boldsymbol{\mu}_{\boldsymbol{x}})\,\Lambda_{\boldsymbol{x}}\mathsf{J}_{\boldsymbol{f}}(\boldsymbol{\mu}_{\boldsymbol{x}})^{T}.
\end{aligned} \tag{2.43}$$

As can be seen, the explicit knowledge of the functional relationship $\boldsymbol{f}$ between $\boldsymbol{x}$ and $\boldsymbol{y}$ is not required as the estimated covariance matrix $\Lambda_{\boldsymbol{y}}$ merely depends on the Jacobian matrix $\mathsf{J}_{\boldsymbol{f}}(\boldsymbol{\mu}_{\boldsymbol{x}})$ as well as the covariance matrix associated with the vector of input data, $\Lambda_{\boldsymbol{x}}$. Note that Equation (2.43) is exact for functions $\boldsymbol{f}$ linear in the input data $\boldsymbol{x}$, but represents an approximation for functions non-linear in $\boldsymbol{x}$.

2.3.3.1 The Jacobian Matrix for Explicit and Implicit Functions

Given a vector of input data $\boldsymbol{x} \in \mathbb{R}^m$ and a vector of output data $\boldsymbol{y} \in \mathbb{R}^n$. Then, the explicit vector-valued function $\boldsymbol{y} = \boldsymbol{f}(\boldsymbol{x})$ maps according to $\boldsymbol{f} : \mathbb{R}^m \mapsto \mathbb{R}^n$, and the $m \times n$ Jacobian matrix $\mathsf{J}_{\boldsymbol{f}}$ can be directly computed by taking the partial derivatives:

$$\mathsf{J}_{\boldsymbol{f}} = \begin{bmatrix} \frac{\partial f_1}{\partial x_1} & \cdots & \frac{\partial f_1}{\partial x_n} \\ \vdots & \ddots & \vdots \\ \frac{\partial f_m}{\partial x_1} & \cdots & \frac{\partial f_m}{\partial x_n} \end{bmatrix}. \tag{2.44}$$

In case of the functional relationship of $\boldsymbol{x}$ and $\boldsymbol{y}$ being given implicitly, i.e.:

$$\boldsymbol{\Phi}\left(\boldsymbol{x}, \boldsymbol{f}(\boldsymbol{x})\right) = \boldsymbol{\Phi}\left(\boldsymbol{x}, \boldsymbol{y}\right) = \boldsymbol{0}, \tag{2.45}$$

the Jacobian matrix $\mathsf{J}_{\boldsymbol{f}}$ exists according to the *Implicit Functions Theorem*[8, 15], if the condition: $\det\left(\frac{\partial \boldsymbol{\Phi}}{\partial \boldsymbol{y}}\right) \neq 0$ is fulfilled. It is then computed as:

$$\mathsf{J}_{\boldsymbol{f}} = -\left(\frac{\partial \boldsymbol{\Phi}}{\partial \boldsymbol{y}}\right)^{-1}\frac{\partial \boldsymbol{\Phi}}{\partial \boldsymbol{x}}. \tag{2.46}$$

2.3.3.2 The Jacobian Matrix for Solving Linear Least Squares Problems

Fitting of geometric models to data points perturbed by measurement noise is a task typically arising in machine vision applications. The fitting operation is commonly formulated as a linear least squares problem:

$$\min_{\boldsymbol{y}} \|\mathsf{D}\boldsymbol{y}\| \quad \text{subject to:} \quad \|\boldsymbol{y}\| = 1, \tag{2.47}$$

with D denoting a design matrix specific for the geometric model being fitted, and $\boldsymbol{y}$ terming the vector of model parameters being sought. The constraint $\|\boldsymbol{y}\| = \boldsymbol{y}^T\boldsymbol{y} = 1$ is to be incorporated for solving the minimization problem using Lagrange multipliers:

$$\boldsymbol{y}^T\mathsf{D}^T\mathsf{D}\boldsymbol{y} - \lambda\left(\boldsymbol{y}^T\boldsymbol{y} - 1\right) = 0. \tag{2.48}$$

Taking the partial derivatives with respect to $\boldsymbol{y}$ and equating them to zero results in:

$$\begin{aligned} 2\mathsf{D}^T\mathsf{D}\boldsymbol{y} - 2\lambda\boldsymbol{y} &= \boldsymbol{0}, \\ \left(\mathsf{A} - \lambda\mathrm{I}\right)\boldsymbol{y} &= \boldsymbol{0}, \end{aligned} \tag{2.49}$$

as well as the constraint: $\boldsymbol{y}^T\boldsymbol{y} - 1 = 0$. As can be seen, the minimization problem leads to an eigenvector problem, $\left(\mathsf{A} - \lambda\mathrm{I}\right)\boldsymbol{y} = \boldsymbol{0}$, with $\mathsf{A} \triangleq \mathsf{D}^T\mathsf{D}$ denoting the scatter matrix, which contains the vector of input parameters $\boldsymbol{x}$. The vector of model parameters $\boldsymbol{y}$ is now found as the eigenvector corresponding to the smallest eigenvalue $\lambda_{\min}$ of A. Equivalently[24], the solution can be found by computing the singular value decomposition of D and taking the right singular vector corresponding to the smallest singular value of the design matrix.

Given a set of n measured data points in the plane, whose coordinates are collected in a vector $\boldsymbol{x} = [x_1, \ldots, x_n, y_1, \ldots, y_n]^T$, together with the covariance matrix $\Lambda_{\boldsymbol{x}}$ representing the perturbation in the data points. In order to estimate the error propagation to $\boldsymbol{y}$, the vector of parameters specifying the geometric model being fitted to the data points, the law of first order error propagation can be applied:

$$\Lambda_{\boldsymbol{y}} = \mathsf{J}_{\boldsymbol{f}}\Lambda_{\boldsymbol{x}}\mathsf{J}_{\boldsymbol{f}}^T. \tag{2.50}$$

According to Clarke [8], the Jacobian matrix for the fitting operation, $\mathsf{J}_{\boldsymbol{f}}$, may be approximated by the Jacobian of the implicit function $\boldsymbol{\Phi}(\boldsymbol{x}, \boldsymbol{y}) = \mathsf{A}\boldsymbol{y} = \boldsymbol{0}$. In other words, it is postulated that $\lambda_{\min}$ is negligibly small: $\lambda_{\min} \approx 0$. This leads to the assumption of A being singular. As a result, the Jacobian $\mathsf{J}_{\boldsymbol{f}}$ is computed according to Equation (2.46) with the required matrix inverse:

$$\left(\frac{\partial\boldsymbol{\Phi}}{\partial\boldsymbol{y}}\right)^{-1} = \mathsf{A}^{-1}. \tag{2.51}$$

As A is assumed to be singular, its inverse must be approximated by the pseudo-inverse, $\mathsf{A}^+ = \mathsf{V}\mathsf{S}^+\mathsf{U}^T$. The required matrices, U, S and V, are obtained by applying singular value decomposition to A, i.e. $\mathsf{A} = \mathsf{U}\mathsf{S}\mathsf{V}^T$. In Appendix C, the general definition of pseudo-inverse matrices is outlined. Moreover, the special situation of computing the pseudo-inverse of a quadratic and symmetric matrix A (such as a scatter matrix) is treated.

Finally, the approximation of the Jacobian $\mathsf{J}_{\boldsymbol{f}}$ is obtained as:

$$\mathsf{J}_{\boldsymbol{f}} \approx -\mathsf{A}^+\frac{\partial\boldsymbol{\Phi}}{\partial\mathsf{A}}\frac{\partial\mathsf{A}}{\partial\boldsymbol{x}}. \tag{2.52}$$

Chapter 3

Representation of Uncertain Geometric Primitives

This chapter introduces points, lines and conics as basic geometric primitives as they are required for solving typical metric vision problems. The primitives are described within the context of projective geometry, more precisely *planar projective geometry*. As there exists plenty of literature concerning projective geometry (see e.g. [15, 22, 52, 41, 32, 53]), only the most important concepts, namely the usage of homogeneous coordinates and the duality principle of the projective plane, are briefly recalled here.

After this, the covariance matrices of points and lines are discussed, as they provide a means to describe the uncertainty associated with these geometric objects. Finally, the equations for visualizing the confidence envelopes of points and lines are derived based on a Mahalanobis distance measure.

3.1 Planar Projective Geometry

As outlined by Faugeras [15], there are at least two fundamental reasons for applying projective geometry in machine vision tasks:

1. the fact that optical mappings of the 3-dimensional real world to an image plane - independently of considering the human eye or the lens of a camera system - can be simply modelled by perspective (i.e. central) projections, and
2. a number of computational advantages compared to Euclidean geometry, such as the possibility of consistently utilizing tools of linear algebra or the unproblematic representation of geometric objects near or at infinity.

Thus, the concepts of projective geometry as well as the representation of geometric objects by means of projective coordinates (also termed *homogeneous coordinates*) are applied throughout the entire work.

In the following, homogeneous coordinates utilized to describe geometric primitives are collected in column vectors. The particular coordinates are termed with indexed, lowercase letters, e.g. x_i, whereas the coordinate vector itself is denoted by the corresponding lowercase bold symbol, e.g. $\boldsymbol{x}$. In contrast, inhomogeneous point coordinates are specified with letters indicating the associated Euclidean coordinate axis. Thus, a point $\boldsymbol{p}$ is represented by the inhomogeneous coordinates x_p and y_p.

3.1.1 Representation of Points

A point $\boldsymbol{p}$ of the projective plane is represented by the column three-vector $[p_1, p_2, p_3]^T$. The transition from homogeneous to inhomogeneous coordinates (as, for example, they are required for visualization purposes) is established by normalizing the homogeneous coordinate vector by the last entry [23]:

$$x_p = \frac{p_1}{p_3},\ y_p = \frac{p_2}{p_3}, \tag{3.1}$$

with x_p and y_p representing the inhomogeneous coordinates of $\boldsymbol{p}$.

The inverse operation, i.e. the transition from inhomogeneous point coordinates (as, for example, they may result from an image processing algorithm operating on an affine image plane) to homogeneous coordinates, is achieved by simply adding a scalar 1 as the third coordinate, thus $\boldsymbol{p} = [x_p, y_p, 1]^T$.

3.1.2 Representation of Lines

A line $\boldsymbol{l}$ of the projective plane is defined by the coordinate vector $[l_1, l_2, l_3]^T$. The coordinates l_1 and l_2 define the orientation of the line. Hence, they are also called *line orientation parameters*. The third parameter, l_3, specifies the moment of the line with respect to the point of origin. Thus, the parameter is also termed the *line moment parameter*.

The homogeneous line equation for a line of the projective plane is given by:

$$\sum_{i=1}^{3} p_i l_i = p_1 l_1 + p_2 l_2 + p_3 l_3 = 0, \tag{3.2}$$

with the homogeneous point coordinates p_i, $i = 1 \ldots 3$. The line equation may also be formulated as a matrix product:

$$\begin{bmatrix} p_1 & p_2 & p_3 \end{bmatrix} \begin{bmatrix} l_1 \\ l_2 \\ l_3 \end{bmatrix} = \boldsymbol{p}^T \boldsymbol{l} = 0. \tag{3.3}$$

3.1.2.1 Normalized Lines

A line is geometrically normalized, if it exhibits a unit length orientational vector, i.e.:

$$\sqrt{l_1^2 + l_2^2} = 1. \tag{3.4}$$

Normalized line vectors are required for all metric computations, such as determination of the orthogonal distance of a point to a line or the normal distance between two parallel lines. Thus, given a line $\boldsymbol{l}$, the homogeneous coordinate vector ${}_n\boldsymbol{l}$ of its geometrically normalized representation is computed according to:

$$ {}_n\boldsymbol{l} = \begin{bmatrix} {}_nl_1 \\ {}_nl_2 \\ {}_nl_3 \end{bmatrix} = \frac{1}{\sqrt{l_1^2 + l_2^2}} \begin{bmatrix} l_1 \\ l_2 \\ l_3 \end{bmatrix}. \tag{3.5} $$

3.1.2.2 Normal Distance of a Point to a Line

The oriented, i.e. signed normal distance d of a point $\boldsymbol{p}$ with normalized homogeneous coordinates $[x_p, y_p, 1]^T$ to a line $\boldsymbol{l}$, represented by the normalized homogeneous coordinate vector $[l_1, l_2, l_3]^T$, is obtained as:

$$ d = x_p l_1 + y_p l_2 + l_3 = \boldsymbol{p}^T \boldsymbol{l}. \tag{3.6} $$

This result may be demonstrated by applying the Grassmannian determinant principle, as outlined by Klein [36]. Given two points $\boldsymbol{x}_1$ and $\boldsymbol{x}_2$ with homogeneous coordinate vectors $[x_1, y_1, 1]^T$ and $[x_2, y_2, 1]^T$ defining a segment of a straight line, than any point $\boldsymbol{x}$ on the same line with coordinate vector $[x, y, 1]^T$ is a linear combination of $\boldsymbol{x}_1$ and $\boldsymbol{x}_2$, thus:

$$ \begin{vmatrix} x & y & 1 \\ x_1 & y_1 & 1 \\ x_2 & y_2 & 1 \end{vmatrix} = 0. \tag{3.7} $$

Expanding the determinant gives:

$$ \begin{aligned} x\,(y_1 - y_2) - y\,(x_1 - x_2) + (x_1 y_2 - x_2 y_1) &= 0 \\ x l_1 + y l_2 + l_3 &= 0, \end{aligned} \tag{3.8} $$

which is another formulation of the homogeneous line equation (cf. Equations (3.2), (3.3)). The line coordinates are thus:

$$ \begin{aligned} l_1 &= y_1 - y_2, \\ l_2 &= x_2 - x_1, \\ l_3 &= x_1 y_2 - x_2 y_1. \end{aligned} \tag{3.9} $$

Similarly, the Grassmannian principle can be applied to define a determinant of two points $\boldsymbol{x}_1$ and $\boldsymbol{x}_2$ specifying a line segment and a third point $\boldsymbol{p} = [x_p, y_p, 1]^T$ being non-collinear to $\boldsymbol{x}_1$ and $\boldsymbol{x}_2$:

$$ 2A_{\triangle} = \begin{vmatrix} x_p & y_p & 1 \\ x_1 & y_1 & 1 \\ x_2 & y_2 & 1 \end{vmatrix}, \tag{3.10} $$

which defines twice the signed area $A_\triangle$ of the triangle spanned by $\boldsymbol{x}_1$, $\boldsymbol{x}_2$ and $\boldsymbol{p}$. Obviously, the same area is obtained as the product of the length of the line segment and d, the normal distance of $\boldsymbol{p}$ to the line segment:

$$\begin{aligned} d\sqrt{(x_1 - x_2)^2 + (y_1 - y_2)^2} &= x_p (y_1 - y_2) - y_p (x_1 - x_2) + (x_1 y_2 - x_2 y_1) \\ d\sqrt{l_1^2 + l_2^2} &= x_p l_1 + y_p l_2 + l_3 \\ d &= \frac{1}{\sqrt{l_1^2 + l_2^2}} \boldsymbol{p}^T \boldsymbol{l}, \end{aligned} \tag{3.11}$$

which equals the formulation given in Equation (3.6) with normalized line coordinates.

3.1.3 Interrelations of Special Line Pairs

3.1.3.1 Parameters of Orthogonal Lines

Two lines ${}_1\boldsymbol{l}$ and ${}_2\boldsymbol{l}$ with normalized line coordinates $[{}_1l_1,\ {}_1l_2,\ {}_1l_3]^T$ and $[{}_2l_1,\ {}_2l_2,\ {}_2l_3]^T$ respectively, are orthogonal to one another, if their orientational parameters fulfill the conditions:

$$\begin{aligned} {}_2l_1 &= \pm {}_1l_2, \\ {}_2l_2 &= \mp {}_1l_1. \end{aligned} \tag{3.12}$$

3.1.3.2 Parameters of Parallel Lines

Two lines ${}_1\boldsymbol{l}$ and ${}_2\boldsymbol{l}$ with normalized line coordinates $[{}_1l_1,\ {}_1l_2,\ {}_1l_3]^T$ and $[{}_2l_1,\ {}_2l_2,\ {}_2l_3]^T$ respectively, are parallel if their orientational parameters are identical. Thus:

$$\begin{aligned} {}_2l_1 &= {}_1l_1, \\ {}_2l_2 &= {}_1l_2. \end{aligned} \tag{3.13}$$

The normal distance d between the two parallel lines (each with normalized line coordinates) is:

$$d = |{}_1l_3 - {}_2l_3| . \tag{3.14}$$

3.1.3.3 Center Line of two Given Parallel Lines

Given two parallel lines ${}_1\boldsymbol{l}$ and ${}_2\boldsymbol{l}$ with normalized coordinate vectors $[l_1, l_2,\ {}_1l_3]^T$ respectively $[l_1, l_2,\ {}_2l_3]^T$, a third line ${}_c\boldsymbol{l}$, representing the center line of ${}_1\boldsymbol{l}$ and ${}_2\boldsymbol{l}$, is sought. The homogeneous line vector ${}_c\boldsymbol{l}$ is obtained as:

$$\begin{bmatrix} {}_cl_1 \\ {}_cl_2 \\ {}_cl_3 \end{bmatrix} = \begin{bmatrix} l_1 \\ l_2 \\ \frac{1}{2}({}_1l_3 + {}_2l_3) \end{bmatrix}. \tag{3.15}$$

3.1.4 The Duality Principle of the Projective Plane

Considering Equation (3.3), the condition for a point $\boldsymbol{x}$ belonging to a line $\boldsymbol{l}$ is obviously symmetric for the homogeneous vectors of the point as well as that of the line [15]. Thus:

$$\boldsymbol{x}^T\boldsymbol{l} = \boldsymbol{l}^T\boldsymbol{x} = 0. \tag{3.16}$$

The interchangeability of points and lines in the projective plane is commonly known as the duality principle. A line in the homogeneous point space (spanned by x_i, $i = 1 \dots 3$) exhibits a dual point in the homogeneous line space (spanned by l_i, $i = 1 \dots 3$) and vice versa.

Due to the duality principle, the following dual statements are valid for the projective plane [41]:

1. two distinct points of the projective plane determine a unique interpolating line, and
2. two distinct lines of the projective plane determine a unique intersection point.

Note, that the second statement provides an advantage of the projective geometry with respect to Euclidean geometry, where this statement is invalid for parallel lines [23].

3.1.4.1 The Point of Intersection of two Lines

Given two lines ${}_1\boldsymbol{l}$ and ${}_2\boldsymbol{l}$, their intersection point $\boldsymbol{p}$ is obtained as the cross product of the vectors holding the homogeneous line coordinates:

$$\boldsymbol{p} = {}_1\boldsymbol{l} \times {}_2\boldsymbol{l}. \tag{3.17}$$

Thus, the homogeneous coordinates of the point of intersection are:

$$\begin{bmatrix} p_1 \\ p_2 \\ p_3 \end{bmatrix} = \begin{bmatrix} {}_1l_2\ {}_2l_3 & - & {}_1l_3\ {}_2l_2 \\ {}_1l_3\ {}_2l_1 & - & {}_1l_1\ {}_2l_3 \\ {}_1l_1\ {}_2l_2 & - & {}_1l_2\ {}_2l_1 \end{bmatrix}. \tag{3.18}$$

3.1.4.2 The Interpolating Line of two Points

The line $\boldsymbol{l}$ interpolating two given points $\boldsymbol{p}_1$ and $\boldsymbol{p}_2$ with homogeneous coordinate vectors $[{}_1p_1,\ {}_1p_2,\ {}_1p_3]^T$ respectively $[{}_2p_1,\ {}_2p_2,\ {}_2p_3]^T$, is computed as the cross product of the vectors holding the point coordinates:

$$\boldsymbol{l} = {}_1\boldsymbol{p} \times {}_2\boldsymbol{p}. \tag{3.19}$$

As a result, the homogeneous coordinates of the interpolating line are (cf. Equation (3.7)):

$$\begin{bmatrix} l_1 \\ l_2 \\ l_3 \end{bmatrix} = \begin{bmatrix} {}_1p_2\ {}_2p_3 & - & {}_1p_3\ {}_2p_2 \\ {}_1p_3\ {}_2p_1 & - & {}_1p_1\ {}_2p_3 \\ {}_1p_1\ {}_2p_2 & - & {}_1p_2\ {}_2p_1 \end{bmatrix}. \tag{3.20}$$

As can be seen, the line going through two given points and the point of intersection of two given lines are identically computed. This is another consequence of the duality principle of the projective plane.

The interchangeability of points and lines in the previous computations is emphasized in Figure 3.1. The line interpolating two given points in the normalized point space is represented by its dual in the normalized line parameter space, which is the point of intersection of the two lines representing the duals of the given points.

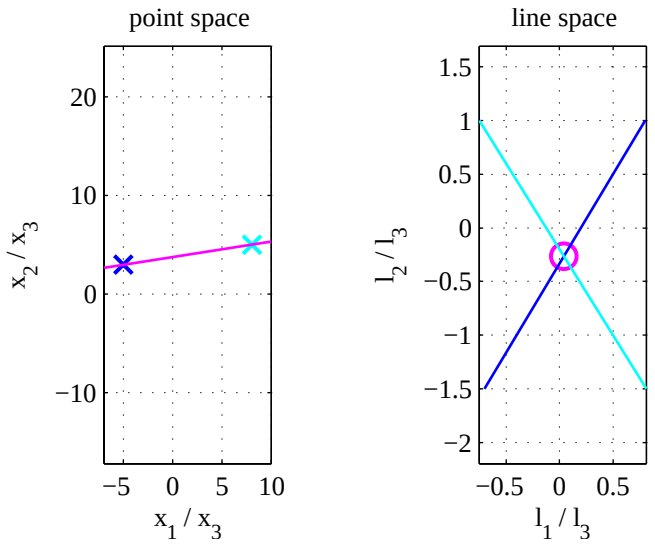

Figure 3.1: Illustration of the duality principle in the projective plane. Points and lines represent dual geometric objects in the homogeneous point and line space, respectively.

3.1.5 Representation of Conics

As, among many other authors, outlined by Hartley and Zisserman [32], the implicit equation of a general conic in homogeneous form is defined as:

$$\sum_{i,j=1}^{3} c_{ij}x_i x_j = c_{11}x_1^2 + 2c_{12}x_1x_2 + 2c_{13}x_1x_3 + c_{22}x_2^2 + 2c_{23}x_2x_3 + c_{33}x_3^2 = 0, \tag{3.21}$$

i.e. a homogeneous quadratic polynomial in the point coordinates x_1, x_2 and x_3.
The coefficients c_{ij} are commonly denoted as *conic coefficients*. Note, that $c_{ij} = c_{ji}$ for $i, j = 1 \ldots 3$. Equation (3.21) may be rewritten as the matrix expression:

$$\boldsymbol{x}^T \mathsf{C} \boldsymbol{x} = 0, \tag{3.22}$$

where the conic coefficient matrix C (commonly called the *conic matrix* in short) terms a symmetric matrix holding the conic coefficients,

$$\mathsf{C} = \begin{bmatrix} c_{11} & c_{12} & c_{13} \\ c_{12} & c_{22} & c_{23} \\ c_{13} & c_{23} & c_{33} \end{bmatrix}. \tag{3.23}$$

Analog to the homogeneous coordinate vectors of points and lines, the homogeneous conic matrix is defined only up to a non-zero scaling factor. Thus, the conic matrix C exhibits five degrees of freedom, which can be reproduced as six entries of the symmetric matrix C less one utilized for the scaling.

3.1.5.1 Euclidean Classification of Conics

The commonly known Euclidean classification of conics utilizes three parameters invariant to Euclidean transformations (see e.g. [23, 47, 35]):

$$I_1 = \det \mathsf{C}, \tag{3.24}$$
$$I_2 = c_{11}c_{22} - c_{12}^2, \tag{3.25}$$
$$I_3 = c_{11} + c_{22}. \tag{3.26}$$

If the conic matrix C is singular, i.e. $I_1 = 0$, the specified conic is degenerate. This results the conic to appear either as a pair of intersecting lines (when C is rank deficient by 1) or as a pair of collinear lines or a single point (for C being rank deficient by 2). For a nonsingular conic matrix C, the conic is said to be proper. There are three types of proper conics to be differentiated, which is achieved by investigation of the invariant I_2:

$$\mathsf{C} \text{ defines } \begin{cases} \text{a hyperbola} & \dots \text{ if } I_2 < 0, \\ \text{a parabola} & \dots \text{ if } I_2 = 0, \\ \text{an ellipse} & \dots \text{ if } I_2 > 0. \end{cases}$$

The elliptic conic has to be further divided into two subcases. If $I_1 I_3 > 0$, the conic exhibits an empty set of points, whereas $I_1 I_3 < 0$ indicates a real ellipse.

3.1.5.2 The Center Point of a Conic

The implicit equation of a general conic with normalized homogeneous point coordinates $[x_p, y_p, 1]^T$ is given as:

$$c_{11}x_p^2 + 2c_{12}x_p y_p + 2c_{13}x_p + c_{22}y_p^2 + 2c_{23}y_p + c_{33} = 0. \tag{3.27}$$

The center point of a conic may be determined by computing the translational parameters x_0 and y_0 required to center the conic at the point of origin. The transformation matrix for executing the translational operation is given as:

$$\mathsf{T} = \begin{bmatrix} 1 & 0 & -x_0 \\ 0 & 1 & -y_0 \\ 0 & 0 & 1 \end{bmatrix}. \tag{3.28}$$

As a result, the conic coefficient matrix C_T of the translated conic becomes:

$$\begin{aligned}\mathsf{C}_T &= \mathsf{T}^{-T}\mathsf{C}\mathsf{T}^{-1} \\ &= \begin{bmatrix} c_{11} & c_{12} & c_{11}x_0 + c_{12}y_0 + c_{13} \\ & c_{22} & c_{12}x_0 + c_{22}y_0 + c_{23} \\ \text{sym.} & & c_{11}x_0^2 + 2c_{12}x_0y_0 + 2c_{13}x_0 + c_{22}y_0^2 + 2c_{23}y_0 + c_{33} \end{bmatrix}. \end{aligned} \tag{3.29}$$

A consequence of the conic being centered at the point of origin is that the two conic coefficients, appearing linear with x_p and y_p in the equation of the translated conic, have to become zero. Thus, we take the first two entries of the last column of C_T and set them to zero:

$$\begin{aligned} c_{11}x_0 + c_{12}y_0 + c_{13} &= 0, \\ c_{12}x_0 + c_{22}y_0 + c_{23} &= 0. \end{aligned} \tag{3.30}$$

Solving for the translational parameters x_0 and y_0 delivers the coordinates of the conic center point:

$$\begin{aligned} x_0 &= \frac{c_{12}c_{23} - c_{22}c_{13}}{c_{11}c_{22} - c_{12}^2}, \\ y_0 &= \frac{c_{12}c_{13} - c_{11}c_{23}}{c_{11}c_{22} - c_{12}^2}. \end{aligned} \tag{3.31}$$

Note, that the denominator in the definition of x_p and y_p is identic and equals the Euclidean invariant I_2 defined in Equation (3.25). Obviously, the conic center point lies at infinity, if this denominator becomes zero. This corresponds to the point of intersection of the conic asymptotes lying at infinity. Thus, the conic represents a parabola [46], which conforms with the results of the Euclidean classification. Back-substituting the coordinates of the conic center point gives:

$$\mathsf{C}_T = \begin{bmatrix} c_{11} & c_{12} & 0 \\ c_{12} & c_{22} & 0 \\ 0 & 0 & \gamma \end{bmatrix}, \tag{3.32}$$

with

$$\gamma = \frac{2c_{12}c_{13}c_{23} + c_{11}c_{22}c_{33} - c_{11}c_{23}^2 - c_{22}c_{13}^2 - c_{33}c_{12}^2}{c_{11}c_{22} - c_{12}^2}. \tag{3.33}$$

Notice that Equation (3.32) represents the coefficient matrix of a general conic centered at the point of origin.

3.1.5.3 The Circle as a Special Case of the General Conic

The general conic is homogeneously defined by six coefficients $\{c_{11}, c_{12}, c_{13}, c_{22}, c_{23}, c_{33}\}$, as is seen in the implicit definition given in Equation (3.21). The special case of circles exhibits two restrictions on the general conic formulation, as is outlined by Zsombor-Murray [58] for example. On the one hand, the aspect ratio of a circle is equal to 1, which

is brought in as the condition $c_{11} = c_{22}$, and on the other hand, a circle is not transformed under rotation, which results in $c_{12} = 0$. Thus, the conic coefficient matrix C_c for a circle is obtained as:

$$\mathsf{C}_c = \begin{bmatrix} C_1 & 0 & C_2 \\ & C_1 & C_3 \\ \text{sym.} & & C_4 \end{bmatrix}. \tag{3.34}$$

Notice that the circle coefficients are denoted with uppercase letters to avoid confusion with the coefficients of a general conic. The parameter set $\{C_1, C_2, C_3, C_4\}$ is known as the set of tetra-circular Grassmannian coordinates [36]. With this, the implicit equation of the circle results to:

$$\boldsymbol{x}^T \mathsf{C}_c \boldsymbol{x} = C_1(x_1^2 + x_2^2) + 2C_2 x_1 x_3 + 2C_3 x_2 x_3 + C_4 x_3^2 = 0, \tag{3.35}$$

which is rewritten utilizing normalized homogeneous point coordinates $[x_p, y_p, 1]^T$ to obtain the more familiar formulation:

$$C_1(x_p^2 + y_p^2) + 2C_2 x_p + 2C_3 y_p + C_4 = 0. \tag{3.36}$$

The affine circle parameters, namely the circle center coordinates x_0 respectively y_0 and the circle radius r, can then be computed from the set of tetra-circular Grassmannian coordinates as:

$$\begin{aligned} x_0 &= -\frac{C_2}{C_1}, \\ y_0 &= -\frac{C_3}{C_1}, \\ r &= \sqrt{x_0^2 + y_0^2 - \frac{C_4}{C_1}} = \sqrt{\frac{C_2^2 + C_3^2}{C_1^2} - \frac{C_4}{C_1}}. \end{aligned} \tag{3.37}$$

Note that Equation (3.35) describes a proper circle only if the conditions $C_1 \neq 0$, as well as $\frac{C_2^2+C_3^2}{C_1^2} - \frac{C_4}{C_1} > 0$ are fulfilled. Otherwise, the conic is degenerate. Concretely:

- $C_1 = 0$: The conic represents a pair of lines, whereas one of them specifies the line at infinity, $x_3 = 0$.
- $\frac{C_2^2+C_3^2}{C_1^2} - \frac{C_4}{C_1} = 0$: Equation (3.35) describes a pair of complex conjugate lines. The only real point of the conic is the point of intersection of the two lines.
- $\frac{C_2^2+C_3^2}{C_1^2} - \frac{C_4}{C_1} < 0$: The conic exhibits an empty set of points, i.e. it has no real point.

3.2 Uncertainty associated with Geometric Primitives

3.2.1 The Covariance Matrix of a Point

The covariance matrix Λ_p of a point $\boldsymbol{p}$ with homogeneous coordinate vector $[p_1, p_2, p_3]^T$ is given as the 3×3 matrix [21]:

$$\Lambda_p = \begin{bmatrix} \sigma_{p_1}^2 & \sigma_{p_1 p_2} & \sigma_{p_1 p_3} \\ \sigma_{p_1 p_2} & \sigma_{p_2}^2 & \sigma_{p_2 p_3} \\ \sigma_{p_1 p_3} & \sigma_{p_2 p_3} & \sigma_{p_3}^2 \end{bmatrix}. \tag{3.38}$$

The variances of the homogeneous coordinates $\sigma_{p_1}^2$, $\sigma_{p_2}^2$ and $\sigma_{p_3}^2$ are arranged along the main diagonal, whereas the off-diagonal entries $\sigma_{p_1 p_2}$, $\sigma_{p_1 p_3}$ and $\sigma_{p_2 p_3}$ specify the covariances between the coordinates. Due to the fact that $\boldsymbol{p}$ is a homogeneous coordinate vector, the covariance matrix specified by Λ_p is also homogeneous, i.e. it is defined only up to a non-zero scaling factor.

3.2.1.1 From Homogeneous to Inhomogeneous Point Coordinates

The computation of inhomogeneous point coordinates x_p and y_p according to Equation (3.1) results in a 2×2 covariance matrix $\Lambda_{\boldsymbol{p}^i}$ representing the uncertainty of the inhomogeneous point coordinates:

$$\Lambda_{\boldsymbol{p}^i} = \begin{bmatrix} \sigma_{x_p}^2 & \sigma_{x_p y_p} \\ \sigma_{x_p y_p} & \sigma_{y_p}^2 \end{bmatrix}. \tag{3.39}$$

There, $\sigma_{x_p}^2$ and $\sigma_{y_p}^2$ denote the variances of x_p respectively y_p, and $\sigma_{x_p y_p}$ terms the covariance between the inhomogeneous point coordinates. A first order estimation for $\Lambda_{\boldsymbol{p}^i}$ may analytically be computed according to the first order error propagation principle introduced in Section 2.3.3:

$$\Lambda_{\boldsymbol{p}^i} = \mathsf{J}_N \Lambda_{\boldsymbol{p}} \mathsf{J}_N^T, \tag{3.40}$$

where $\Lambda_{\boldsymbol{p}}$ represents the covariance matrix of the homogeneous point coordinates and J_N terms the Jacobian matrix of the normalizing operation [8]:

$$\mathsf{J}_N = \frac{1}{p_3^2} \begin{bmatrix} p_3 & 0 & -p_1 \\ 0 & p_3 & -p_2 \end{bmatrix}. \tag{3.41}$$

Notice that this operation is non-linear, thus the first-order estimation $\Lambda_{\boldsymbol{p}^i}$ merely represents an approximation for the covariance matrix of the inhomogeneous point vector.

3.2.1.2 From Inhomogeneous to Homogeneous Point Coordinates

The inverse operation of homogenizing an inhomogeneous point vector by adding a scalar 1 to the inhomogeneous coordinates x_p and y_p results in the 3×3 covariance matrix:

$$\Lambda_p = \begin{bmatrix} \sigma_{x_p}^2 & \sigma_{x_p y_p} & 0 \\ \sigma_{x_p y_p} & \sigma_{y_p}^2 & 0 \\ 0 & 0 & 0 \end{bmatrix}, \tag{3.42}$$

as the additional value is obviously not subject to statistical noise. The result may analytically be simply verified by applying the error propagation principle utilized above.

3.2.2 The Covariance Matrix of a Line

The covariance matrix Λ_l of a line $\boldsymbol{l}$ with homogeneous coordinate vector $[l_1, l_2, l_3]^T$ is given by the 3×3 matrix:

$$\Lambda_l = \begin{bmatrix} \sigma_{l_1}^2 & \sigma_{l_1 l_2} & \sigma_{l_1 l_3} \\ \sigma_{l_1 l_2} & \sigma_{l_2}^2 & \sigma_{l_2 l_3} \\ \sigma_{l_1 l_3} & \sigma_{l_2 l_3} & \sigma_{l_3}^2 \end{bmatrix}. \tag{3.43}$$

The diagonal components $\sigma_{l_1}^2$, $\sigma_{l_2}^2$ and $\sigma_{l_3}^2$ denote the variances of the three line parameters, and $\sigma_{l_1 l_2}$, $\sigma_{l_1 l_3}$ and $\sigma_{l_2 l_3}$ specify the covariances between the line parameters. As with points, the covariance matrix of a line is homogeneous too, i.e. it is defined only up to a non-zero scaling factor.

3.2.2.1 Geometric Normalization of a Line

The first order estimation for the covariance matrix $\Lambda_{\boldsymbol{l}_N}$ of a line $\boldsymbol{l}_N$, specifying the geometrically normalized representation of $\boldsymbol{l}$ (see Equation (3.5)), is obtained as:

$$\Lambda_{\boldsymbol{l}_N} = \mathsf{J}_N \Lambda_{\boldsymbol{l}} \mathsf{J}_N^T, \tag{3.44}$$

with $\Lambda_{\boldsymbol{l}}$ denoting the homogeneous covariance matrix of the line $\boldsymbol{l}$, and J_N specifying the Jacobian matrix of the normalizing operation:

$$\mathsf{J}_N = \frac{1}{(l_1^2 + l_2^2)^{\frac{3}{2}}} \begin{bmatrix} l_2^2 & -l_1 l_2 & 0 \\ -l_1 l_2 & l_1^2 & 0 \\ -l_1 l_3 & -l_2 l_3 & l_1^2 + l_2^2 \end{bmatrix}. \tag{3.45}$$

Notice that the first-order estimation $\Lambda_{\boldsymbol{l}_N}$ solely represents an approximation for the covariance matrix of the normalized line $\boldsymbol{l}_N$ as the normalizing operation obviously is non-linear.

3.3 Visualization of Uncertain Geometric Primitives

Given a Gaussian random vector with expectation vector $\boldsymbol{\mu}$ and covariance matrix Λ. Then the expression:

$$(\boldsymbol{x} - \boldsymbol{\mu})^T \Lambda^+ (\boldsymbol{x} - \boldsymbol{\mu}) = k^2, \tag{3.46}$$

defines the locus of points $\boldsymbol{x}$ exhibiting equal probability in the given Gaussian distribution. Therein, Λ^+ terms the pseudo-inverse of the given covariance matrix and k^2 denotes the squared *Mahalanobis distance*, a parameter following a χ^2 distribution with r degrees of freedom, r being the rank of Λ. Table 3.1 lists a number of values $k^2_{\alpha,r}$ for some typically utilized probabilities α as well as for $r = \{2, 3\}$, i.e. the planar and the spatial situation, respectively. A more comprehensive list can be found in [49].

r	$k^2_{0.70,r}$	$k^2_{0.80,r}$	$k^2_{0.90,r}$	$k^2_{0.95,r}$	$k^2_{0.99,r}$	$k^2_{0.999,r}$
2	2.41	3.22	4.61	5.99	9.21	13.82
3	3.66	4.64	6.25	7.81	11.34	16.27

Table 3.1: Mahalanobis distance values typically utilized for visualizations in the 2- as well as the 3-dimensional space.

Ochoa [42] as well as Hartley [32] described a procedure for computing algebraic expressions representing the confidence envelopes of points and lines of the affine plane. The great advantage of this approach is that the conic matrices describing the uncertainty envelopes of points and lines (and in the general case, i.e. the n-dimensional space, points and hyperplanes) can be directly derived from the expectation vector $\boldsymbol{\mu}$ and the covariance matrix Λ associated with the geometric primitive.

3.3.1 Points and Lines of the Affine Plane

Given the expectation vector $\boldsymbol{\mu}$ as well as the covariance matrix Λ associated with an uncertain point of the plane, which is represented by the homogeneous 3-vector $\boldsymbol{x}$. The covariance matrix Λ has rank 2, as the homogeneous point vector obviously exhibits only two degrees of freedom. Starting with the definition of the squared Mahalanobis distance in Equation (3.46), a change of coordinates is applied to the covariance matrix Λ at first:

$$\Lambda' = \mathsf{U}\Lambda\mathsf{U}^T = \begin{bmatrix} \bar{\Lambda} & \mathbf{0} \\ \mathbf{0}^T & 0 \end{bmatrix}, \tag{3.47}$$

with the diagonal matrix $\bar{\Lambda}$. The required matrix U represents a similarity transformation, which is computed as: $\mathsf{U} = s\mathsf{V}^T$. Therein, V denotes an orthogonal matrix determined from the eigen-decomposition of Λ, i.e.: $\Lambda = \mathsf{V}\mathsf{D}\mathsf{V}^T$, with the diagonal matrix $\mathsf{D} = \mathrm{diag}\{\lambda_1, \lambda_2, 0\}$ holding the eigenvalues of Λ. Note that D is related with Λ' according to: $\Lambda' = s^2\mathsf{D}$. The real parameter $s \neq 0$ is chosen such as to obtain a 1 as the last element of the

transformed (homogeneous) expectation vector, $\boldsymbol{\mu}' = \mathsf{U}\boldsymbol{\mu} = s\mathsf{V}^T\boldsymbol{\mu}$. With the specified similarity transformation, we obtain:

$$(\boldsymbol{x} - \boldsymbol{\mu})^T \Lambda^+ (\boldsymbol{x} - \boldsymbol{\mu}) = k^2, \tag{3.48}$$

$$(\boldsymbol{x}' - \boldsymbol{\mu}')^T \Lambda'^+ (\boldsymbol{x}' - \boldsymbol{\mu}') = k^2, \tag{3.49}$$

$$(\bar{\boldsymbol{x}} - \bar{\boldsymbol{\mu}})^T \bar{\Lambda}^{-1} (\bar{\boldsymbol{x}} - \bar{\boldsymbol{\mu}}) = k^2, \tag{3.50}$$

with $\boldsymbol{x}' = \begin{bmatrix} \bar{\boldsymbol{x}} & 1 \end{bmatrix}^T$ and $\boldsymbol{\mu}' = \begin{bmatrix} \bar{\boldsymbol{\mu}} & 1 \end{bmatrix}^T$. Expanding Equation (3.50) gives:

$$\bar{\boldsymbol{x}}^T\bar{\Lambda}^{-1}\bar{\boldsymbol{x}} - \bar{\boldsymbol{x}}^T\bar{\Lambda}^{-1}\bar{\boldsymbol{\mu}} - \bar{\boldsymbol{\mu}}^T\bar{\Lambda}^{-1}\bar{\boldsymbol{x}} + \bar{\boldsymbol{\mu}}^T\bar{\Lambda}^{-1}\bar{\boldsymbol{\mu}} - k^2 = 0, \tag{3.51}$$

which can be reformulated with matrix notation as:

$$\begin{bmatrix} \bar{\boldsymbol{x}}^T & 1 \end{bmatrix} \begin{bmatrix} \bar{\Lambda}^{-1} & -\bar{\Lambda}^{-1}\bar{\boldsymbol{\mu}} \\ -\bar{\boldsymbol{\mu}}^T\bar{\Lambda}^{-1} & \bar{\boldsymbol{\mu}}^T\bar{\Lambda}^{-1}\bar{\boldsymbol{\mu}} - k^2 \end{bmatrix} \begin{bmatrix} \bar{\boldsymbol{x}} \\ 1 \end{bmatrix} = 0. \tag{3.52}$$

This is - as can be verified by means of a computer algebra system, such as Maple® - equivalent to:

$$\begin{bmatrix} \bar{\boldsymbol{x}}^T & 1 \end{bmatrix} \begin{bmatrix} \bar{\boldsymbol{\mu}}\bar{\boldsymbol{\mu}}^T & -k^2\bar{\Lambda}\bar{\boldsymbol{\mu}} \\ \bar{\boldsymbol{\mu}}^T & 1 \end{bmatrix}^{-1} \begin{bmatrix} \bar{\boldsymbol{x}} \\ 1 \end{bmatrix} = 0, \tag{3.53}$$

$$\boldsymbol{x}'^T \left[\boldsymbol{\mu}'\boldsymbol{\mu}'^T - k^2\Lambda'\right]^{-1} \boldsymbol{x}' = 0, \tag{3.54}$$

which represents - as we consider planar entities in homogeneous coordinates - the equation of a conic with coefficient matrix:

$$\mathsf{C}' = \left[\boldsymbol{\mu}'\boldsymbol{\mu}'^T - k^2\Lambda'\right]^{-1}. \tag{3.55}$$

The conic can now be transformed back (cf. Equation (3.47)) to the original coordinate system according to: $\mathsf{C} = \mathsf{U}^T\mathsf{C}'\mathsf{U}$, resulting in a conic with coefficient matrix:

$$\mathsf{C} = \left[\boldsymbol{\mu}\boldsymbol{\mu}^T - k^2\Lambda\right]^{-1}. \tag{3.56}$$

3.3.1.1 The Confidence Envelope of a Point on the Affine Plane

Considering a point $\boldsymbol{p}$ on the affine plane, whose homogeneous coordinate vector follows a Gaussian distribution with expectation vector $\boldsymbol{\mu}_{\boldsymbol{p}}$ and covariance matrix $\Lambda_{\boldsymbol{p}}$. The locus of points with equal probability in the given distribution satisfy:

$$\left(\boldsymbol{p} - \boldsymbol{\mu}_{\boldsymbol{p}}\right)^T \Lambda_{\boldsymbol{p}}^+ \left(\boldsymbol{p} - \boldsymbol{\mu}_{\boldsymbol{p}}\right) = k_{\alpha,2}^2, \tag{3.57}$$

and form the homogeneous conic:

$$\mathsf{C}_{\boldsymbol{p}} = \left[\boldsymbol{\mu}_{\boldsymbol{p}}\boldsymbol{\mu}_{\boldsymbol{p}}^T - k_{\alpha,2}^2\Lambda_{\boldsymbol{p}}\right]^{-1}. \tag{3.58}$$

The squared Mahalanobis distance parameter $k_{\alpha,2}^2$ is chosen according to the desired probability α (cf. Table 3.1). It can be verified - by analysis of the Euclidean invariants of the conic - that $\mathsf{C}_{\boldsymbol{p}}$ specifies a proper ellipse.

3.3.1.2 The Confidence Envelope of a Line on the Affine Plane

According to the duality principle of the projective plane between points and lines and accordingly of conics and dual conics, the procedure is analogously applied to lines.

Given a line $\boldsymbol{l}$ in the affine plane, whose homogeneous coordinate vector follows a Gaussian distribution with expectation vector $\boldsymbol{\mu_l}$ and covariance matrix $\Lambda_{\boldsymbol{l}}$. The set of lines with equal likelihood in the given distribution fulfill:

$$(\boldsymbol{l} - \boldsymbol{\mu_l})^T \Lambda_{\boldsymbol{l}}^{+} (\boldsymbol{l} - \boldsymbol{\mu_l}) = k_{\alpha,2}^2, \tag{3.59}$$

and form the homogeneous line conic $\mathsf{C}_{\boldsymbol{l}}^{*} = \left[\boldsymbol{\mu_l}\boldsymbol{\mu_l}^T - k_{\alpha,2}^2 \Lambda_{\boldsymbol{l}}\right]^{-1}$. Thus, the dual point conic specifying the confidence envelope associated with $\boldsymbol{l}$ is computed as the matrix adjoint[1]:

$$\mathsf{C}_{\boldsymbol{l}} = \boldsymbol{\mu_l}\boldsymbol{\mu_l}^T - k_{\alpha,2}^2 \Lambda_{\boldsymbol{l}}. \tag{3.60}$$

It can be verified - by analysis of the Euclidean invariants of the conic - that $\mathsf{C}_{\boldsymbol{l}}$ specifies a hyperbola, whose two branches are symmetric about $\boldsymbol{\mu_l}$.

3.3.1.3 The Location of a Line with Respect to a Line Confidence Envelope

In order to determine the location of an arbitrary line with respect to a given line confidence hyperbola, one could explicitly compute the points of intersection and verify for real or imaginary coordinates. Another approach is based on the dual problem, i.e. computing the location of the dual point with respect to the dual confidence ellipse. Thus, a line with coordinate vector $\boldsymbol{l}_k$ lies within a confidence hyperbola defined by $\mathsf{C}_{\boldsymbol{l}}$, if:

$$\operatorname{sgn}\left(\boldsymbol{l}_k{}^T \mathsf{C}_{\boldsymbol{l}}^{-1} \boldsymbol{l}_k\right) = \operatorname{sgn}\left(\boldsymbol{\mu_l}{}^T \mathsf{C}_{\boldsymbol{l}}^{-1} \boldsymbol{\mu_l}\right). \tag{3.61}$$

3.3.2 Points and Hyperplanes in n Dimensions

The results obtained for points and lines on the affine plane can directly be generalized to n dimensions.

An n-dimensional point with homogeneous coordinate vector $\boldsymbol{x} \in \mathbb{R}^{n+1}$ is given as a random vector following a Gaussian distribution with expectation vector $\boldsymbol{\mu_x}$ and covariance matrix $\Lambda_{\boldsymbol{x}}$ of rank n. The confidence envelope of the point $\boldsymbol{x}$ is specified by the homogeneous n-dimensional hyper-ellipsoid (which is commonly termed the *hyper-ellipsoid of uncertainty*):

$$\mathsf{Q}_{\boldsymbol{x}} = \left[\boldsymbol{\mu_x}\boldsymbol{\mu_x}^T - k_{\alpha,n}^2 \Lambda_{\boldsymbol{x}}\right]^{-1}. \tag{3.62}$$

Given a hyperplane with homogeneous coordinate vector $\boldsymbol{\pi} \in \mathbb{R}^{n+1}$ as a random vector following a Gaussian distribution with expectation vector $\boldsymbol{\mu_\pi}$ and covariance matrix $\Lambda_{\boldsymbol{\pi}}$ of rank n. Following the duality principle of the n-dimensional projective space, the confidence envelope of the hyperplane is specified by the n-dimensional hyperboloid:

$$\mathsf{Q}_{\boldsymbol{\pi}} = \boldsymbol{\mu_\pi}\boldsymbol{\mu_\pi}^T - k_{\alpha,n}^2 \Lambda_{\boldsymbol{\pi}}. \tag{3.63}$$

[1] Notice the matrix adjoint property $\mathsf{C}_{\boldsymbol{l}}^{*} \sim \mathsf{C}_{\boldsymbol{l}}^{-1}$ for a non-singular, symmetric matrix $\mathsf{C}_{\boldsymbol{l}}$.

3.3.3 Plotting Confidence Envelopes of Planar Points and Lines

As demonstrated in the previous sections, the confidence envelopes of points and lines on the affine plane are represented by ellipses and hyperbolae, respectively. They can be visualized by means of a general algorithm for plotting implicitly given functions. In this thesis, the conic representing the actual confidence envelope is evaluated on points of a regular grid. Then, the zero contour of the resulting residual surface is extracted and finally, the curve is plotted by joining adjacent points of the contour with linear segments.

3.3.3.1 Illustration Example

An uncertain point on the affine plane is given with a homogeneous coordinate vector following a Gaussian distribution with expectation vector $\boldsymbol{\mu}_{\boldsymbol{p}}$ and covariance matrix $\boldsymbol{\Lambda}_{\boldsymbol{p}}$:

$$\boldsymbol{\mu}_{\boldsymbol{p}} = \begin{bmatrix} 3 \\ 5 \\ 1 \end{bmatrix}, \quad \boldsymbol{\Lambda}_{\boldsymbol{p}} = \begin{bmatrix} 0.25 & 0.05 & 0 \\ 0.05 & 0.25 & 0 \\ 0 & 0 & 0 \end{bmatrix}. \tag{3.64}$$

A number of $n = 10^4$ random sample points was generated. Figure 3.2 (left) shows (a portion of) the random sample points together with confidence ellipses corresponding to confidence levels of 95%, 99% and 99.9% respectively.

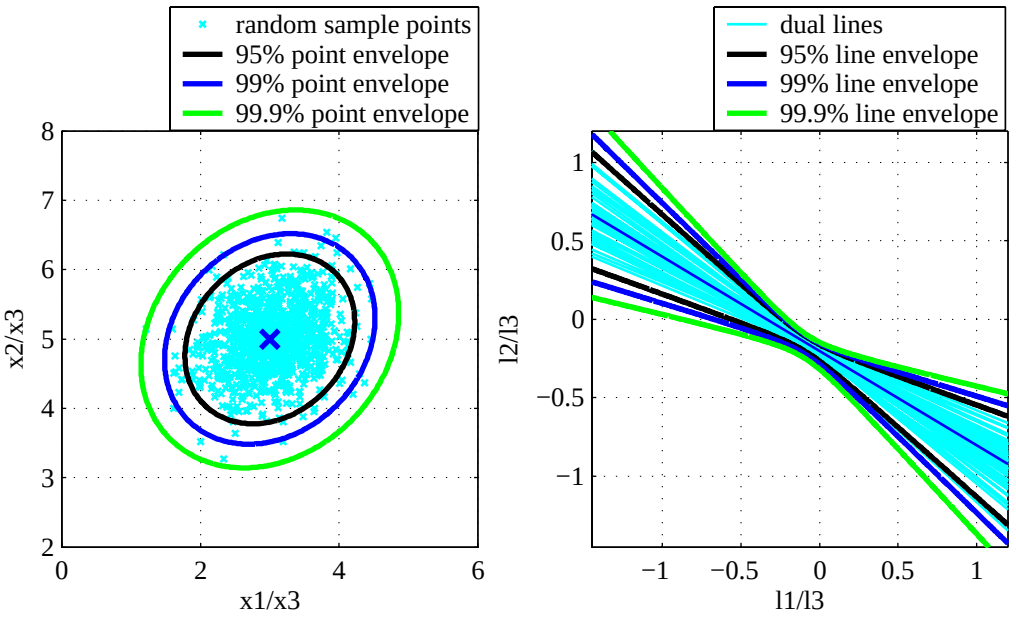

Figure 3.2: A population of random points with associated confidence ellipses (left) and the population of dual lines with associated dual confidence hyperbolae (right).

In the dual space, i.e. the space of normalized line parameters, the sample points represent dual lines and the confidence envelopes are given as the confidence hyperbolae associated with the dual lines. Figure 3.2 (right) visualizes the dual lines together with their associated confidence hyperbolae in the space of normalized line parameters.

Part II

Uncertainty Analysis of Metric Vision Tasks

Chapter 4

Fitting of Linear Geometric Models

This chapter addresses fitting of lines to given sets of uncertain data points together with an uncertainty analysis for the fitting procedure. A numerically robust and efficient fitting algorithm is outlined for fitting a straight line to a set of data points of the projective plane. However, the algorithm is generally applicable for fitting linear geometric models, i.e. planes and hyperplanes, to sets of data points in spaces of higher dimensions.

In order to analytically compute the covariance matrix associated with the line fitted to the data points, the law of first order error propagation is applied to the particular steps of the fitting procedure. Schalk [50] has presented this approach based on synthetically generated sets of data points. Thereby, isotropic homogeneous perturbation of the particular data points was assumed.

The work presented here is more general in that sense, that it makes no assumption on the perturbation model underlying the data points. The situation of anisotropic and inhomogeneous perturbation is handled, which is reflected by fully occupied covariance matrices $\Lambda_{\boldsymbol{p}_i}$ associated with the particular data points $\boldsymbol{p}_i = \begin{bmatrix} x_i & y_i \end{bmatrix}^T$. Thus,

$$\Lambda_{\boldsymbol{p}_i} = \begin{bmatrix} \sigma_{x_i}^2 & \sigma_{x_i y_i} \\ \sigma_{x_i y_i} & \sigma_{y_i}^2 \end{bmatrix}. \tag{4.1}$$

At first, the algorithm for fitting a line to a set of uncertain data points is described, followed by the uncertainty analysis for the particular steps of the procedure. As a consequence of the generalization in the perturbation model, the outcomes of the uncertainty analysis can not be listed explicitly. Thus, the results are illustrated by means of numerical examples. Subsequently, an extension of the fitting algorithm for fitting a pair of parallel lines to two given sets of uncertain data points is presented. Again, the particular steps of the procedure are analyzed by means of first order error propagation.

All of the numerical examples are executed on measurement data extracted from image sequences acquired under conditions of repeatability. The results of the fitting algorithms applied on the measurement data are statistically evaluated and compared with the results of first order error propagation. These comparisons reveal that the best agreement can be achieved if the fully occupied covariance matrices associated with the data points are incorporated in the analyses.

4.1 Fitting a Line to a Set of Uncertain Data Points

4.1.1 The Fitting Algorithm

As outlined in Section 3.1.2, a line in the projective plane is represented by the homogeneous 3-vector $\boldsymbol{l} = [l_1, l_2, l_3]^T$ and the line equation is given by:

$$\boldsymbol{p}^T\boldsymbol{l} = xl_1 + yl_2 + l_3 = 0, \tag{4.2}$$

with $\boldsymbol{p} = [x, y, 1]^T$ denoting the normalized homogeneous 3-vector of a point on the line. Given a set of n data points $\boldsymbol{p}_i = [x_i, y_i, 1]^T$ perturbed by measurement noise, the points will not lie exactly on the line, in general. Thus, there are residual parameters r_i, $i = 1 \dots n$, associated with the particular data points, which leads to a set of n linear equations of the type:

$$x_i l_1 + y_i l_2 + l_3 = r_i. \tag{4.3}$$

In order to compute the line that fits the set of data points best in a least squares sense, we have to solve the following system of linear equations:

$$\mathsf{D}\boldsymbol{l} = \begin{bmatrix} x_1 & y_1 & 1 \\ x_2 & y_2 & 1 \\ \vdots & \vdots & \vdots \\ x_n & y_n & 1 \end{bmatrix} \begin{bmatrix} l_1 \\ l_2 \\ l_3 \end{bmatrix} = \begin{bmatrix} r_1 \\ r_2 \\ \vdots \\ r_n \end{bmatrix}, \tag{4.4}$$

with the design matrix D. This can be rewritten as the linear least squares problem:

$$\min_{\boldsymbol{l}} \|\mathsf{D}\boldsymbol{l}\| \quad \text{subject to:} \quad \sqrt{l_1^2 + l_2^2} = 1. \tag{4.5}$$

This problem can now be solved by eigenvector calculation of the scatter matrix $\mathsf{A} = \mathsf{D}^T\mathsf{D}$ and extraction of the eigenvector corresponding to the smallest eigenvalue of A. Thereby, the constraint $\sqrt{l_1^2 + l_2^2} = 1$ has to be incorporated by means of Lagrange multipliers[24].

An alternative approach is based on singular value decomposition and is outlined as follows: The columns of D have differing statistical nature, as the column of 1's is - in contrast to the two other columns - statistically invariant. For this reason, Harker et al. [31] stated that it is advantageous to partition D into two parts:

$$\mathsf{D} = \left[\begin{array}{c|c} \mathsf{D}_1 & \mathsf{D}_0 \end{array}\right] = \left[\begin{array}{cc|c} x_1 & y_1 & 1 \\ x_2 & y_2 & 1 \\ \vdots & \vdots & \vdots \\ x_n & y_n & 1 \end{array}\right], \tag{4.6}$$

and to apply orthogonal residualisation of D_1 onto D_0 to yield a new design matrix $\hat{\mathsf{D}}$

with statistically congenerous columns. These represent columns of mean-free point coordinates, i.e.:

$$\hat{\mathsf{D}} = \begin{bmatrix} x_1 - \mu_x & y_1 - \mu_y \\ x_2 - \mu_x & y_2 - \mu_y \\ \vdots & \vdots \\ x_n - \mu_x & y_n - \mu_y \end{bmatrix}, \tag{4.7}$$

with the mean values $\mu_x = \frac{1}{n}\sum_{i=1}^{n} x_i$ and $\mu_y = \frac{1}{n}\sum_{i=1}^{n} y_i$. The linear least squares problem to be solved now becomes:

$$\min_{\hat{\boldsymbol{l}}} \|\hat{\mathsf{D}}\hat{\boldsymbol{l}}\| \quad \text{subject to:} \quad \|\hat{\boldsymbol{l}}\| = 1, \tag{4.8}$$

with $\hat{\boldsymbol{l}} = \begin{bmatrix} l_1 & l_2 \end{bmatrix}^T$ denoting the vector of line orientation parameters. This approach has been introduced by Harker et al. [31, 29, 30] and has been further discussed by Tratnig [54], Schalk [50] and Koller [37]. For further details, the reader is referred to the cited literature.

The fitting problem is now solved by computing the singular value decomposition (SVD) of $\hat{\mathsf{D}}$ and extraction of the right singular vector corresponding to the smallest singular value of $\hat{\mathsf{D}}$. The constraint $\|\hat{\boldsymbol{l}}\| = 1$ is implicitly fulfilled by the implementation of the SVD algorithm (see Golub[24]). Compared with the approach based on eigenvector calculation, this method delivers exactly identical results. However, the SVD-based approach is preferred for the reason of numerical robustness as well as the implicit consideration of the normalization constraint.

Finally, the line moment parameter l_3 is obtained by back-substituting the coordinates of the centroid of the data points into Equation (4.2) and results in:

$$l_3 = -(\mu_x l_1 + \mu_y l_2). \tag{4.9}$$

Summarizing, the presented fitting algorithm exhibits the following properties:

- The algorithm implicitly introduces the constraint $\|\hat{\boldsymbol{l}}\| = \sqrt{l_1^2 + l_2^2} = 1$, thus the vector of line coordinates obtained is geometrically normalized (cf. Section 3.1.2).
- The error measure being minimized by this algorithm is given by the sum of the squared residual parameters r_i. As a consequence of the implicitly realized geometric normalization, the residuals are equal to the orthogonal distances d_i of the particular data points to the fitted line. Thus, the approach minimizes the geometric error measure and yields an unbiased maximum-likelihood solution.

4.1.2 First Order Error Propagation for the Fitting Algorithm

In the following, the propagation of the uncertainty associated with the data points towards the covariance matrix of the homogeneous 3-vector of the line fitted to the data points is analyzed by means of the law of first order error propagation. Thereby, the individual steps of the fitting algorithm are considered separately:

1. computation of the centroid of the data points,
2. calculation of mean-free data points and setup of the design matrix $\hat{\mathsf{D}}$ according to Equation (4.7),
3. estimation of the line orientation parameters l_1 and l_2 by singular value decomposition of $\hat{\mathsf{D}}$, and
4. computation of the line moment parameter l_3 according to Equation (4.9).

4.1.2.1 Organisation of the Data Points

Considering a set of n data points, perturbed by measurement noise. The "measurement" of the data points, i.e. extraction of their x- and y-coordinates, under conditions of repeatability can be regarded as repeatedly taking a sample from a random experiment (refer to Section 2.1). In the following, the x- and y-coordinates of the data points, x_i and y_i, $i = 1 \dots n$, are to be understood as expectation values of a Gaussian probability density function underlying the measurement process. They are collected in a common expectation vector $\boldsymbol{p}$ according to the following order: $\boldsymbol{p} = \begin{bmatrix} x_1 & x_2 & \dots & x_n & y_1 & y_2 & \dots & y_n \end{bmatrix}^T$. The Gaussian probability density function underlying the measurement process is characterized by the $2n \times 2n$ covariance matrix $\Lambda_{\boldsymbol{p}}$, which is structured as:

$$\Lambda_{\boldsymbol{p}} = \begin{bmatrix} \Lambda_{\boldsymbol{x}} & \mathsf{C}_{\boldsymbol{xy}} \\ \mathsf{C}_{\boldsymbol{xy}}^T & \Lambda_{\boldsymbol{y}} \end{bmatrix}, \tag{4.10}$$

with the $n \times n$ covariance matrices of the x- and y-coordinates:

$$\Lambda_{\boldsymbol{x}} = \begin{bmatrix} \sigma_{x_1}^2 & \sigma_{x_1x_2} & \dots & \sigma_{x_1x_n} \\ \sigma_{x_1x_2} & \sigma_{x_2}^2 & \dots & \sigma_{x_2x_n} \\ \vdots & \vdots & \ddots & \vdots \\ \sigma_{x_1x_n} & \sigma_{x_2x_n} & \dots & \sigma_{x_n}^2 \end{bmatrix}, \quad \Lambda_{\boldsymbol{y}} = \begin{bmatrix} \sigma_{y_1}^2 & \sigma_{y_1y_2} & \dots & \sigma_{y_1y_n} \\ \sigma_{y_1y_2} & \sigma_{y_2}^2 & \dots & \sigma_{y_2y_n} \\ \vdots & \vdots & \ddots & \vdots \\ \sigma_{y_1y_n} & \sigma_{y_2y_n} & \dots & \sigma_{y_n}^2 \end{bmatrix}, \tag{4.11}$$

and the $n \times n$ matrix of covariances between the x- and y-coordinates:

$$\mathsf{C}_{\boldsymbol{xy}} = \begin{bmatrix} \sigma_{x_1y_1} & \sigma_{x_1y_2} & \dots & \sigma_{x_1y_n} \\ \sigma_{x_2y_1} & \sigma_{x_2y_2} & \dots & \sigma_{x_2y_n} \\ \vdots & \vdots & \ddots & \vdots \\ \sigma_{x_ny_1} & \sigma_{x_ny_2} & \dots & \sigma_{x_ny_n} \end{bmatrix}. \tag{4.12}$$

Note, that this data structure enables the incorporation of all possibly existing correlations between the data points for the subsequent analyses.

4.1.2.2 Computing the Coordinates of the Centroid

In the following, the coordinates of the centroid of the data points are collected in a column vector:

$$\boldsymbol{\mu} = \begin{bmatrix} \mu_x \\ \mu_y \end{bmatrix} = \begin{bmatrix} \frac{1}{n}\sum_{i=1}^{n} x_i \\ \\ \frac{1}{n}\sum_{i=1}^{n} y_i \end{bmatrix}. \tag{4.13}$$

This enables the computation of a fully occupied 2×2 covariance matrix $\Lambda_{\boldsymbol{\mu}}$ associated with $\boldsymbol{\mu}$. Note that the analysis could also be executed on μ_x and μ_y separately of one another, however the covariance between the centroid coordinates would then be ignored. According to the law of first order error propagation, the covariance matrix associated with the vector of centroid coordinates is computed as:

$$\Lambda_{\boldsymbol{\mu}} = \mathsf{J}_{\boldsymbol{\mu}} \Lambda_{\boldsymbol{p}} \mathsf{J}_{\boldsymbol{\mu}}{}^{T}, \tag{4.14}$$

with the $2 \times 2n$ Jacobian matrix:

$$\mathsf{J}_{\boldsymbol{\mu}} = \begin{bmatrix} \mathsf{J}_{\mu_x} & \mathbf{0} \\ \mathbf{0} & \mathsf{J}_{\mu_y} \end{bmatrix}, \quad \mathsf{J}_{\mu_x} = \mathsf{J}_{\mu_y} = \frac{1}{n}\,\mathbf{1}. \tag{4.15}$$

Therein, $\mathbf{0}$ and $\mathbf{1}$ term row vectors of length n, holding 0's and 1's respectively. Note that Equation (4.13) is linear in the input parameters, i.e. the point coordinates, x_i and y_i. Thus, the error propagation specified by Equation (4.14) is exact.

4.1.2.3 Calculation of Mean-Free Data Points

The mean-free coordinates of the data points are calculated as:

$$\begin{aligned} \hat{x}_i &= x_i - \mu_x, \\ \hat{y}_i &= y_i - \mu_y, \end{aligned} \tag{4.16}$$

and are collected in a vector $\hat{\boldsymbol{p}}$ of length $2n$:

$$\hat{\boldsymbol{p}} = \begin{bmatrix} \hat{x}_1 & \hat{x}_2 & \dots & \hat{x}_n & \hat{y}_1 & \hat{y}_2 & \dots & \hat{y}_n \end{bmatrix}^{T}. \tag{4.17}$$

The covariance matrix $\Lambda_{\hat{\boldsymbol{p}}}$ associated with $\hat{\boldsymbol{p}}$ is computed according to the law of first order error propagation as:

$$\Lambda_{\hat{\boldsymbol{p}}} = \mathsf{J}_{\hat{\boldsymbol{p}}} \Lambda_{\boldsymbol{p}} \mathsf{J}_{\hat{\boldsymbol{p}}}{}^{T}, \tag{4.18}$$

with the $2n \times 2n$ Jacobian matrix $\mathsf{J}_{\hat{\boldsymbol{p}}}$ being structured as:

$$\mathsf{J}_{\hat{\boldsymbol{p}}} = \begin{bmatrix} \mathsf{J}_{\hat{x}} & \mathsf{0} \\ \mathsf{0} & \mathsf{J}_{\hat{y}} \end{bmatrix}, \quad \mathsf{J}_{\hat{x}} = \mathsf{J}_{\hat{y}} = \mathrm{I}_n - \frac{1}{n}\,\mathsf{1}. \tag{4.19}$$

Therein, $\mathsf{0}$ and $\mathsf{1}$ are $n \times n$ matrices of 0's and 1's, and I_n terms the $n \times n$ identity matrix. As the computation of mean-free point coordinates represents a linear operation, the error propagation specified by Equation (4.18) is exact.

4.1.2.4 Computation of the Line Orientation Parameters

Computation of the 2-vector of line orientation parameters $\hat{\boldsymbol{l}}$ is formulated as the following linear least squares problem:

$$\min_{\hat{\boldsymbol{l}}} \|\hat{\mathsf{D}}\hat{\boldsymbol{l}}\| \quad \text{subject to:} \quad \|\hat{\boldsymbol{l}}\| = 1. \tag{4.20}$$

Therein, the design matrix $\hat{\mathsf{D}}$ holds the mean-free point coordinates as specified in Equation (4.7). Applying the law of first order error propagation, the covariance matrix associated with $\hat{\boldsymbol{l}}$ is estimated as:

$$\Lambda_{\hat{\boldsymbol{l}}} \approx \mathsf{J}_{\hat{\boldsymbol{l}}} \Lambda_{\hat{\boldsymbol{p}}} \mathsf{J}_{\hat{\boldsymbol{l}}}^{T}, \tag{4.21}$$

where $\mathsf{J}_{\hat{\boldsymbol{l}}}$ denotes the Jacobian matrix of the implicit function $\boldsymbol{\Phi}\left(\hat{\boldsymbol{p}}, \hat{\boldsymbol{l}}\right) = \mathsf{A}\hat{\boldsymbol{l}} = \mathbf{0}$. Referring to Section 2.3.3.2, $\mathsf{J}_{\hat{\boldsymbol{l}}}$ is approximated by:

$$\mathsf{J}_{\hat{\boldsymbol{l}}} \approx -\mathsf{A}^{+} \frac{\partial \boldsymbol{\Phi}}{\partial \mathsf{A}} \frac{\partial \mathsf{A}}{\partial \hat{\boldsymbol{p}}}. \tag{4.22}$$

Therein, A terms the scatter matrix, which is given as:

$$\mathsf{A} = \hat{\mathsf{D}}^{T}\hat{\mathsf{D}} = \begin{bmatrix} \sum_{i=1}^{n} \hat{x}_i^2 & \sum_{i=1}^{n} \hat{x}_i\hat{y}_i \\ \sum_{i=1}^{n} \hat{x}_i\hat{y}_i & \sum_{i=1}^{n} \hat{y}_i^2 \end{bmatrix}. \tag{4.23}$$

Furthermore, the required matrices $\frac{\partial \boldsymbol{\Phi}}{\partial \mathsf{A}}$ and $\frac{\partial \mathsf{A}}{\partial \hat{\boldsymbol{p}}}$ are computed as:

$$\frac{\partial \Phi}{\partial \mathsf{A}} = \begin{bmatrix} l_1 & l_2 & 0 & 0 \\ 0 & 0 & l_1 & l_2 \end{bmatrix}, \text{ and} \tag{4.24}$$

$$\frac{\partial \mathsf{A}}{\partial \hat{\boldsymbol{p}}} = \begin{bmatrix} 2\hat{x}_1 & 2\hat{x}_2 & \dots & 2\hat{x}_n & 0 & 0 & \dots & 0 \\ \hat{y}_1 & \hat{y}_2 & \dots & \hat{y}_n & \hat{x}_1 & \hat{x}_2 & \dots & \hat{x}_n \\ \hat{y}_1 & \hat{y}_2 & \dots & \hat{y}_n & \hat{x}_1 & \hat{x}_2 & \dots & \hat{x}_n \\ 0 & 0 & \dots & 0 & 2\hat{y}_1 & 2\hat{y}_2 & \dots & 2\hat{y}_n \end{bmatrix}. \tag{4.25}$$

4.1.2.5 Computation of the Line Moment Parameter

The line moment parameter l_3 is computed according to Equation (4.9). Thus, collecting the 3 homogeneous line parameters results in the line vector:

$$\boldsymbol{l} = \begin{bmatrix} l_1 \\ l_2 \\ -(\mu_x l_1 + \mu_y l_2) \end{bmatrix}. \tag{4.26}$$

According to the law of first order error propagation, the covariance matrix of the homogeneous 3-vector of line parameters is computed as:

$$\Lambda_{\boldsymbol{l}} = \mathsf{J}_{\boldsymbol{l}} \Lambda_{\hat{\boldsymbol{l}},\boldsymbol{\mu}} \mathsf{J}_{\boldsymbol{l}}^{T}. \tag{4.27}$$

Therein, the 4×4 covariance matrix $\Lambda_{\hat{\boldsymbol{l}},\boldsymbol{\mu}}$ is structured as:

$$\Lambda_{\hat{\boldsymbol{l}},\boldsymbol{\mu}} = \begin{bmatrix} \Lambda_{\hat{\boldsymbol{l}}} & 0 \\ 0 & \Lambda_{\boldsymbol{\mu}} \end{bmatrix}, \tag{4.28}$$

with 0 denoting a 2×2 matrix of 0's, which represents the non-existence of covariances between the centroid coordinates and the line orientation parameters. Taking into account the order of the input parameters in $\Lambda_{\hat{\boldsymbol{l}},\boldsymbol{\mu}}$, i.e.: l_1, l_2, μ_x and μ_y, the Jacobian matrix $\mathsf{J}_{\boldsymbol{l}}$ results in:

$$\mathsf{J}_{\boldsymbol{l}} = \begin{bmatrix} 1 & 0 & 0 & 0 \\ 0 & 1 & 0 & 0 \\ -\mu_x & -\mu_y & -l_1 & -l_2 \end{bmatrix}. \tag{4.29}$$

4.1.3 Error Propagation for Derived Quantities

4.1.3.1 The Geometric Distance of a Point to a Line

As outlined in Section 3.1.2.2, the signed geometric distance of a point $\boldsymbol{p} = [x_p, y_p, w_p]^T$ to a line with the vector of normalized line parameters, $\boldsymbol{l} = [l_1, l_2, l_3]^T$, is given as:

$$d = x_p l_1 + y_p l_2 + w_p l_3. \tag{4.30}$$

The variance associated with d is calculated by application of the law of first order error propagation as:

$$\sigma_d^2 = \mathsf{J}_d \Lambda_{\boldsymbol{p},\boldsymbol{l}} \mathsf{J}_d^T. \tag{4.31}$$

Therein, the combined covariance matrix $\Lambda_{\boldsymbol{p},\boldsymbol{l}}$ is incorporated, which is structured as:

$$\Lambda_{\boldsymbol{p},\boldsymbol{l}} = \begin{bmatrix} \Lambda_{\boldsymbol{p}} & 0 \\ 0 & \Lambda_{\boldsymbol{l}} \end{bmatrix}. \tag{4.32}$$

Thus, it is assumed that there are no covariances existing between the homogeneous coordinates of $\boldsymbol{p}$ and $\boldsymbol{l}$. The required Jacobian matrix J_d is finally obtained as:

$$\mathsf{J}_d = \begin{bmatrix} l_1 & l_2 & l_3 & x_p & y_p & w_p \end{bmatrix} = \begin{bmatrix} \boldsymbol{l}^T & \boldsymbol{p}^T \end{bmatrix}. \tag{4.33}$$

Note that the computation of the signed geometric distance of a point to a line represents a function linear in the line parameters. Thus, the error propagation specified by Equation (4.31) is exact.

4.1.3.2 The Point of Intersection of Two Lines

Given two lines, ${}_1\boldsymbol{l} = [{}_1l_1,\ {}_1l_2,\ {}_1l_3]^T$ and ${}_2\boldsymbol{l} = [{}_2l_1,\ {}_2l_2,\ {}_2l_3]^T$, together with their associated covariance matrices, $\Lambda_{{}_1\boldsymbol{l}}$ and $\Lambda_{{}_2\boldsymbol{l}}$, respectively. The homogeneous coordinates of the point of intersection of the two lines, $\boldsymbol{p}$, are calculated as the cross product of the homogeneous line vectors:

$$\boldsymbol{p} = \begin{bmatrix} x_p \\ y_p \\ w_p \end{bmatrix} = {}_1\boldsymbol{l} \times {}_2\boldsymbol{l} = \begin{bmatrix} {}_1l_2\ {}_2l_3 - {}_1l_3\ {}_2l_2 \\ {}_1l_3\ {}_2l_1 - {}_1l_1\ {}_2l_3 \\ {}_1l_1\ {}_2l_2 - {}_1l_2\ {}_2l_1 \end{bmatrix}. \tag{4.34}$$

The covariance matrix associated with $\boldsymbol{p}$ is computed according to:

$$\Lambda_{\boldsymbol{p}} = \mathsf{J}_{\boldsymbol{p}} \Lambda_{{}_1\boldsymbol{l},\,{}_2\boldsymbol{l}} \mathsf{J}_{\boldsymbol{p}}^T, \tag{4.35}$$

with the combined covariance matrix:

$$\Lambda_{{}_1\boldsymbol{l},\,{}_2\boldsymbol{l}} = \begin{bmatrix} \Lambda_{{}_1\boldsymbol{l}} & \mathsf{0} \\ \mathsf{0} & \Lambda_{{}_2\boldsymbol{l}} \end{bmatrix}, \tag{4.36}$$

and the Jacobian matrix:

$$\mathsf{J}_{\boldsymbol{p}} = \begin{bmatrix} 0 & {}_2l_3 & -{}_2l_2 & 0 & -{}_1l_3 & {}_1l_2 \\ -{}_2l_3 & 0 & {}_2l_1 & {}_1l_3 & 0 & -{}_1l_1 \\ {}_2l_2 & -{}_2l_1 & 0 & -{}_1l_2 & {}_1l_1 & 0 \end{bmatrix}. \tag{4.37}$$

The computation of the point of intersection of two lines represents a function linear in the line parameters. Thus, the error propagation specified by Equation (4.35) is exact.

4.1.4 Numerical Verification

A series of m images of a straight object edge was acquired with an industrial camera at conditions of repeatability[1]. See Figure 4.1 (left) for a sample of the image series.

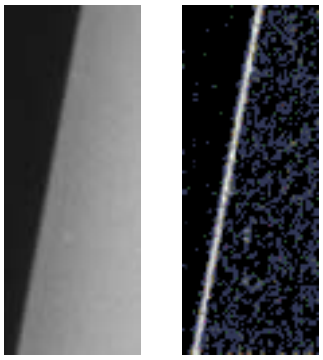

Figure 4.1: A sample of the image series acquired with an industrial camera (left) and the corresponding image of absolute gradient (right).

Each of the n pixel rows of the particular series images was evaluated independently to determine the location of a data point on the object edge. For that purpose, the following processing steps were executed on the particular series images:

1. computation of the absolute gradient image, as is depicted in Figure 4.1 (right),
2. extraction of the location of the maximum image gradient along each pixel row, and
3. computation of the 2-dimensional center-of-gravity within a 5×5 image window centered at the location of maximum image gradient.

[1] These comprise (a) the camera as well as the specimen to remain unmoved during the measurements, (b) constant parameters of the measurement setup, such as lighting intensity, lens aperture or exposure time, and (c) ideally constant environmental conditions, such as ambient light or vibrations.

4.1.4.1 Organisation of the Measurement Data

As a result, m sets of measurement points were obtained, whose x- and y-coordinates are organized in a common data matrix P of size $2n \times m$:

$$\mathsf{P} = \begin{bmatrix} x_{1,1} & x_{1,2} & \dots & x_{1,m} \\ x_{2,1} & x_{2,2} & \dots & x_{2,m} \\ \vdots & \vdots & \ddots & \vdots \\ x_{n,1} & x_{n,2} & \dots & x_{n,m} \\ y_{1,1} & y_{1,2} & \dots & y_{1,m} \\ y_{2,1} & y_{2,2} & \dots & y_{2,m} \\ \vdots & \vdots & \ddots & \vdots \\ y_{n,1} & y_{n,2} & \dots & y_{n,m} \end{bmatrix}. \tag{4.38}$$

In the following, a multivariate Gaussian distribution with mean vector $\boldsymbol{\mu_p}$ and covariance matrix $\Lambda_{\boldsymbol{p}}$ is assumed as the statistical model underlying the data points.

Given P, the vector of mean values, $\boldsymbol{\mu_p} = [\mu_{x_1}, \mu_{x_2}, \dots, \mu_{x_n}, \mu_{y_1}, \mu_{y_2}, \dots, \mu_{y_n}]^T$, was computed by evaluation of the particular rows of P, i.e.:

$$\begin{aligned} \mu_{x_i} &= \tfrac{1}{m} \sum_{k=1}^{m} x_{i,k}, \\ \mu_{y_i} &= \tfrac{1}{m} \sum_{k=1}^{m} y_{i,k}. \end{aligned} \tag{4.39}$$

Moreover, the $2n \times 2n$ covariance matrix $\Lambda_{\boldsymbol{p}}$ was computed according to:

$$\Lambda_{\boldsymbol{p}} = \frac{1}{m-1} \left(\hat{\mathsf{P}}\ \hat{\mathsf{P}}^T \right), \tag{4.40}$$

with $\hat{\mathsf{P}}$ representing the matrix of mean free point coordinates, which in turn was computed as: $\hat{\mathsf{P}} = \mathsf{P} - \boldsymbol{\mu_p} \otimes \mathbf{1}$. Therein, $\mathbf{1}$ represents an m-dimensional row vector of 1's, and the symbol $\otimes$ indicates the Kronecker matrix product.

Note that as a consequence of the evaluation procedure, the location of the particular data points is subject to measurement noise along the x- as well as the y-coordinate. Thus, the covariance matrix $\Lambda_{\boldsymbol{p}}$ is fully occupied.

4.1.4.2 Evaluation of the Measurement Data

The particular sets of data points collected in P were evaluated according to the procedure outlined in Section 4.1.1. As a result, m vectors of homogeneous line parameters, $\boldsymbol{l}_i$, $i = 1 \dots m$, were obtained. Then, the vector of mean line parameters, $\boldsymbol{\mu_l}$, as well as the 3×3 covariance matrix of the line parameters, $\Lambda_{\boldsymbol{l}}$, was computed. These act as reference values for the subsequent examinations:

$$\boldsymbol{\mu_l} = \begin{bmatrix} 0.98 \\ 0.18 \\ -28.97 \end{bmatrix}, \quad \Lambda_{\boldsymbol{l}} = \begin{bmatrix} 2.28\,10^{-9} & -1.24\,10^{-8} & 6.28\,10^{-7} \\ -1.24\,10^{-8} & 6.69\,10^{-8} & -3.40\,10^{-6} \\ 6.28\,10^{-7} & -3.40\,10^{-6} & 5.35\,10^{-4} \end{bmatrix}. \tag{4.41}$$

4.1.4.3 Monte-Carlo Experiments

In order to numerically verify the multivariate Gaussian distribution underlying the acquired measurement data, three Monte-Carlo experiments were executed. Thereby, three sets of 10^4 data points were synthetically generated (cf. Section 2.3.2) utilizing the mean vector $\boldsymbol{\mu_p}$ in combination with three different covariance matrices.

In the first covariance matrix, $\Lambda_{\boldsymbol{p}_1}$, merely the average coordinate variances $\bar{\sigma}_x^2 = \frac{1}{n}\sum_{i=1}^{n}\sigma_{x_i}^2$ and $\bar{\sigma}_y^2 = \frac{1}{n}\sum_{i=1}^{n}\sigma_{y_i}^2$ are incorporated, the covariances are neglected:

$$\Lambda_{\boldsymbol{p}_1} = \begin{bmatrix} \Lambda_{\boldsymbol{x}_1} & 0 \\ 0 & \Lambda_{\boldsymbol{y}_1} \end{bmatrix}, \quad \Lambda_{\boldsymbol{x}_1} = \begin{bmatrix} \bar{\sigma}_x^2 & 0 & \dots & 0 \\ 0 & \bar{\sigma}_x^2 & \dots & 0 \\ \vdots & \vdots & \ddots & \vdots \\ 0 & 0 & \dots & \bar{\sigma}_x^2 \end{bmatrix}, \; \Lambda_{\boldsymbol{y}_1} = \begin{bmatrix} \bar{\sigma}_y^2 & 0 & \dots & 0 \\ 0 & \bar{\sigma}_y^2 & \dots & 0 \\ \vdots & \vdots & \ddots & \vdots \\ 0 & 0 & \dots & \bar{\sigma}_y^2 \end{bmatrix}.$$

The second covariance matrix incorporates all of the individual variances of the point coordinates, but neglects the covariances between the coordinates:

$$\Lambda_{\boldsymbol{p}_2} = \begin{bmatrix} \Lambda_{\boldsymbol{x}_2} & 0 \\ 0 & \Lambda_{\boldsymbol{y}_2} \end{bmatrix}, \quad \Lambda_{\boldsymbol{x}_2} = \begin{bmatrix} \sigma_{x_1}^2 & 0 & \dots & 0 \\ 0 & \sigma_{x_2}^2 & \dots & 0 \\ \vdots & \vdots & \ddots & \vdots \\ 0 & 0 & \dots & \sigma_{x_n}^2 \end{bmatrix}, \; \Lambda_{\boldsymbol{y}_2} = \begin{bmatrix} \sigma_{y_1}^2 & 0 & \dots & 0 \\ 0 & \sigma_{y_2}^2 & \dots & 0 \\ \vdots & \vdots & \ddots & \vdots \\ 0 & 0 & \dots & \sigma_{y_n}^2 \end{bmatrix}.$$

Ultimately, the third Monte-Carlo experiment is based on the fully occupied covariance matrix as defined in Equation (4.40), i.e.: $\Lambda_{\boldsymbol{p}_3} = \Lambda_{\boldsymbol{p}}$.

After generating the sets of synthetical data points, the particular data sets were evaluated, i.e. a straight line was fitted to each set of data points according to the procedure outlined in Section 4.1.1. Furthermore, the vectors of average line parameters $\boldsymbol{\mu}_{\boldsymbol{l}_{MC,i}}$, $i = 1 \dots 3$, as well as the covariance matrices $\Lambda_{\boldsymbol{l}_{MC,i}}$, $i = 1 \dots 3$, were determined.

4.1.4.4 Comparison with the Results of Analytic Computation

The covariance matrices $\Lambda_{\boldsymbol{p}_i}$, $i = 1 \dots 3$, specified for the Monte-Carlo experiments, were now taken as a basis for computing first order error propagation as presented in Section 4.1.2. As a result, the covariance matrix associated with the 3-vector of homogeneous line parameters was computed analytically three times. In Table 4.1, the covariance matrices obtained from the analytic computations, $\Lambda_{\boldsymbol{l}_{A,i}}$, are opposed to the covariance matrices determined by the Monte-Carlo experiments.

Obviously, the covariance matrices are poorly conditioned as a result of the variance associated with the line moment parameter dominating the other elements of the particular covariance matrices. Thus, it is inappropriate to compare the covariance matrices by means of matrix norms. Hence, the results are analyzed qualitatively.

Comparing the covariance matrices listed in Table 4.1 with $\Lambda_{\boldsymbol{l}}$, the covariance matrix determined by evaluation of the measurement data (see Equation (4.41)), the following conclusions can be drawn:

i	$\Lambda_{\boldsymbol{l}_{MC,i}}$	$\Lambda_{\boldsymbol{l}_{A,i}}$
1	$\begin{bmatrix} 0.99\,10^{-9} & -5.36\,10^{-9} & 3.36\,10^{-7} \\ -5.36\,10^{-9} & 2.90\,10^{-8} & -1.82\,10^{-6} \\ 3.36\,10^{-7} & -1.82\,10^{-6} & 1.56\,10^{-4} \end{bmatrix}$	$\begin{bmatrix} 0.98\,10^{-9} & -5.28\,10^{-9} & 3.32\,10^{-7} \\ -5.28\,10^{-9} & 2.86\,10^{-8} & -1.80\,10^{-6} \\ 3.32\,10^{-7} & -1.80\,10^{-6} & 1.54\,10^{-4} \end{bmatrix}$
2	$\begin{bmatrix} 1.02\,10^{-9} & -5.54\,10^{-9} & 3.50\,10^{-7} \\ -5.54\,10^{-9} & 2.99\,10^{-8} & -1.89\,10^{-6} \\ 3.50\,10^{-7} & -1.89\,10^{-6} & 1.62\,10^{-4} \end{bmatrix}$	$\begin{bmatrix} 1.03\,10^{-9} & -5.59\,10^{-9} & 3.51\,10^{-7} \\ -5.59\,10^{-9} & 3.03\,10^{-8} & -1.90\,10^{-6} \\ 3.51\,10^{-7} & -1.90\,10^{-6} & 1.61\,10^{-4} \end{bmatrix}$
3	$\begin{bmatrix} 2.26\,10^{-9} & -1.22\,10^{-8} & 6.11\,10^{-7} \\ -1.22\,10^{-8} & 6.63\,10^{-8} & -3.31\,10^{-6} \\ 6.11\,10^{-7} & -3.31\,10^{-6} & 5.16\,10^{-4} \end{bmatrix}$	$\begin{bmatrix} 2.28\,10^{-9} & -1.24\,10^{-8} & 7.77\,10^{-7} \\ -1.24\,10^{-8} & 6.69\,10^{-8} & -4.20\,10^{-6} \\ 7.77\,10^{-7} & -4.20\,10^{-6} & 6.36\,10^{-4} \end{bmatrix}$

Table 4.1: Covariance matrices associated with a homogeneous 3-vector of line parameters, determined by Monte-Carlo experiments (left column) and application of first order error propagation (right column).

1. The elements of corresponding covariance matrices $\Lambda_{\boldsymbol{l}_{MC,i}}$ and $\Lambda_{\boldsymbol{l}_{A,i}}$ exhibit very small deviations to one another. Thus, the approach outlined in Section 4.1.2 can be considered as a suitable method for analytically computing the uncertainty associated with a line fitted to a set of data points.

2. The deviations of $\Lambda_{\boldsymbol{l}_{MC,3}}$ and $\Lambda_{\boldsymbol{l}_{A,3}}$ with respect to $\Lambda_{\boldsymbol{l}}$ are significantly smaller than those of $\Lambda_{\boldsymbol{l}_{MC,1}}$ and $\Lambda_{\boldsymbol{l}_{A,1}}$ respectively $\Lambda_{\boldsymbol{l}_{MC,2}}$ and $\Lambda_{\boldsymbol{l}_{A,2}}$. Thus, the fully occupied covariance matrix of the data points, $\Lambda_{\boldsymbol{p}_3}$, is more appropriate to model the stochastic nature of the data points than the two simplified models, $\Lambda_{\boldsymbol{p}_1}$ and $\Lambda_{\boldsymbol{p}_2}$.

The three plots listed in Figure 4.2 visualize the 99.9% line confidence envelopes represented by the covariance matrices $\Lambda_{\boldsymbol{l}_{A,1}}$, $\Lambda_{\boldsymbol{l}_{A,2}}$ and $\Lambda_{\boldsymbol{l}_{A,3}}$ opposed to the 99.9% line confidence envelope described by $\Lambda_{\boldsymbol{l}}$. The plots of the confidence envelopes represented by the covariance matrices $\Lambda_{\boldsymbol{l}_{MC,1}}$, $\Lambda_{\boldsymbol{l}_{MC,2}}$ and $\Lambda_{\boldsymbol{l}_{MC,3}}$ are omitted, as they are optically not distinguishable from those of the analytic computations. Moreover, the 99.9% point confidence envelope of a sample data point is plotted to illustrate the underlying perturbation model described by $\Lambda_{\boldsymbol{p}_1}$, $\Lambda_{\boldsymbol{p}_2}$ and $\Lambda_{\boldsymbol{p}_3}$. As can be seen in the rightmost plot, the confidence envelope described by $\Lambda_{\boldsymbol{l}_{A,3}}$ is optically identical to that corresponding to $\Lambda_{\boldsymbol{l}}$.

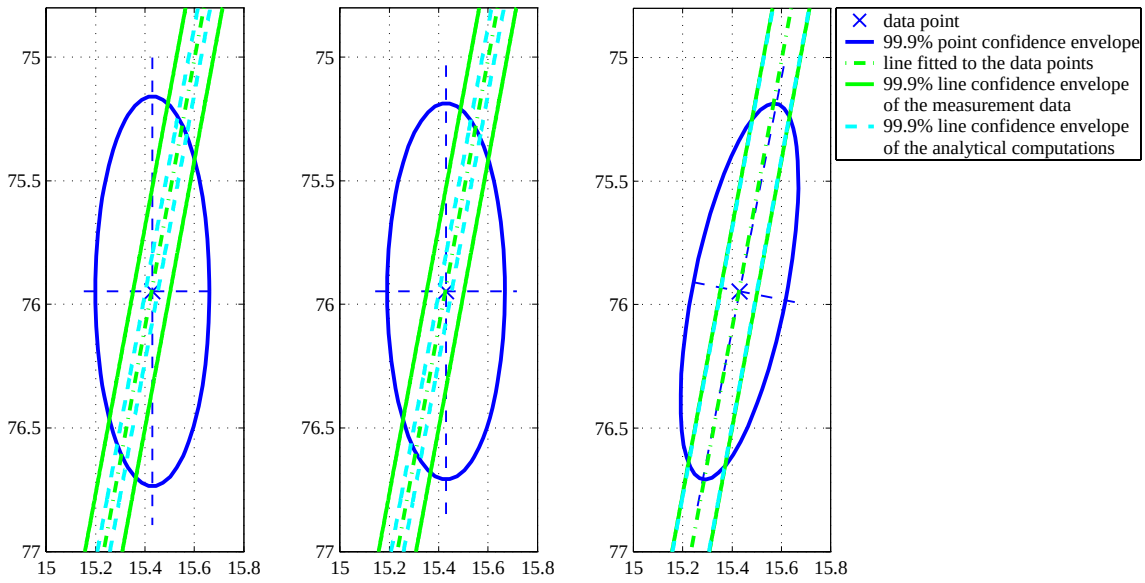

Figure 4.2: Confidence envelopes of the line envelopes described by the covariance matrices $\Lambda_{\boldsymbol{l}_{A,1}}$ (left), $\Lambda_{\boldsymbol{l}_{A,2}}$ (central) and $\Lambda_{\boldsymbol{l}_{A,3}}$ (right), opposed to that represented by $\Lambda_{\boldsymbol{l}}$.

4.2 Fitting a Pair of Parallel Lines to two Sets of Uncertain Data Points

4.2.1 The Fitting Algorithm

The line equations of two parallel lines, represented by the 3-vectors of homogeneous line parameters $\boldsymbol{l}_1 = \begin{bmatrix} l_1 & l_2 & {}_1l_3 \end{bmatrix}^T$ and $\boldsymbol{l}_2 = \begin{bmatrix} l_1 & l_2 & {}_2l_3 \end{bmatrix}^T$ respectively, are given as:

$$\begin{aligned} {}_1\boldsymbol{p}^T\boldsymbol{l}_1 &= {}_1xl_1 + {}_1yl_2 + {}_1l_3 = 0, \\ {}_2\boldsymbol{p}^T\boldsymbol{l}_2 &= {}_2xl_1 + {}_2yl_2 + {}_2l_3 = 0. \end{aligned} \tag{4.42}$$

Therein, ${}_1\boldsymbol{p} = \begin{bmatrix} {}_1x & {}_1y & 1 \end{bmatrix}^T$ and ${}_2\boldsymbol{p} = \begin{bmatrix} {}_2x & {}_2y & 1 \end{bmatrix}^T$ denote vectors of normalized homogeneous coordinates of points lying on the respective lines. Given two sets of data points, ${}_1\boldsymbol{p}_i = \begin{bmatrix} {}_1x_i & {}_1y_i & 1 \end{bmatrix}^T$, $i = 1 \dots n_1$, and ${}_2\boldsymbol{p}_j = \begin{bmatrix} {}_2x_j & {}_2y_j & 1 \end{bmatrix}^T$, $j = 1 \dots n_2$, fitting a pair of parallel lines to the data points is formulated as:

$$\mathsf{D}\boldsymbol{l}_{12} = \begin{bmatrix} {}_1x_1 & {}_1y_1 & 1 & 0 \\ {}_1x_2 & {}_1y_2 & 1 & 0 \\ \vdots & \vdots & \vdots & \vdots \\ {}_1x_{n_1} & {}_1y_{n_1} & 1 & 0 \\ {}_2x_1 & {}_2y_1 & 0 & 1 \\ {}_2x_2 & {}_2y_2 & 0 & 1 \\ \vdots & \vdots & \vdots & \vdots \\ {}_2x_{n_2} & {}_2y_{n_2} & 0 & 1 \end{bmatrix} \begin{bmatrix} l_1 \\ l_2 \\ {}_1l_3 \\ {}_2l_3 \end{bmatrix} = \begin{bmatrix} {}_1r_1 \\ {}_1r_2 \\ \vdots \\ {}_1r_{n_1} \\ {}_2r_1 \\ {}_2r_2 \\ \vdots \\ {}_2r_{n_2} \end{bmatrix}, \tag{4.43}$$

with the design matrix D and the vector $\boldsymbol{l}_{12}$ holding the line orientation parameters

common for both lines, l_1 and l_2, as well as the two line moment parameters ${}_1l_3$ and ${}_2l_3$. This can be rewritten as the linear least squares problem:

$$\min_{\boldsymbol{l}_{12}} \|\mathsf{D}\boldsymbol{l}_{12}\| \quad \text{subject to:} \quad \sqrt{l_1^2 + l_2^2} = 1. \tag{4.44}$$

Obviously, the particular columns of D exhibit differing statistical nature. The columns of 0's and 1's are statistically invariant, whereas the other two columns are not. Thus, O'Leary et al. [45] suggested to partition the design matrix as follows:

$$\mathsf{D} = \left[\begin{array}{c|cc} {}_1\mathsf{D}_1 & {}_1\mathsf{D}_0 & \mathsf{0} \\ \hline {}_2\mathsf{D}_1 & \mathsf{0} & {}_2\mathsf{D}_0 \end{array}\right] = \left[\begin{array}{cc|cc} {}_1x_1 & {}_1y_1 & 1 & 0 \\ {}_1x_2 & {}_1y_2 & 1 & 0 \\ \vdots & \vdots & \vdots & \vdots \\ {}_1x_{n_1} & {}_1y_{n_1} & 1 & 0 \\ \hline {}_2x_1 & {}_2y_1 & 0 & 1 \\ {}_2x_2 & {}_2y_2 & 0 & 1 \\ \vdots & \vdots & \vdots & \vdots \\ {}_2x_{n_2} & {}_2y_{n_2} & 0 & 1 \end{array}\right]. \tag{4.45}$$

After applying orthogonal projection of ${}_1\mathsf{D}_1$ onto ${}_1\mathsf{D}_0$ as well as ${}_2\mathsf{D}_1$ onto ${}_2\mathsf{D}_0$, a new design matrix $\hat{\mathsf{D}}$ with statistically uniform columns is obtained:

$$\hat{\mathsf{D}} = \begin{bmatrix} {}_1x_1 - {}_1\mu_x & {}_1y_1 - {}_1\mu_y \\ {}_1x_2 - {}_1\mu_x & {}_1y_2 - {}_1\mu_y \\ \vdots & \vdots \\ {}_1x_{n_1} - {}_1\mu_x & {}_1y_{n_1} - {}_1\mu_y \\ {}_2x_1 - {}_2\mu_x & {}_2y_1 - {}_2\mu_y \\ {}_2x_2 - {}_2\mu_x & {}_2y_2 - {}_2\mu_y \\ \vdots & \vdots \\ {}_2x_{n_2} - {}_2\mu_x & {}_2y_{n_2} - {}_2\mu_y \end{bmatrix}. \tag{4.46}$$

As can be seen, the columns of $\hat{\mathsf{D}}$ hold the mean-free coordinates of the given data points, with the mean values being subtracted:

$$\begin{aligned} {}_1\mu_x &= \frac{1}{n_1}\sum_{i=1}^{n_1} {}_1x_i, \\ {}_1\mu_y &= \frac{1}{n_1}\sum_{i=1}^{n_1} {}_1y_i, \end{aligned} \tag{4.47}$$

$$\begin{aligned} {}_2\mu_x &= \frac{1}{n_2}\sum_{j=1}^{n_2} {}_2x_j, \\ {}_2\mu_y &= \frac{1}{n_2}\sum_{j=1}^{n_2} {}_2y_j. \end{aligned} \tag{4.48}$$

The linear least squares problem to be solved now becomes:

$$\min_{\hat{\boldsymbol{l}}} \|\hat{\mathsf{D}}\hat{\boldsymbol{l}}\| \quad \text{subject to:} \quad \|\hat{\boldsymbol{l}}\| = 1, \tag{4.49}$$

with $\hat{\boldsymbol{l}} = \begin{bmatrix} l_1 & l_2 \end{bmatrix}^T$ denoting the vector of line orientation parameters. This again can be solved by singular value decomposition of the design matrix and extracting the right singular vector corresponding to the smallest singular value of $\hat{\mathsf{D}}$.

The line moment parameters, ${}_1l_3$ and ${}_2l_3$, are finally obtained by back-substituting the centroid coordinates of the data points into the respective line equations. They result in:

$$\begin{aligned} {}_1l_3 &= -({}_1\mu_x l_1 + {}_1\mu_y l_2), \\ {}_2l_3 &= -({}_2\mu_x l_1 + {}_2\mu_y l_2). \end{aligned} \tag{4.50}$$

Summarizing, the algorithm for fitting a pair of parallel lines to two sets of uncertain data points comprises (analogously to fitting a single line) the following steps:

1. computation of the centroid coordinates of the two sets of data points,
2. calculation of mean-free data points and setup of the design matrix $\hat{\mathsf{D}}$ according to Equation (4.46),
3. estimation of the line orientation parameters l_1 and l_2 by singular value decomposition of $\hat{\mathsf{D}}$, and
4. computation of the line moment parameters ${}_1l_3$ and ${}_2l_3$ according to Equation (4.50).

4.2.2 First Order Error Propagation for the Fitting Algorithm

4.2.2.1 Organisation of the Data Points

Considering two sets of n_1 and n_2 data points, perturbed by measurement noise. Along the lines of Section 4.1.2, the x- and y-coordinates of the data points, ${}_1x_i$ and ${}_1y_i$, $i = 1 \dots n_1$, respectively ${}_2x_j$ and ${}_2y_j$, $j = 1 \dots n_2$, are to be understood as expectation values of the random measurement process in the following. They are collected in a common expectation vector $\boldsymbol{p}$ as follows:

$$\boldsymbol{p} = \begin{bmatrix} {}_1x_1 & \dots & {}_1x_{n_1} & {}_2x_1 & \dots & {}_2x_{n_2} & {}_1y_1 & \dots & {}_1y_{n_1} & {}_2y_1 & \dots & {}_2y_{n_2} \end{bmatrix}^T. \tag{4.51}$$

Introducing the sum $n = n_1 + n_2$, the $2n \times 2n$ covariance matrix characterizing the Gaussian probability density function underlying the measurement process is structured as follows:

$$\Sigma_{\boldsymbol{pp}} = \begin{bmatrix} \Sigma_{{}_1\boldsymbol{xx}} & \mathsf{C}_{{}_1\boldsymbol{x}{}_2\boldsymbol{x}} & \mathsf{C}_{{}_1\boldsymbol{x}{}_1\boldsymbol{y}} & \mathsf{C}_{{}_1\boldsymbol{x}{}_2\boldsymbol{y}} \\ \mathsf{C}^T_{{}_1\boldsymbol{x}{}_2\boldsymbol{x}} & \Sigma_{{}_2\boldsymbol{xx}} & \mathsf{C}_{{}_2\boldsymbol{x}{}_1\boldsymbol{y}} & \mathsf{C}_{{}_2\boldsymbol{x}{}_2\boldsymbol{y}} \\ \mathsf{C}^T_{{}_1\boldsymbol{x}{}_1\boldsymbol{y}} & \mathsf{C}^T_{{}_2\boldsymbol{x}{}_1\boldsymbol{y}} & \Sigma_{{}_1\boldsymbol{yy}} & \mathsf{C}_{{}_1\boldsymbol{y}{}_2\boldsymbol{y}} \\ \mathsf{C}^T_{{}_1\boldsymbol{x}{}_2\boldsymbol{y}} & \mathsf{C}^T_{{}_2\boldsymbol{x}{}_2\boldsymbol{y}} & \mathsf{C}^T_{{}_1\boldsymbol{y}{}_2\boldsymbol{y}} & \Sigma_{{}_2\boldsymbol{yy}} \end{bmatrix}. \tag{4.52}$$

Therein, $\Sigma_{{}_1\boldsymbol{xx}}$ and $\Sigma_{{}_1\boldsymbol{yy}}$ denote the covariance matrices of the x- and y-coordinates of the first data set and analogously, $\Sigma_{{}_2\boldsymbol{xx}}$ and $\Sigma_{{}_2\boldsymbol{yy}}$ denote the covariance matrices of the x- and y-coordinates of the second data set. Furthermore, $\mathsf{C}_{{}_1\boldsymbol{x}{}_2\boldsymbol{x}}$, $\mathsf{C}_{{}_1\boldsymbol{x}{}_1\boldsymbol{y}}$, $\mathsf{C}_{{}_1\boldsymbol{x}{}_2\boldsymbol{y}}$, $\mathsf{C}_{{}_2\boldsymbol{x}{}_1\boldsymbol{y}}$, $\mathsf{C}_{{}_2\boldsymbol{x}{}_2\boldsymbol{y}}$ and $\mathsf{C}_{{}_1\boldsymbol{y}{}_2\boldsymbol{y}}$ term matrices of covariances possibly existing between the x- and y-coordinates of the respective sets of data points.

4.2.2.2 Computing the Centroid Coordinates

The centroid coordinates of the two sets of data points are collected in a common vector as follows:

$$\boldsymbol{\mu} = \begin{bmatrix} \mu_{1\boldsymbol{x}} & \mu_{2\boldsymbol{x}} & \mu_{1\boldsymbol{y}} & \mu_{2\boldsymbol{y}} \end{bmatrix}^T, \tag{4.53}$$

whereas the particular mean values are calculated according to Equation (4.48). Note that this structure enables the computation of a fully occupied 4×4 covariance matrix associated with $\boldsymbol{\mu}$ by application of the law of first order error propagation:

$$\Lambda_{\boldsymbol{\mu}} = \mathsf{J}_{\boldsymbol{\mu}} \Lambda_{\boldsymbol{p}} \mathsf{J}_{\boldsymbol{\mu}}{}^T, \tag{4.54}$$

with $\mathsf{J}_{\boldsymbol{\mu}}$ denoting the $4 \times 2n$ Jacobian matrix:

$$\mathsf{J}_{\boldsymbol{\mu}} = \begin{bmatrix} \mathsf{J}_{\mu_{1\boldsymbol{x}}} & \mathbf{0} & \mathbf{0} & \mathbf{0} \\ \mathbf{0} & \mathsf{J}_{\mu_{2\boldsymbol{x}}} & \mathbf{0} & \mathbf{0} \\ \mathbf{0} & \mathbf{0} & \mathsf{J}_{\mu_{1\boldsymbol{y}}} & \mathbf{0} \\ \mathbf{0} & \mathbf{0} & \mathbf{0} & \mathsf{J}_{\mu_{2\boldsymbol{y}}} \end{bmatrix}, \quad \begin{aligned} \mathsf{J}_{\mu_{1\boldsymbol{x}}} &= \mathsf{J}_{\mu_{1\boldsymbol{y}}} = \tfrac{1}{n_1}\, \mathbf{1}_{n_1}, \\ \mathsf{J}_{\mu_{2\boldsymbol{x}}} &= \mathsf{J}_{\mu_{2\boldsymbol{y}}} = \tfrac{1}{n_2}\, \mathbf{1}_{n_2}. \end{aligned} \tag{4.55}$$

Therein, $\mathbf{1}_{n_1}$ and $\mathbf{1}_{n_2}$ term row vectors of 1's, having length n_1 and n_2, respectively. Note that the computation of vector $\boldsymbol{\mu}$ represents a function linear in the input parameters, i.e. the point coordinates. Thus, the error propagation specified by Equation (4.54) is exact.

4.2.2.3 Calculation of Mean-Free Data Points

The mean-free coordinates of the data points are calculated as:

$$\begin{aligned} {}_1\hat{x}_i &= {}_1x_i - {}_1\mu_x, \\ {}_1\hat{y}_i &= {}_1y_i - {}_1\mu_y, \end{aligned} \tag{4.56}$$

$$\begin{aligned} {}_2\hat{x}_i &= {}_2x_i - {}_2\mu_x, \\ {}_2\hat{y}_i &= {}_2y_i - {}_2\mu_y, \end{aligned} \tag{4.57}$$

and are collected in a common vector,

$$\hat{\boldsymbol{p}} = \begin{bmatrix} {}_1\hat{x}_1 & \dots & {}_1\hat{x}_{n_1} & {}_2\hat{x}_1 & \dots & {}_2\hat{x}_{n_2} & {}_1\hat{y}_1 & \dots & {}_1\hat{y}_{n_1} & {}_2\hat{y}_1 & \dots & {}_2\hat{y}_{n_2} \end{bmatrix}^T. \tag{4.58}$$

The covariance matrix $\Lambda_{\hat{\boldsymbol{p}}}$ associated with $\hat{\boldsymbol{p}}$ is computed according to the law of first order error propagation as:

$$\Lambda_{\hat{\boldsymbol{p}}} = \mathsf{J}_{\hat{\boldsymbol{p}}} \Lambda_{\boldsymbol{p}} \mathsf{J}_{\hat{\boldsymbol{p}}}{}^T, \tag{4.59}$$

with the $2n \times 2n$ Jacobian matrix $\mathsf{J}_{\hat{\boldsymbol{p}}}$ being structured as:

$$\mathsf{J}_{\hat{\boldsymbol{p}}} = \begin{bmatrix} \mathsf{J}_{1\hat{x}} & 0 & 0 & 0 \\ 0 & \mathsf{J}_{2\hat{x}} & 0 & 0 \\ 0 & 0 & \mathsf{J}_{1\hat{y}} & 0 \\ 0 & 0 & 0 & \mathsf{J}_{2\hat{y}} \end{bmatrix}, \quad \begin{aligned} \mathsf{J}_{1\hat{x}} &= \mathsf{J}_{1\hat{y}} = \mathrm{I}_{n_1} - \tfrac{1}{n_1}\, 1, \\ \mathsf{J}_{2\hat{x}} &= \mathsf{J}_{2\hat{y}} = \mathrm{I}_{n_2} - \tfrac{1}{n_2}\, 1. \end{aligned} \tag{4.60}$$

Therein, I_{n_1} and I_{n_2} term identity matrices of dimensionality $n_1 \times n_1$ and $n_2 \times n_2$, respectively. As the computation of mean-free point coordinates represents a linear operation, the error propagation specified by Equation (4.59) is exact.

4.2.2.4 Computation of the Line Orientation Parameters

Computation of the 2-vector of line orientation parameters $\hat{\boldsymbol{l}}$ is formulated as the following linear least squares problem:

$$\min_{\hat{\boldsymbol{l}}} \|\hat{\mathsf{D}}\hat{\boldsymbol{l}}\| \quad \text{subject to:} \quad \|\hat{\boldsymbol{l}}\| = 1, \tag{4.61}$$

with the design matrix $\hat{\mathsf{D}}$, which is composed as in Equation (4.46). Applying the law of first order error propagation, the covariance matrix associated with $\hat{\boldsymbol{l}}$ is estimated as:

$$\Lambda_{\hat{\boldsymbol{l}}} \approx \mathsf{J}_{\hat{\boldsymbol{l}}} \Lambda_{\hat{\boldsymbol{p}}} \mathsf{J}_{\hat{\boldsymbol{l}}}^T, \tag{4.62}$$

where $\mathsf{J}_{\hat{\boldsymbol{l}}}$ denotes the Jacobian matrix of the implicit function $\boldsymbol{\Phi}\left(\hat{\boldsymbol{p}}, \hat{\boldsymbol{l}}\right) = \mathsf{A}\hat{\boldsymbol{l}} = \mathbf{0}$. Referring to Section 2.3.3.2, $\mathsf{J}_{\hat{\boldsymbol{l}}}$ is approximated by:

$$\mathsf{J}_{\hat{\boldsymbol{l}}} \approx -\mathsf{A}^{+} \frac{\partial \boldsymbol{\Phi}}{\partial \mathsf{A}} \frac{\partial \mathsf{A}}{\partial \hat{\boldsymbol{p}}}, \tag{4.63}$$

with the 2×2 scatter matrix $\mathsf{A} = \hat{\mathsf{D}}^T \hat{\mathsf{D}}$. Furthermore, the required matrices $\frac{\partial \boldsymbol{\Phi}}{\partial \mathsf{A}}$ and $\frac{\partial \mathsf{A}}{\partial \hat{\boldsymbol{p}}}$ are computed as:

$$\frac{\partial \Phi}{\partial \mathsf{A}} = \begin{bmatrix} l_1 & l_2 & 0 & 0 \\ 0 & 0 & l_1 & l_2 \end{bmatrix}, \text{ and:} \tag{4.64}$$

$$\frac{\partial \mathsf{A}}{\partial \hat{\boldsymbol{p}}} = \begin{bmatrix} {}_2\hat{x}_1 & \dots & {}_2\hat{x}_{n_1} & {}_1\hat{x}_1 & \dots & {}_1\hat{x}_{n_2} & 0 & \dots & 0 & 0 & \dots & 0 \\ {}_2\hat{y}_1 & \dots & {}_2\hat{y}_{n_1} & {}_1\hat{y}_1 & \dots & {}_1\hat{y}_{n_2} & {}_2\hat{x}_1 & \dots & {}_2\hat{x}_{n_1} & {}_1\hat{x}_1 & \dots & {}_1\hat{x}_{n_2} \\ {}_2\hat{y}_1 & \dots & {}_2\hat{y}_{n_1} & {}_1\hat{y}_1 & \dots & {}_1\hat{y}_{n_2} & {}_2\hat{x}_1 & \dots & {}_2\hat{x}_{n_1} & {}_1\hat{x}_1 & \dots & {}_1\hat{x}_{n_2} \\ 0 & \dots & 0 & 0 & \dots & 0 & {}_2\hat{y}_1 & \dots & {}_2\hat{y}_{n_1} & {}_1\hat{y}_1 & \dots & {}_1\hat{y}_{n_2} \end{bmatrix}. \tag{4.65}$$

4.2.2.5 Computation of the Line Moment Parameters

The line moment parameters ${}_1l_3$ and ${}_2l_3$ are computed according to Equation (4.50). The 3×3 covariance matrices associated with the parameters of the two lines can be computed separately according to the formulae outlined in Section 4.1.2.5. However, the covariance between the two line moment parameters would then remain unconsidered.

This can be avoided by computing the covariance matrix $\Lambda_{\boldsymbol{l}}$ associated with a vector of line parameters, which is structured as follows:

$$\boldsymbol{l} = \begin{bmatrix} l_1 \\ l_2 \\ {}_1l_3 \\ {}_2l_3 \end{bmatrix} = \begin{bmatrix} l_1 \\ l_2 \\ -(\mu_{1x} l_1 + \mu_{1y} l_2) \\ -(\mu_{2x} l_1 + \mu_{2y} l_2) \end{bmatrix}. \tag{4.66}$$

Then, the 4×4 covariance matrix $\Lambda_{\boldsymbol{l}}$ is computed according to the law of first order error propagation as:

$$\Lambda_{\boldsymbol{l}} = \mathsf{J}_{\boldsymbol{l}} \Lambda_{\hat{\boldsymbol{l}},\boldsymbol{\mu}} \mathsf{J}_{\boldsymbol{l}}^T. \tag{4.67}$$

Therein, a 6×6 covariance matrix $\Lambda_{\hat{\boldsymbol{l}},\boldsymbol{\mu}}$ is incorporated, which is organized as:

$$\Lambda_{\hat{\boldsymbol{l}},\boldsymbol{\mu}} = \begin{bmatrix} \Lambda_{\hat{\boldsymbol{l}}} & 0 \\ 0 & \Lambda_{\boldsymbol{\mu}} \end{bmatrix}. \tag{4.68}$$

Taking into account the order of parameters in $\Lambda_{\hat{\boldsymbol{l}},\boldsymbol{\mu}}$, i.e.: l_1, l_2, μ_{1x}, μ_{2x}, μ_{1y} and μ_{2y}, the 4×6 Jacobian matrix $\mathsf{J}_{\boldsymbol{l}}$ results in:

$$\mathsf{J}_{\boldsymbol{l}} = \begin{bmatrix} 1 & 0 & 0 & 0 & 0 & 0 \\ 0 & 1 & 0 & 0 & 0 & 0 \\ -\mu_{1x} & -\mu_{1y} & -l_1 & 0 & -l_2 & 0 \\ -\mu_{2x} & -\mu_{2y} & 0 & -l_1 & 0 & -l_2 \end{bmatrix}. \tag{4.69}$$

The computation of the line moment parameters represents a function linear in the input parameters, i.e. the line orientation parameters as well as the centroid coordinates. Thus, the error propagation specified by Equation (4.67) is exact.

4.2.3 Error Propagation for Derived Quantities

4.2.3.1 The Orthogonal Distance between two Parallel Lines

Referring to Section 3.1.3, the signed orthogonal distance d between two parallel lines is calculated as:

$$\begin{aligned} d &= {}_1l_3 - {}_2l_3, \\ &= -(\mu_{1x}l_1 + \mu_{1y}l_2) + (\mu_{2x}l_1 + \mu_{2y}l_2), \\ &= (\mu_{2x} - \mu_{1x})\, l_1 + (\mu_{2y} - \mu_{1y})\, l_2. \end{aligned} \tag{4.70}$$

The variance associated with d is analytically computed according to the law of first order error propagation as:

$$\sigma_{d_A}^2 = \mathsf{J}_d \Lambda_{\hat{\boldsymbol{l}},\boldsymbol{\mu}} \mathsf{J}_d{}^T. \tag{4.71}$$

Therein, the 6×6 covariance matrix $\Lambda_{\hat{\boldsymbol{l}},\boldsymbol{\mu}}$ is structured as defined in Equation (4.68). Furthermore, the 1×6 Jacobian matrix J_d is determined as:

$$\mathsf{J}_d = \begin{bmatrix} \mu_{2x} - \mu_{1x} & \mu_{2y} - \mu_{1y} & -l_1 & l_1 & -l_2 & l_2 \end{bmatrix}. \tag{4.72}$$

Note that the computation of the orthogonal distance between two lines represents a function linear in the input parameters, i.e. the line parameters as well as the centroid coordinates. Thus, the error propagation specified by Equation (4.71) is exact.

4.2.3.2 The Line Central to two Parallel Lines

As outlined in Section 3.1.3, the homogeneous vector of a line ${}_c\boldsymbol{l}$ being central to two parallel lines ${}_1\boldsymbol{l}$ respectively ${}_2\boldsymbol{l}$ is computed as:

$${}_c\boldsymbol{l} = \begin{bmatrix} {}_cl_1 \\ {}_cl_2 \\ {}_cl_3 \end{bmatrix} = \begin{bmatrix} {}_1l_1 \\ {}_1l_2 \\ \frac{1}{2}\left({}_1l_3 + {}_2l_3\right) \end{bmatrix}. \tag{4.73}$$

The covariance matrix associated with ${}_c\boldsymbol{l}$ can be determined according to the law of first order error propagation:

$$\Lambda_{c\boldsymbol{l}} = \mathsf{J}_{c\boldsymbol{l}} \Lambda_{\boldsymbol{l}} \mathsf{J}_{c\boldsymbol{l}}{}^{T}. \tag{4.74}$$

Therein, $\Lambda_{\boldsymbol{l}}$ terms the 4×4 covariance matrix of line parameters as in Equation (4.67). Furthermore, the required 3×4 Jacobian matrix $\mathsf{J}_{c\boldsymbol{l}}$ results in:

$$\mathsf{J}_{c\boldsymbol{l}} = \begin{bmatrix} 1 & 0 & 0 & 0 \\ 0 & 1 & 0 & 0 \\ 0 & 0 & \frac{1}{2} & \frac{1}{2} \end{bmatrix}. \tag{4.75}$$

The operation given in Equation (4.73) is linear in the input parameters, i.e. the set of line parameters. Thus the error propagation specified in Equation (4.74) is exact.

4.2.4 Numerical Verification

A series of m images of an object with two parallel edges was acquired with an industrial camera at conditions of repeatability[2]. See Figure 4.3 (left) for a sample of the image series.

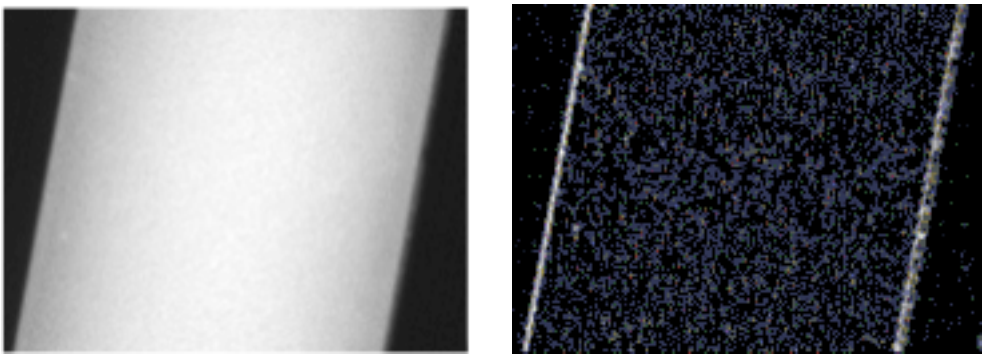

Figure 4.3: An image series was acquired with an industrial camera under conditions of repeatability. A sample of the image series showing an object with two parallel edges (left) and the corresponding image of absolute gradient (right).

Each of the n pixel rows of the particular series images was evaluated independently to determine the location of data points on the two object edges. For that purpose, the following processing steps were executed on the particular series images:

1. Computation of the absolute gradient image as depicted in Figure 4.3 (right).
2. Extraction of the locations of maximum image gradient along each pixel row, whereas the first and second half of the pixel rows were handled separately in order to obtain data points on the left and right object edge, respectively.
3. Computation of the center-of-gravity of the gradient around the extracted locations of maximum image gradient. Two different methods were investigated:
   (a) 1-dimensional center-of-gravity computed within a 1×5 image window centered at the locations of maximum image gradient, and
   (b) 2-dimensional center-of-gravity computed within a 5×5 image window centered at the locations of maximum image gradient

Note that the two different evaluation procedures result in two types of perturbation associated with the data points. The 1-dimensional center-of-gravity computation leads to perturbation along the horizontal image direction only, whereas the 2-dimensional computation of the center-of-gravity delivers perturbation of the data points along the horizontal as well as the vertical image direction.

[2]These comprise (a) the camera as well as the specimen to remain unmoved during the measurements, (b) constant parameters of the measurement setup, such as lighting intensity, lens aperture or exposure time, and (c) ideally constant environmental conditions, such as ambient light or vibrations.

4.2.4.1 Organisation of the Measurement Data

As a result of the two evaluation procedures, 2 sets of measurement points were obtained. For each set of measurement points, the x- and y-coordinates were organized in a common data matrix P of size $4n \times m$:

$$\mathsf{P} = \begin{bmatrix} {}_1x_{1,1} & {}_1x_{1,2} & \cdots & {}_1x_{1,m} \\ \vdots & \vdots & \ddots & \vdots \\ {}_1x_{n,1} & {}_1x_{n,2} & \cdots & {}_1x_{n,m} \\ {}_2x_{1,1} & {}_2x_{1,2} & \cdots & {}_2x_{1,m} \\ \vdots & \vdots & \ddots & \vdots \\ {}_2x_{n,1} & {}_2x_{n,2} & \cdots & {}_2x_{n,m} \\ {}_1y_{1,1} & {}_1y_{1,2} & \cdots & {}_1y_{1,m} \\ \vdots & \vdots & \ddots & \vdots \\ {}_1y_{n,1} & {}_1y_{n,2} & \cdots & {}_1y_{n,m} \\ {}_2y_{1,1} & {}_2y_{1,2} & \cdots & {}_2y_{1,m} \\ \vdots & \vdots & \ddots & \vdots \\ {}_2y_{n,1} & {}_2y_{n,2} & \cdots & {}_2y_{n,m} \end{bmatrix}. \tag{4.76}$$

A multivariate Gaussian distribution with mean vector $\boldsymbol{\mu_p}$ and covariance matrix $\Lambda_{\boldsymbol{p}}$ was assumed as the statistical model underlying the data points.
The mean vector, $\boldsymbol{\mu_p} = [\mu_{1x_1}, \ldots, \mu_{1x_n}, \mu_{2x_1}, \ldots, \mu_{2x_n}, \mu_{1y_1}, \ldots, \mu_{1y_n}, \mu_{2y_1}, \ldots, \mu_{2y_n}]^T$, was determined by evaluation of the particular rows of P, i.e.:

$$\begin{aligned} {}_1\mu_{x_i} &= \tfrac{1}{m}\sum_{k=1}^{m} {}_1x_{i,k}, \\ {}_1\mu_{y_i} &= \tfrac{1}{m}\sum_{k=1}^{m} {}_1y_{i,k}, \end{aligned} \tag{4.77}$$

$$\begin{aligned} {}_2\mu_{x_i} &= \tfrac{1}{m}\sum_{k=1}^{m} {}_2x_{i,k}, \\ {}_2\mu_{y_i} &= \tfrac{1}{m}\sum_{k=1}^{m} {}_2y_{i,k}. \end{aligned} \tag{4.78}$$

Moreover, the $4n \times 4n$ covariance matrix $\Lambda_{\boldsymbol{p}}$ was computed according to:

$$\Lambda_{\boldsymbol{p}} = \frac{1}{m-1}\left(\hat{\mathsf{P}}\ \hat{\mathsf{P}}^T\right), \tag{4.79}$$

with $\hat{\mathsf{P}}$ representing the matrix of mean free point coordinates, which in turn was computed as: $\hat{\mathsf{P}} = \mathsf{P} - \boldsymbol{\mu_p} \otimes \mathbf{1}$. Therein, $\mathbf{1}$ represents an m-dimensional row vector of 1's, and the symbol $\otimes$ indicates the Kronecker matrix product.

4.2.4.2 Evaluation of the Measurement Data

In order to evaluate the measurement data obtained by the two evaluation procedures, a pair of parallel lines was fitted to the particular sets of data points according to the procedure outlined in Section 4.2.1. Furthermore, the orthogonal distance between each pair of parallel lines was computed resulting in two sets of m orthogonal distances d_i, $i = 1 \ldots m$. Finally, the average distance μ_d as well as the associated variance σ_d^2 were determined.

4.2.4.3 Comparison with the Results of Analytic Computation

Based on the procedure outlined in Section 4.2.2, the uncertainty in the measurement data, represented by the covariance matrix $\Lambda_{\boldsymbol{p}}$, was analytically propagated to the uncertainty in the line parameters by application of the law of first order error propagation. Furthermore, the variance $\sigma_{d_A}^2$, associated with the orthogonal distance between the pair of parallel lines was analytically computed according to Equation (4.71).

In Table 4.2, the results obtained by evaluation of the measurement data as well as those from the analytic computations are presented for both of the two evaluation procedures described above.

center-of-gravity	$\mu_d, [pix]$	$\sigma_d^2, [pix^2]$	$\sigma_{d_A}^2, [pix^2]$	$\frac{\sigma_d^2 - \sigma_{d_A}^2}{\sigma_d^2}, [\%]$
1-dim.	137.02	$4.11\ 10^{-3}$	$4.06\ 10^{-3}$	1.21
2-dim.	137.17	$1.77\ 10^{-3}$	$1.71\ 10^{-3}$	3.64

Table 4.2: Comparison of the results of an uncertainty analysis concerning the orthogonal distance between a pair of parallel lines. The average orthogonal distance μ_d as well as the associated variance σ_d^2 were obtained by evaluation of the measurement data, whereas the variance $\sigma_{d_A}^2$ was analytically estimated.

As can be seen, the results of the measurement data evaluations and the analytic computations are in good agreement with one another. The small relative deviations can be explained by the approximation introduced for computing the first order error propagation of the line orientation parameters (cf. Section 2.3.3.1).

Moreover, the variance associated with the orthogonal distance between the two parallel lines is about 2 times smaller when extracting the locations of the data points by means of 2-dimensional center-of-gravity computation compared to the 1-dimensional center-of-gravity computation. This is a result of the additional averaging effect introduced by the 2-dimensional center-of-gravity computation, which can also be observed in the average variance $\bar{\sigma}_x^2$ of a data point along the horizontal image direction. For the data points of the left object edge, $\bar{\sigma}_x^2 = 5.3\ 10^{-3}$ in the case of 2-dimensional center-of-gravity computation compared to $\bar{\sigma}_x^2 = 8.4\ 10^{-2}$ in the case of 1-dimensional center-of-gravity computation.

Chapter 5

Geometric Transformations of the Projective Plane

In this chapter, the well-known "direct linear transformation" (DLT) algorithm for estimating plane-to-plane homographies is treated. Homographies represent the most general type of linear geometric transformations (see e.g. [32, 16]) and are frequently required for solving computer vision problems.

The DLT algorithm is probably the best-known approach for estimating homographies based on point correspondences. In the present work, a brief derivation of the DLT algorithm is given at first. As will be outlined, the procedure is based on computing a least squares solution of a set of linear equations.

Furthermore, an analytic approach for estimating the covariance matrix associated with a vector of homography parameters is presented. The procedure is based on the covariance matrices of the sets of corresponding points required for the homography computation and is accomplished by application of the law of first order error propagation. The Jacobian matrix required therein is to be derived from the implicitly defined least squares problem, which will be described in detail.

Finally, the results of the analytic computation are verified by means of numerical examples. These are realized on real measurement data extracted from images acquired at conditions of repeatability as well as on synthetically generated data points and Monte-Carlo simulations.

5.1 Estimation of Plane-to-Plane Homographies

Considering the 2-dimensional situation, precisely the projective plane, points are represented by homogeneous 3-vectors and are transformed under a homography according to:

$$\boldsymbol{p}' = \begin{bmatrix} x' \\ y' \\ w' \end{bmatrix} = \begin{bmatrix} h_{11} & h_{12} & h_{13} \\ h_{21} & h_{22} & h_{23} \\ h_{31} & h_{32} & h_{33} \end{bmatrix} \begin{bmatrix} x \\ y \\ w \end{bmatrix} = \mathsf{H}\boldsymbol{p}. \tag{5.1}$$

The 3×3 homography matrix H is homogeneous and regular, i.e. it has 8 degrees of freedom. As a result, a number of $n \geq 4$ point correspondences (each contributing with two equations) is required to determine H. The "direct linear transformation" (DLT) algorithm is probably the best-known procedure for the direct (i.e. non-iterative) estimation of a homography, see e.g. [32, 11, 12].

5.1.1 The Direct Linear Transformation Algorithm

Given $n \geq 4$ pairs of corresponding points, $\boldsymbol{p}_i$ and $\boldsymbol{p}'_i$, $i = \{1 \dots n\}$. Expanding Equation (5.1) yields two equations for each pair of corresponding points:

$$\frac{x'_i}{w'_i} = \frac{h_{11}x_i + h_{12}y_i + h_{13}w_i}{h_{31}x_i + h_{32}y_i + h_{33}w_i}, \tag{5.2}$$

$$\frac{y'_i}{w'_i} = \frac{h_{21}x_i + h_{22}y_i + h_{23}w_i}{h_{31}x_i + h_{32}y_i + h_{33}w_i}, \tag{5.3}$$

which are rearranged to:

$$\left(-h_{11}x_i - h_{12}y_i - h_{13}w_i\right) w'_i + \left(h_{31}x_i + h_{32}y_i + h_{33}w_i\right) x'_i = 0, \tag{5.4}$$

$$\left(-h_{21}x_i - h_{22}y_i - h_{23}w_i\right) w'_i + \left(h_{31}x_i + h_{32}y_i + h_{33}w_i\right) y'_i = 0. \tag{5.5}$$

Collecting the equations of the n pairs of corresponding points leads to the matrix equation:

$$\mathsf{D}\boldsymbol{h} = \mathbf{0}, \tag{5.6}$$

with the vector of homography parameters:

$$\boldsymbol{h} = \begin{bmatrix} h_{11} & h_{12} & h_{13} & h_{21} & h_{22} & h_{23} & h_{31} & h_{32} & h_{33} \end{bmatrix}^T, \tag{5.7}$$

and the design matrix:

$$\mathsf{D} = \begin{bmatrix} -x_1w'_1 & -y_1w'_1 & -w_1w'_1 & 0 & 0 & 0 & x_1x'_1 & y_1x'_1 & w_1x'_1 \\ 0 & 0 & 0 & -x_1w'_1 & -y_1w'_1 & -w_1w'_1 & x_1y'_1 & y_1y'_1 & w_1y'_1 \\ \vdots & \vdots & \vdots & \vdots & \vdots & \vdots & \vdots & \vdots & \vdots \\ -x_nw'_n & -y_nw'_n & -w_nw'_n & 0 & 0 & 0 & x_nx'_n & y_nx'_n & w_nx'_n \\ 0 & 0 & 0 & -x_nw'_n & -y_nw'_n & -w_nw'_n & x_ny'_n & y_ny'_n & w_ny'_n \end{bmatrix}. \tag{5.8}$$

In order to find a non-trivial solution for this system of linear equations, singular value decomposition (SVD) is applied on the design matrix D and the vector of homography parameters $\boldsymbol{h}$ is found as the right singular vector corresponding to the smallest singular value of D.

Summarizing, estimation of a homography according to the DLT algorithm is realized by solving the linear least squares problem:

$$\min_{\boldsymbol{h}} \|\mathsf{D}\boldsymbol{h}\| \quad \text{subject to:} \quad \|\boldsymbol{h}\| = 1. \tag{5.9}$$

The disadvantage of the DLT algorithm is that it does not take into account the varying statistical nature of the particular columns of D. Assuming the points involved in the homography computation being "measured" quantities, the homogeneous coordinates w_i and w_i' are equal to 1. Thus, they are statistically invariant as are the zero entries of D. On the other hand, there are elements showing the perturbation of an individual point coordinate as well as elements exhibiting the perturbation of the product of two point coordinates. As a result of the statistical inhomogeneities inherent to D, the solution obtained with the DLT algorithm is subject to systematic errors.

A different approach for the direct estimation of homographies has been presented by Harker and O'Leary [28]. The approach utilized therein is based on partitioned orthogonalization of the sparse design matrix D in order to overcome the stated drawback of the DLT algorithm. In this thesis however, homographies are estimated by means of the DLT algorithm for simplicity reasons. In the following sections, a derivation for the first order error propagation associated with the DLT algorithm is presented.

5.1.2 First Order Error Propagation for the DLT Algorithm

5.1.2.1 Organisation of the Data Points

The points involved in the homography computation are assumed to be "measured", i.e. the homogeneous coordinates w_i and w_i' are equal to 1. The remaining coordinates of the pairs of corresponding points are collected in a common vector $\boldsymbol{q}$ according to the following order:

$$\boldsymbol{q} = [x_1, \ldots, x_n, y_1, \ldots, y_n, x_1', \ldots, x_n', y_1', \ldots, y_n']^T. \tag{5.10}$$

In the following, the point coordinates are to be understood as expectation values of a Gaussian probability density function. The covariance matrix $\Lambda_{\boldsymbol{q}}$ associated with the data points is structured as follows:

$$\Lambda_{\boldsymbol{q}} = \begin{bmatrix} \Lambda_{\boldsymbol{p}} & 0 \\ 0 & \Lambda_{\boldsymbol{p}'} \end{bmatrix}, \quad \text{with:} \quad \Lambda_{\boldsymbol{p}} = \begin{bmatrix} \Lambda_{\boldsymbol{x}} & \mathsf{C}_{\boldsymbol{xy}} \\ \mathsf{C}_{\boldsymbol{xy}}^T & \Lambda_{\boldsymbol{y}} \end{bmatrix}, \; \Lambda_{\boldsymbol{p}'} = \begin{bmatrix} \Lambda_{\boldsymbol{x}'} & \mathsf{C}_{\boldsymbol{xy}'} \\ \mathsf{C}_{\boldsymbol{xy}'}^T & \Lambda_{\boldsymbol{y}'} \end{bmatrix}. \tag{5.11}$$

Therein, $\Lambda_{\boldsymbol{x}}$ and $\Lambda_{\boldsymbol{y}}$ as well as $\Lambda_{\boldsymbol{x}'}$ and $\Lambda_{\boldsymbol{y}'}$ denote the covariance matrices associated with the x- and y-coordinates of the two sets of data points. Furthermore, $\mathsf{C}_{\boldsymbol{xy}}$ and $\mathsf{C}_{\boldsymbol{xy}'}$ specify matrices of covariances between the respective x- and y-coordinates. Finally, it is assumed that there are no covariances existing between the two sets of points.

5.1.2.2 Estimation of the Homography

As described in Section 5.1.1, a homography is estimated according to the DLT algorithm by solving the system of linear equations:

$$\boldsymbol{\Phi}\left(\boldsymbol{q},\boldsymbol{h}\right)=\mathsf{D}\boldsymbol{h}=\mathbf{0}. \tag{5.12}$$

Applying the law of first order error propagation, the 9×9 covariance matrix associated with the vector of homography parameters $\boldsymbol{h}$ is estimated as:

$$\Lambda_{\boldsymbol{h}}\approx \mathsf{J}_{\boldsymbol{h}}\Lambda_{\boldsymbol{q}}{\mathsf{J}_{\boldsymbol{h}}}^{T}. \tag{5.13}$$

Therein, $\Lambda_{\boldsymbol{q}}$, represents the covariance matrix associated with the data points involved in the homography computation as defined in Equation (5.11). Referring to Section 2.3.3.2, the Jacobian matrix $\mathsf{J}_{\boldsymbol{h}}$ is approximated as:

$$\mathsf{J}_{\boldsymbol{h}}\approx -\mathsf{A}^{+}\frac{\partial\boldsymbol{\Phi}}{\partial A}\frac{\partial A}{\partial\boldsymbol{q}}. \tag{5.14}$$

Therein, the 9×9 matrix A is calculated as:

$$\mathsf{A}=\mathsf{D}^{T}\mathsf{D}, \tag{5.15}$$

and thus, the 9×81 matrix $\frac{\partial\Phi}{\partial A}$ results to:

$$\frac{\partial\Phi}{\partial A}=\begin{bmatrix}\boldsymbol{h}^{T} & \mathbf{0} & \dots & \mathbf{0}\\ \mathbf{0} & \boldsymbol{h}^{T} & \dots & \mathbf{0}\\ \vdots & \vdots & \ddots & \vdots\\ \mathbf{0} & \mathbf{0} & \dots & \boldsymbol{h}^{T}\end{bmatrix}. \tag{5.16}$$

In order to compute the $81\times 4n$ matrix $\frac{\partial A}{\partial\boldsymbol{q}}$, we take a closer look at matrix A at first:

$$\mathsf{A}=\mathsf{D}^{T}\mathsf{D}=\begin{bmatrix}\mathsf{A}_1 & \mathsf{0} & -\mathsf{A}_2\\ \mathsf{0} & \mathsf{A}_1 & -\mathsf{A}_3\\ -\mathsf{A}_2 & -\mathsf{A}_3 & \mathsf{A}_4\end{bmatrix}. \tag{5.17}$$

Therein, the four symmetric 3×3 sub-matrices A_1 to A_4 appear as follows:

$$\mathsf{A}_1=\begin{bmatrix}\sum_{i=1}^{n}x_i^2 & \sum_{i=1}^{n}x_iy_i & \sum_{i=1}^{n}x_i\\ \sum_{i=1}^{n}x_iy_i & \sum_{i=1}^{n}y_i^2 & \sum_{i=1}^{n}y_i\\ \sum_{i=1}^{n}x_i & \sum_{i=1}^{n}y_i & n\end{bmatrix},\qquad \mathsf{A}_2=\begin{bmatrix}\sum_{i=1}^{n}x_i^2x_i' & \sum_{i=1}^{n}x_iy_ix_i' & \sum_{i=1}^{n}x_ix_i'\\ \sum_{i=1}^{n}x_iy_ix_i' & \sum_{i=1}^{n}y_i^2x_i' & \sum_{i=1}^{n}y_ix_i'\\ \sum_{i=1}^{n}x_ix_i' & \sum_{i=1}^{n}y_ix_i' & \sum_{i=1}^{n}x_i'\end{bmatrix}, \tag{5.18}$$

$$\mathsf{A}_3 = \begin{bmatrix} \sum_{i=1}^{n} x_i^2 y_i' & \sum_{i=1}^{n} x_i y_i y_i' & \sum_{i=1}^{n} x_i y_i' \\ \sum_{i=1}^{n} x_i y_i y_i' & \sum_{i=1}^{n} y_i^2 y_i' & \sum_{i=1}^{n} y_i y_i' \\ \sum_{i=1}^{n} x_i y_i' & \sum_{i=1}^{n} y_i y_i' & \sum_{i=1}^{n} y_i' \end{bmatrix}, \quad \mathsf{A}_4 = \begin{bmatrix} \sum_{i=1}^{n} x_i^2 s_i' & \sum_{i=1}^{n} x_i y_i s_i' & \sum_{i=1}^{n} x_i s_i' \\ \sum_{i=1}^{n} x_i y_i s_i' & \sum_{i=1}^{n} y_i^2 s_i' & \sum_{i=1}^{n} y_i s_i' \\ \sum_{i=1}^{n} x_i s_i' & \sum_{i=1}^{n} y_i s_i' & \sum_{i=1}^{n} s_i' \end{bmatrix}, \tag{5.19}$$

with the substitution: $s_i' = x_i'^2 + y_i'^2$, $i = 1 \ldots n$.

The elements of $\frac{\partial A}{\partial \boldsymbol{q}}$ are obtained by taking the partial derivatives of the elements in the four sub-matrices A_1 to A_4 with respect to the particular elements of $\boldsymbol{q}$. Due to the sparse, symmetric nature of the matrix A, the number of distinct elements, whose partial derivatives are to be computed, reduces to 24 (six for each of the sub-matrices A_1 to A_4).

The particular results are listed in Table 5.1 to Table 5.4.

$a_{1_{ij}}$	$\frac{\partial a_{1_{ij}}}{\partial x_i}$	$\frac{\partial a_{1_{ij}}}{\partial y_i}$	$\frac{\partial a_{1_{ij}}}{\partial x_i'}$	$\frac{\partial a_{1_{ij}}}{\partial y_i'}$
$\sum_{i=1}^{n} x_i^2$	$2x_i$	0	0	0
$\sum_{i=1}^{n} x_i y_i$	y_i	x_i	0	0
$\sum_{i=1}^{n} y_i^2$	0	$2y_i$	0	0
$\sum_{i=1}^{n} x_i$	1	0	0	0
$\sum_{i=1}^{n} y_i$	0	1	0	0
n	0	0	0	0

Table 5.1: Partial derivatives of the distinct elements $a_{1_{ij}}$ of sub-matrix A_1.

$a_{2_{ij}}$	$\frac{\partial a_{2_{ij}}}{\partial x_i}$	$\frac{\partial a_{2_{ij}}}{\partial y_i}$	$\frac{\partial a_{2_{ij}}}{\partial x_i'}$	$\frac{\partial a_{2_{ij}}}{\partial y_i'}$
$\sum_{i=1}^{n} x_i^2 x_i'$	$2x_i x_i'$	0	x_i^2	0
$\sum_{i=1}^{n} x_i y_i x_i'$	$y_i x_i'$	$x_i x_i'$	$x_i y_i$	0
$\sum_{i=1}^{n} y_i^2 x_i'$	0	$2y_i x_i'$	y_i^2	0
$\sum_{i=1}^{n} x_i x_i'$	x_i'	0	x_i	0
$\sum_{i=1}^{n} y_i x_i'$	0	x_i'	y_i	0
$\sum_{i=1}^{n} x_i'$	0	0	1	0

Table 5.2: Partial derivatives of the distinct elements $a_{2_{ij}}$ of sub-matrix A_2.

$a_{3_{ij}}$	$\frac{\partial a_{3_{ij}}}{\partial x_i}$	$\frac{\partial a_{3_{ij}}}{\partial y_i}$	$\frac{\partial a_{3_{ij}}}{\partial x'_i}$	$\frac{\partial a_{3_{ij}}}{\partial y'_i}$
$\sum_{i=1}^{n} x_i^2 y'_i$	$2x_i y'_i$	0	0	x_i^2
$\sum_{i=1}^{n} x_i y_i y'_i$	$y_i y'_i$	$x_i y'_i$	0	$x_i y_i$
$\sum_{i=1}^{n} y_i^2 y'_i$	0	$2y_i y'_i$	0	y_i^2
$\sum_{i=1}^{n} x_i y'_i$	y'_i	0	0	x_i
$\sum_{i=1}^{n} y_i y'_i$	0	y'_i	0	y_i
$\sum_{i=1}^{n} y'_i$	0	0	0	1

Table 5.3: Partial derivatives of the distinct elements $a_{3_{ij}}$ of sub-matrix A_3.

$a_{4_{ij}}$	$\frac{\partial a_{4_{ij}}}{\partial x_i}$	$\frac{\partial a_{4_{ij}}}{\partial y_i}$	$\frac{\partial a_{4_{ij}}}{\partial x'_i}$	$\frac{\partial a_{4_{ij}}}{\partial y'_i}$
$\sum_{i=1}^{n} x_i^2 s'_i$	$2x_i s'_i$	0	$2x_i^2 x'_i$	$2x_i^2 y'_i$
$\sum_{i=1}^{n} x_i y_i s'_i$	$y_i s'_i$	$x_i s'_i$	$2x_i y_i x'_i$	$2x_i y_i y'_i$
$\sum_{i=1}^{n} y_i^2 s'_i$	0	$2y_i s'_i$	$2y_i^2 x'_i$	$2y_i^2 y'_i$
$\sum_{i=1}^{n} x_i s'_i$	s'_i	0	$2x_i x'_i$	$2x_i y'_i$
$\sum_{i=1}^{n} y_i s'_i$	0	s'_i	$2y_i x'_i$	$2y_i y'_i$
$\sum_{i=1}^{n} s'_i$	0	0	$2x'_i$	$2y'_i$

Table 5.4: Partial derivatives of the distinct elements $a_{4_{ij}}$ of sub-matrix A_4.

After properly collecting the partial derivatives for all of the n data points into the $81 \times 4n$ matrix $\frac{\partial \mathsf{A}}{\partial \boldsymbol{q}}$, the Jacobian matrix $\mathsf{J}_{\boldsymbol{h}}$ can be calculated according to Equation (5.14).

Finally, the 9×9 covariance matrix $\Lambda_{\boldsymbol{h}}$ associated with the vector of homography parameters is estimated according to Equation (5.13).

5.1.3 First Order Error Propagation for a Point Transformation

Given a point $\boldsymbol{p} = [x, y, w]^T$ together with its associated covariance matrix $\Lambda_{\boldsymbol{p}}$, as well as a homography matrix H together with the 9×9 covariance matrix $\Lambda_{\boldsymbol{h}}$ associated with the vector of homography parameters $\boldsymbol{h}$. In order to estimate the covariance matrix associated with the point transformed under the given homography, $\boldsymbol{p}' = \mathsf{H}\boldsymbol{p}$ (cf. Equation (5.1)), the law of first order error propagation is applied:

$$\Lambda_{\boldsymbol{p}'} = \mathsf{J}_{\boldsymbol{p}'} \Lambda_{\boldsymbol{h},\boldsymbol{p}} \mathsf{J}_{\boldsymbol{p}'}^T. \tag{5.20}$$

Therein, a combined 12×12 covariance matrix $\Lambda_{\boldsymbol{h},\boldsymbol{p}}$ is incorporated, which is structured as follows:

$$\Lambda_{\boldsymbol{h},\boldsymbol{p}} = \begin{bmatrix} \Lambda_{\boldsymbol{h}} & \mathsf{0} \\ \mathsf{0} & \Lambda_{\boldsymbol{p}} \end{bmatrix}. \tag{5.21}$$

It is assumed that there are no covariances existing between the homography parameters and the point to be transformed. Moreover, the required 3×12 Jacobian matrix $\mathsf{J}_{\boldsymbol{p}'}$ results to:

$$\mathsf{J}_{\boldsymbol{p}'} = \begin{bmatrix} \mathsf{P} & \mathsf{H} \end{bmatrix}, \quad \text{with: } \mathsf{P} = \begin{bmatrix} \boldsymbol{p}^T & \mathbf{0} & \mathbf{0} \\ \mathbf{0} & \boldsymbol{p}^T & \mathbf{0} \\ \mathbf{0} & \mathbf{0} & \boldsymbol{p}^T \end{bmatrix}. \tag{5.22}$$

5.1.4 Numerical Verification

A series of m images of a calibration target utilized for a video-extensometer system, which will be presented in Chapter 7, was acquired with an industrial camera at conditions of repeatability[1]. See Figure 5.1 for a sample of the image series.

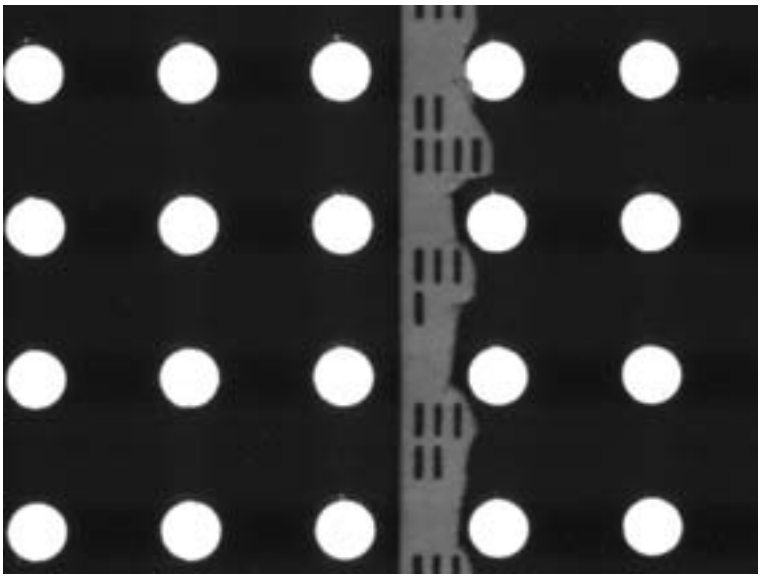

Figure 5.1: A sample image of a calibration target acquired with an industrial camera. The target exhibits a rectangular grid of reference bores with diameters of 1.5mm. The distance between center points of adjacent reference bores is 4mm in each direction.

The calibration target is equipped with a rectangular grid of reference bores (bright circular image objects) as well as a simple bar-coding scheme utilized to properly identify the particular reference bores in the acquired images.

5.1.4.1 The Image Coordinates of the Center Points

Each of the particular series images was evaluated independently to determine the center point coordinates of the reference bores. For that purpose, a contour extraction algorithm was applied to the particular series images. In order to separate "invalid" contour objects from those representing the circumference of the reference bores, the following processing steps were executed:

1. Verifying the horizontal, the vertical as well as the average dimension, contour objects showing an inappropriate size were eliminated.

2. Contour objects with a shape significantly deviating from a circular shape were rejected by checking the aspect ratio of the contour objects.

[1]These comprise (a) the camera as well as the specimen to remain unmoved during the measurements, (b) constant parameters of the measurement setup, such as lighting intensity, lens aperture or exposure time, and (c) ideally constant environmental conditions, such as ambient light or vibrations.

3. A circular model was approximated to each of the remaining contour objects and by verifying the fitting residual, the contour objects representing the imaged reference bores can finally be separated.

The algorithm utilized for approximating circular models to the sets of contour points comprises two steps. At first, a simple algebraic fit is applied according to the algorithm outlined by O'Leary [44] to the points of the particular contour objects. Subsequently, the circle parameters obtained are taken as initial values for an iterative optimization method presented by Joseph [34].

Finally, the center point coordinates of the "valid" circular contour objects were sorted according to their location with respect to the image coordinate frame, starting from the upper left corner going row-wise down the grid to the lower right corner.

5.1.4.2 Organisation of the Image Point Coordinates

As a result, m sets of the $n = 20$ center points were obtained with respect to the image coordinate frame. The x- and y-coordinates of the points were organized in a common $2n \times m$ data matrix P:

$$\mathsf{P} = \begin{bmatrix} x_{1,1} & x_{1,2} & \dots & x_{1,m} \\ x_{2,1} & x_{2,2} & \dots & x_{2,m} \\ \vdots & \vdots & \ddots & \vdots \\ x_{n,1} & x_{n,2} & \dots & x_{n,m} \\ y_{1,1} & y_{1,2} & \dots & y_{1,m} \\ y_{2,1} & y_{2,2} & \dots & y_{2,m} \\ \vdots & \vdots & \ddots & \vdots \\ y_{n,1} & y_{n,2} & \dots & y_{n,m} \end{bmatrix}. \tag{5.23}$$

In the following, a multivariate Gaussian distribution with mean vector $\boldsymbol{\mu}_{\boldsymbol{p}}$ and covariance matrix $\Lambda_{\boldsymbol{p}}$ is assumed as the statistical model underlying the data points. Given P, the vector of mean values is computed as specified by Equation (4.39). Moreover, the $2n \times 2n$ covariance matrix $\Lambda_{\boldsymbol{p}}$ is determined according to Equation (4.40).

Note that as a consequence of the evaluation procedure, the location of the particular center points is subject to measurement noise along the x- as well as the y-coordinate. Thus, the covariance matrix $\Lambda_{\boldsymbol{p}}$ is fully occupied.

5.1.4.3 The Metric Coordinates of the Center Points

The reference bore's center point coordinates were determined with respect to a metric coordinate frame (see Chapter 7 for details) prior to the analysis and stored in a file on the hard-disk. In order to find the set of metric center point coordinates corresponding to the set of center points extracted in the images, the bar-coding scheme (cf. Figure 5.1) was evaluated:

- the bar-code itself holds the information about the row indices (with respect to the rectangular grid) of the imaged reference bores, and

- the horizontal position of the stripe of paper holding the bar-code specifies the column indices of the imaged reference bores.

Given the row and column indices of the imaged reference bores, the metric center point coordinates, $[x'_i, y'_i]$, $i = 1 \dots n$, corresponding to the points extracted in the images were identified. As a result, a proper assignment of the center points in the image and the metric coordinate frame was achieved.

5.1.4.4 Organisation of the Metric Point Coordinates

The uncertainty associated with the metric center point coordinates is directly related to the positioning accuracy of the device utilized for measuring the surface of the calibration target (cf. Chapter 7). In the present situation, the uncertainty of the metric center point coordinates, $[x'_i, y'_i]$, $i = 1 \dots n$, is given in terms of the standard deviation values $\sigma_{x'} = \sigma_{y'} \approx 0.2\mu m$. The covariance between the center point coordinates is assumed to be negligible small, i.e. $\sigma_{xy'} \approx 0$. As a result, the covariance matrix $\Lambda_{\boldsymbol{p}'}$ associated with the vector of metric center point coordinates,

$$\boldsymbol{\mu}_{\boldsymbol{p}'} = \left[\; x'_1, x'_2, \dots, x'_n, y'_1, y'_2, \dots, y'_n \; \right]^T, \tag{5.24}$$

is a diagonal matrix of the form:

$$\Lambda_{\boldsymbol{p}'} = \begin{bmatrix} \Lambda_{\boldsymbol{x}'} & 0 \\ 0 & \Lambda_{\boldsymbol{y}'} \end{bmatrix}, \; \Lambda_{\boldsymbol{x}'} = \begin{bmatrix} \sigma^2_{x'} & 0 & \dots & 0 \\ 0 & \sigma^2_{x'} & \dots & 0 \\ \vdots & \vdots & \ddots & \vdots \\ 0 & 0 & \dots & \sigma^2_{x'} \end{bmatrix}, \; \Lambda_{\boldsymbol{y}'} = \begin{bmatrix} \sigma^2_{y'} & 0 & \dots & 0 \\ 0 & \sigma^2_{y'} & \dots & 0 \\ \vdots & \vdots & \ddots & \vdots \\ 0 & 0 & \dots & \sigma^2_{y'} \end{bmatrix}. \tag{5.25}$$

5.1.4.5 Monte-Carlo Simulation

Given the coordinate vectors of the sets of $n = 20$ corresponding pairs of center points, $\boldsymbol{\mu}_{\boldsymbol{p}}$ and $\boldsymbol{\mu}_{\boldsymbol{p}'}$, together with their associated covariance matrices, $\Lambda_{\boldsymbol{p}}$ and $\Lambda_{\boldsymbol{p}'}$. A Monte-Carlo simulation was now started by generating a number of $m = 10^5$ synthetical sets of corresponding pairs of points (cf. Section 2.3.2). Subsequently, the DLT algorithm was executed on the particular sets of corresponding points and a number of m vectors of homography parameters $\boldsymbol{h}_i$, $i = 1 \dots m$, was obtained. Moreover, the vector of mean homography parameters $\boldsymbol{\mu}_{\boldsymbol{h}_{MC}}$ is computed,

$$\boldsymbol{\mu}_{\boldsymbol{h}_{MC}} = \frac{1}{m} \sum_{i=1}^{m} \boldsymbol{h}_i, \tag{5.26}$$

as well as the 9×9 covariance matrix $\Lambda_{\boldsymbol{h}_{MC}}$ associated with the homography parameters:

$$\Lambda_{\boldsymbol{h}_{MC}} = \frac{1}{m-1} \sum_{i=1}^{m} \left(\left(\boldsymbol{h}_i - \boldsymbol{\mu}_{\boldsymbol{h}} \right) \left(\boldsymbol{h}_i - \boldsymbol{\mu}_{\boldsymbol{h}} \right)^T \right). \tag{5.27}$$

5.1.4.6 Comparison with the Results of Analytic Computation

Starting again with the vectors $\boldsymbol{\mu}_{\boldsymbol{p}}$ and $\boldsymbol{\mu}_{\boldsymbol{p}'}$ as well as the associated covariance matrices $\Lambda_{\boldsymbol{p}}$ and $\Lambda_{\boldsymbol{p}'}$, the error propagation through the DLT algorithm was estimated according to the procedure presented in Section 5.1.2. As a result of this computation, the first order estimate of $\Lambda_{\boldsymbol{h}_A}$ of the covariance matrix associated with the vector of homography parameters was obtained. The results of the Monte-Carlo simulation were compared with the results of the analytic computation by means of the relative Frobenius norm error:

$$\frac{\parallel \Lambda_{\boldsymbol{h}_A} - \Lambda_{\boldsymbol{h}_{MC}} \parallel}{\parallel \Lambda_{\boldsymbol{h}_A} \parallel} \approx 0.79\%. \tag{5.28}$$

The small deviations are explained by the approximations inherent to the first order order estimate of error propagation of the DLT algorithm.

5.1.4.7 The Influence of the Pairs of Points Utilized for the DLT Algorithm

In the preceding analysis, the center points of the reference bores were chosen as the sets of corresponding pairs of points required for the DLT algorithm. The procedure was repeated with a second set of corresponding pairs of points. At first, two sets of parallel and orthogonal lines were fitted to the center points according to their location with respect to the grid of reference bores (see Figure 5.2). The algorithm utilized for this fitting operation represents an extension of the procedure of fitting a pair of parallel lines, as described in Section 4.2.1.

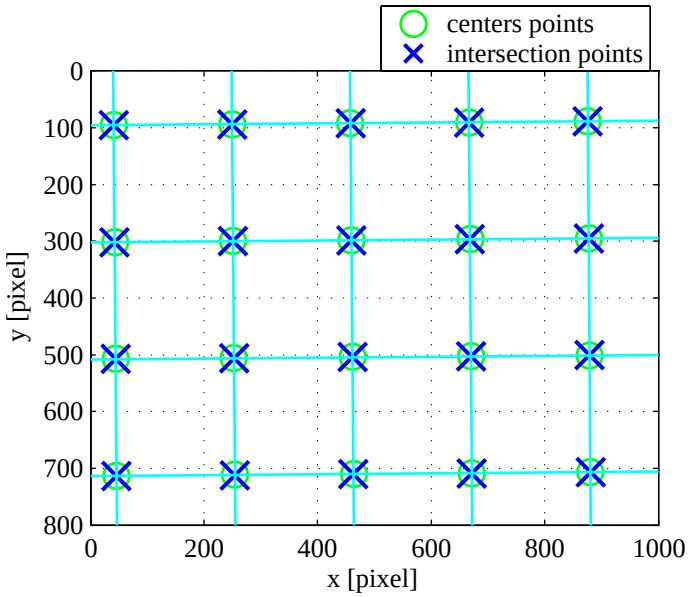

Figure 5.2: The center points of the reference bores together with the approximated sets of parallel and orthogonal lines as well as the resulting intersection points.

Subsequently, the intersection points of the particular lines were calculated. This procedure was realized for the image points as well as for the metric points. As a result, a

number of $n = 20$ pairs of corresponding intersection points were obtained. See Figure 5.2 for an illustration of the lines fitted to the center points as well as the location of the intersection points with respect to the image coordinate frame.

As a result of the averaging effect introduced by the fitting operation, the uncertainty associated with the intersection points is significantly lower than the uncertainty associated with the given center points. This is illustrated in Figure 5.3, where the 99% confidence ellipses of the center points as well as those of the intersection points are depicted.

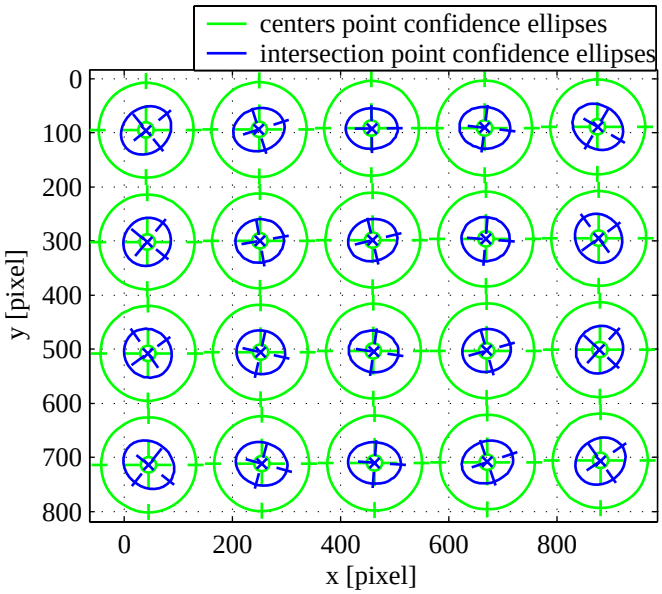

Figure 5.3: Comparison of the uncertainty associated with the given center points and the calculated intersection points. Note that the confidence ellipses were plotted incorporating a scaling factor of $f = 1000$.

Based on the sets of corresponding intersection points, a first order estimate of the covariance matrix associated with the homography parameters, $\Lambda_{\boldsymbol{h}_{A2}}$, was computed. In order to compare $\Lambda_{\boldsymbol{h}_{A2}}$ with $\Lambda_{\boldsymbol{h}_A}$, the quotient of Frobenius matrix norms $\frac{\|\Lambda_{\boldsymbol{h}_{A2}}\|}{\|\Lambda_{\boldsymbol{h}_A}\|} \approx 1.93$ was computed. Thus, computing the homography based on the sets of corresponding pairs of intersection points yields a significant reduction of the norm of the covariance matrix associated with the vector of homography parameters.

Chapter 6

First Order Error Propagation for Non-Linear Functions

This chapter deals with the application of the law of first order error propagation to non-linear functions. Considering an explicit, vector valued function $\boldsymbol{y} = \boldsymbol{f}(\boldsymbol{x})$, with $\boldsymbol{x}$ and $\boldsymbol{y}$ denoting vectors of uncertain input and output data, respectively. According to the law of first order error propagation (cf. Section 2.3.3):

$$\Lambda_{\boldsymbol{y}} = \mathsf{J}_{\boldsymbol{f}} \Lambda_{\boldsymbol{x}} \mathsf{J}_{\boldsymbol{f}}{}^{T}, \tag{6.1}$$

the uncertainty associated with the output variables, represented by the covariance matrix $\Lambda_{\boldsymbol{y}}$, is computed by means of the covariance matrix $\Lambda_{\boldsymbol{x}}$ and the Jacobian matrix $\mathsf{J}_{\boldsymbol{f}}$, which specifies the sensitivity of the elements in $\boldsymbol{y}$ with respect to the particular parameters in $\boldsymbol{x}$. For $\boldsymbol{f}$ representing a function linear in the parameters $\boldsymbol{x}$, Equation (6.1) is exact. However, when applied to functions non-linear in $\boldsymbol{x}$, the results of first order error propagation merely represent estimates of the covariance matrix $\Lambda_{\boldsymbol{y}}$.

In order to determine the approximation error associated with the estimate of $\Lambda_{\boldsymbol{y}}$, Monte-Carlo experiments can be performed. This method requires a large number of real measurement data, or - based on a suitable statistical model of the input variables - synthetically generated data. Moreover, Monte-Carlo experiments are computationally expensive.

In the following, a procedure for analytically computing the approximation error associated with first order estimates of error propagation for non-linear functions $\boldsymbol{f}(\boldsymbol{x})$ is presented. Due to the stochastic nature of the input data $\boldsymbol{x}$, the approximation error has to be understood as a confidence interval rather than a strict upper error bound.

The procedure is based on the definition of Lagrange remainder terms associated with Taylor series truncated after the first order terms. At first, the procedure is described in general. Subsequently, its applicability is demonstrated with a number of non-linear functions typically arising in metric vision tasks.

6.1 The Approximation Error in Results of First Order Error Propagation

When applied to non-linear, vector-valued functions $\boldsymbol{y} = \boldsymbol{f}(\boldsymbol{x})$, first order error propagation delivers an estimate of the covariance matrix $\Lambda_{\boldsymbol{y}}$ rather than the covariance matrix itself. A confidence interval associated with such an estimate can be analytically computed by the following procedure:

1. a Taylor series of the function is expanded around the means of the uncertain input data vector $\boldsymbol{x}$ up to the first order terms,
2. the Lagrange remainder term belonging to the Taylor series is computed,
3. the variance associated with the Lagrange remainder term is determined by application of the analytical definition of expectation values, and
4. the confidence interval is calculated as the maximum value of this variance.

To simplify matters, details of the procedure are outlined in the following on the basis of multivariate, scalar-valued functions.

6.1.1 Nature and Statistical Model of the Uncertain Input Data

In the following, the vector of uncertain input data $\boldsymbol{x} = [x_1, x_2, \ldots, x_p]^T$ is to be understood as a p-dimensional random vector, i.e. a vector of random variables x_i. Given a number of n realizations of the random vector - either obtained from repeated measurements or synthetically produced by means of a random number generator - the data can be organized in a $p \times n$ data matrix X as follows:

$$\mathsf{X} = \begin{bmatrix} x_{1,1} & x_{1,2} & \ldots & x_{1,n} \\ x_{2,1} & x_{2,2} & \ldots & x_{2,n} \\ \vdots & \vdots & \ddots & \vdots \\ x_{p,1} & x_{p,2} & \ldots & x_{p,n} \end{bmatrix}. \tag{6.2}$$

The random vector of uncertain input data $\boldsymbol{x}$ is assumed to have a multivariate Gaussian probability density function with expectation vector $\boldsymbol{\mu}_{\boldsymbol{x}}$ and covariance matrix $\Lambda_{\boldsymbol{x}}$, thus:

$$\boldsymbol{x} \sim \mathcal{N}\left(\boldsymbol{x}, \boldsymbol{\mu}_{\boldsymbol{x}}, \Lambda_{\boldsymbol{x}}\right) = \left((2\pi)^p \left|\Lambda_{\boldsymbol{x}}\right|\right)^{-\frac{1}{2}} \mathrm{e}^{-\frac{1}{2}(\boldsymbol{x}-\boldsymbol{\mu}_{\boldsymbol{x}})^T \Lambda_{\boldsymbol{x}}^{-1} (\boldsymbol{x}-\boldsymbol{\mu}_{\boldsymbol{x}})}. \tag{6.3}$$

The elements of the expectation vector $\boldsymbol{\mu}_{\boldsymbol{x}} = \left[\mu_{x_1}, \mu_{x_2}, \ldots, \mu_{x_p}\right]^T$ are calculated as:

$$\mu_{x_i} = \frac{1}{n} \sum_{k=1}^{n} x_{i,k}. \tag{6.4}$$

Moreover, the covariance matrix $\Lambda_{\boldsymbol{x}}$ is computed as:

$$\Lambda_{\boldsymbol{x}} = \frac{1}{n-1} \left(\hat{\mathsf{X}}\, \hat{\mathsf{X}}^T\right), \tag{6.5}$$

with $\hat{\mathsf{X}}$ terming the matrix of mean free data, which is obtained as: $\hat{\mathsf{X}} = \mathsf{X} - \boldsymbol{\mu}_{\boldsymbol{x}} \otimes \mathbf{1}$. Therein, $\mathbf{1}$ represents an n-dimensional row vector of 1's, and the symbol $\otimes$ indicates the Kronecker matrix product.

In order to simplify the probability density function presented in Equation (6.3) for subsequent computations, the vector of uncertain input data $\boldsymbol{x}$ is made mean-free. With this, a vector of mean-free perturbation values $\boldsymbol{e}_{\boldsymbol{x}} = \left[e_{x_1}, e_{x_2}, \ldots, e_{x_p}\right]^T$ is introduced:

$$\boldsymbol{e}_{\boldsymbol{x}} = \boldsymbol{x} - \boldsymbol{\mu}_{\boldsymbol{x}}. \tag{6.6}$$

Assuming that the mean values μ_{x_i} have been computed from a sufficiently large number of samples, their uncertainty can be neglected. Thus, merely the values e_{x_i} are subject to perturbation and the Gaussian probability density function underlying the uncertain input data simplifies to:

$$\boldsymbol{x} \sim \mathcal{N}\left(\boldsymbol{x}, \boldsymbol{\mu}_{\boldsymbol{x}}, \Lambda_{\boldsymbol{x}}\right) = \left((2\pi)^p \left|\Lambda_{\boldsymbol{x}}\right|\right)^{-\frac{1}{2}} \mathrm{e}^{-\frac{1}{2}\boldsymbol{e}_{\boldsymbol{x}}^T \Lambda_{\boldsymbol{x}}^{-1} \boldsymbol{e}_{\boldsymbol{x}}}. \tag{6.7}$$

6.1.2 Taylor Series Expansion

Given a multivariate, scalar-valued function $f(\boldsymbol{x})$ operating on a vector of stochastic input data $\boldsymbol{x} = [x_1, x_2, \ldots]^T$. Expanding an n'th order Taylor series for $f(\boldsymbol{x})$ around the mean vector $\boldsymbol{\mu}_{\boldsymbol{x}} = [\mu_{x_1}, \mu_{x_2}, \ldots]^T$ gives:

$$\begin{aligned} f(\boldsymbol{x}) &= \mathrm{T}_n(f(\boldsymbol{x})) + \mathrm{R}_n(f(\boldsymbol{x})) \\ &= \sum_{k=0}^{n} \frac{\mathsf{D}^{(k)} f(\boldsymbol{\mu}_{\boldsymbol{x}})}{k!} \left(\boldsymbol{x} - \boldsymbol{\mu}_{\boldsymbol{x}}\right)^k + \mathrm{R}_n(f(\boldsymbol{x})). \end{aligned} \tag{6.8}$$

Therein, $\mathsf{D}^{(k)} f(\boldsymbol{\mu}_{\boldsymbol{x}})$ denotes the k'th order partial derivatives of the function $f(\boldsymbol{x})$ with respect to the elements of $\boldsymbol{x}$, evaluated at $\boldsymbol{\mu}_{\boldsymbol{x}}$. Furthermore, $\mathrm{R}_n(f(\boldsymbol{x}))$ terms the remainder term associated with $\mathrm{T}_n(f(\boldsymbol{x}))$.

6.1.2.1 The Approximation Error Associated with a Taylor Series

According to Lagrange (see e.g. Bronstein [7]), the remainder term associated with an n'th order Taylor series can be formulated as:

$$\mathrm{R}_n(f(\boldsymbol{x})) = \frac{\mathsf{D}^{(n+1)} f(\boldsymbol{\xi})}{(n+1)!} (\boldsymbol{x} - \boldsymbol{\mu}_{\boldsymbol{x}})^{n+1}, \tag{6.9}$$

with $\mathsf{D}^{(n+1)} f(\boldsymbol{\xi})$ terming the partial derivatives of order $n+1$ of the function $f(\boldsymbol{x})$ with respect to the elements of $\boldsymbol{x}$, evaluated at $\boldsymbol{\xi} = [\xi_1, \xi_2, \ldots]^T$. Therein, the ξ_i are numbers within the following open intervals: $\xi_i \in (\mu_{x_i}, x_i)$.

In order to determine the maximum approximation error associated with the n'th order Taylor series $\mathrm{T}_n(f(\boldsymbol{x}))$, the ξ_i are to be found such that $\mathrm{R}_n(f(\boldsymbol{x}))$ becomes a maximum. Due to the stochastic nature of the input data $\boldsymbol{x}$, the approximation error has to be understood as a confidence interval rather than a strict upper error bound.

Criminisi et al. [11, 10] proposed to introduce a statistical model for the particular ξ_i, namely $\xi_i = \mu_{x_i} \pm \alpha\sigma_{x_i}$, to take the stochastic nature of the input data x_i into account. Therein, μ_{x_i} and σ_{x_i} term the expectation values respectively the standard deviation values of the particular x_i. Moreover, the factor α is chosen such that it reflects the desired level of significance p associated with the confidence interval. For Gaussian distributed data, the significance levels p for $\alpha = \{1, 2, 3\}$ are:

α	1	2	3
p	68.3%	95.4%	99.7%

Table 6.1: Significance levels p associated with confidence intervals, assuming Gaussian distributed data.

6.1.3 The Confidence Interval Associated with First Order Estimates of Error Propagation

The task now is to compute a confidence interval associated with the result of first order error propagation applied to a non-linear function $f(\boldsymbol{x})$ (cf. Equation (6.1)). Assuming the random vector of uncertain input data $\boldsymbol{x}$ to exhibit Gaussian characteristics, this task is perfectly equivalent to computing the confidence interval associated with the variance of the first order Taylor series $\mathrm{T}_1(f(\boldsymbol{x}))$. Thus, we expand a first order Taylor series:

$$f(\boldsymbol{x}) = \mathrm{T}_1(f(\boldsymbol{x})) + \mathrm{R}_1(f(\boldsymbol{x})), \tag{6.10}$$

with $\mathrm{R}_1(f(\boldsymbol{x}))$ representing the Lagrange remainder term associated with the first order Taylor series $\mathrm{T}_1(f(\boldsymbol{x}))$. Referring to Equation (6.9), the Lagrange remainder term associated with the first order Taylor series $\mathrm{T}_1(f(\boldsymbol{x}))$ results to:

$$R_1(f(\boldsymbol{x})) = \frac{1}{2}\boldsymbol{e}_{\boldsymbol{x}}^T \mathsf{D}^{(2)} f(\boldsymbol{\xi}) \boldsymbol{e}_{\boldsymbol{x}}. \tag{6.11}$$

Therein, the term $\mathsf{D}^{(2)} f(\boldsymbol{\xi})$ denotes the Hessian matrix, i.e. the matrix of second order partial derivatives of $f(\boldsymbol{x})$ with respect to the elements of $\boldsymbol{x}$, evaluated at $\boldsymbol{\xi} = [\xi_1, \xi_2, \ldots]^T$. For a function of dimensionality p, the Hessian matrix is structured as follows:

$$\mathsf{D}^{(2)} f(\boldsymbol{\xi}) = \begin{bmatrix} \frac{\partial^2 f_1}{\partial x_1^2} & \frac{\partial^2 f_1}{\partial x_1 \partial x_2} & \cdots & \frac{\partial^2 f_1}{\partial x_1 \partial x_p} \\ \frac{\partial^2 f_2}{\partial x_1 \partial x_2} & \frac{\partial^2 f_2}{\partial x_2^2} & \cdots & \frac{\partial^2 f_2}{\partial x_2 \partial x_p} \\ \vdots & \vdots & \ddots & \vdots \\ \frac{\partial^2 f_p}{\partial x_1 \partial x_p} & \frac{\partial^2 f_p}{\partial x_2 \partial x_p} & \cdots & \frac{\partial^2 f_p}{\partial x_p^2} \end{bmatrix}_{[\xi_1, \ldots, \xi_p]^T}. \tag{6.12}$$

According to the principle described in the previous section, the confidence interval associated with the variance $\mathrm{V}(\mathrm{T}_1(f(\boldsymbol{x})))$ can be determined by means of the variance $\mathrm{V}(\mathrm{R}_1(f(\boldsymbol{x})))$ of the Lagrange remainder term. Referring to Section 2.1.1, this variance is defined as:

$$\mathrm{V}(\mathrm{R}_1(f(\boldsymbol{x}))) = \mathrm{E}\left(\mathrm{R}_1(f(\boldsymbol{x}))^2\right) - \mathrm{E}(\mathrm{R}_1(f(\boldsymbol{x})))^2. \tag{6.13}$$

The two required expectation values can be computed by application of the analytical definition of expectation values (cf. Equation (2.22)) from the following integrals:

$$\mathrm{E}(R_1(f(\boldsymbol{x}))) = \frac{1}{2}\int_{-\infty}^{\infty} \boldsymbol{e}_{\boldsymbol{x}}^T \mathsf{D}^{(2)} f(\boldsymbol{\xi}) \boldsymbol{e}_{\boldsymbol{x}} \frac{\sqrt{|\boldsymbol{\Lambda}_{\boldsymbol{x}}^{-1}|}}{(2\pi)^{\frac{p}{2}}} \mathrm{e}^{-\frac{1}{2}\boldsymbol{e}_{\boldsymbol{x}}^T \boldsymbol{\Lambda}_{\boldsymbol{x}}^{-1} \boldsymbol{e}_{\boldsymbol{x}}} \,\mathrm{d}\boldsymbol{e}_{\boldsymbol{x}}, \tag{6.14}$$

$$\mathrm{E}(R_1(f(\boldsymbol{x}))^2) = \frac{1}{4}\int_{-\infty}^{\infty} \left(\boldsymbol{e}_{\boldsymbol{x}}^T \mathsf{D}^{(2)} f(\boldsymbol{\xi}) \boldsymbol{e}_{\boldsymbol{x}}\right)^2 \frac{\sqrt{|\boldsymbol{\Lambda}_{\boldsymbol{x}}^{-1}|}}{(2\pi)^{\frac{p}{2}}} \mathrm{e}^{-\frac{1}{2}\boldsymbol{e}_{\boldsymbol{x}}^T \boldsymbol{\Lambda}_{\boldsymbol{x}}^{-1} \boldsymbol{e}_{\boldsymbol{x}}} \,\mathrm{d}\boldsymbol{e}_{\boldsymbol{x}}. \tag{6.15}$$

As a consequence of the chosen model, all of the functions to be integrated contain products of perturbation values e_{x_i} raised to the power of exponents $k_i = \{1, 2, 3, \ldots\}$. Thus, these functions are of the form $f(e_{x_1}^{k_1}, e_{x_2}^{k_2}, \ldots)$. In Table 6.2, a list of functions of this type is presented together with the corresponding expectation values.

$\sum_{i=1}^{4} k_i$	$f(e_{x_1}^{k_1}, e_{x_2}^{k_2}, e_{x_3}^{k_3}, e_{x_4}^{k_4})$	$\mathrm{E}(f(e_{x_1}^{k_1}, e_{x_2}^{k_2}, e_{x_3}^{k_3}, e_{x_4}^{k_4}))$
1	e_{x_1}	0
2	$e_{x_1}^2$	$\sigma_{x_1}^2$
	$e_{x_1} e_{x_2}$	$\sigma_{x_1 x_2}$
3	$e_{x_1}^3$	0
	$e_{x_1}^2 e_{x_2}$	0
	$e_{x_1} e_{x_2} e_{x_3}$	0
4	$e_{x_1}^4$	$3\sigma_{x_1}^4$
	$e_{x_1}^3 e_{x_2}$	$3\sigma_{x_1}^2 \sigma_{x_1 x_2}$
	$e_{x_1}^2 e_{x_2}^2$	$\sigma_{x_1}^2 \sigma_{x_2}^2 + 2\sigma_{x_1 x_2}^2$
	$e_{x_1}^2 e_{x_2} e_{x_3}$	$\sigma_{x_1}^2 \sigma_{x_2 x_3} + 2\sigma_{x_1 x_2} \sigma_{x_1 x_3}$
	$e_{x_1} e_{x_2} e_{x_3} e_{x_4}$	$\sigma_{x_1 x_2} \sigma_{x_3 x_4} + \sigma_{x_1 x_3} \sigma_{x_2 x_4} + \sigma_{x_1 x_4} \sigma_{x_2 x_3}$

Table 6.2: A list of functions $f(e_{x_1}^{k_1}, e_{x_2}^{k_2}, e_{x_3}^{k_3}, e_{x_4}^{k_4})$ with corresponding expectation values. The expectation values were computed by means of the analytical definition of expectation values and integrating out the parameters e_{x_i}.

All of the terms listed in Table 6.2 appear in the examples presented in Section 6.2. Note that the expectation values of those functions $f(e_{x_1}^{k_1}, e_{x_2}^{k_2}, e_{x_3}^{k_3}, e_{x_4}^{k_4})$ that show uneven sums of exponents, $\sum_{i=1}^{4} k_i$, are zero. This is a result of the fact that these functions exhibit uneven characteristics. Thus, integration over the range $-\infty$ to ∞ (cf. Equation (2.22)) results in positive and negative contributions, which entirely nullify.

6.2 Analysis of Non-Linear Functions

The applicability of the concept described in the previous section is demonstrated with two non-linear functions typically arising in metric vision tasks, namely:

- calculation of the Euclidean distance between two uncertain points as well as the variance associated with it, and
- computation of the inhomogeneous coordinates of an uncertain point on the projective plane, given the set of homogeneous point coordinates. The elements of the resulting 2×2 covariance matrix, i.e. the variances of the inhomogeneous point coordinates as well as the covariance between them, are analyzed separately.

All of the results presented have been analytically derived with the symbolic math processing tool Maple® and were numerically verified by means of Monte-Carlo experiments.

6.2.1 The Euclidean Distance between two Uncertain Points

Given two uncertain points on the projective plane with inhomogeneous coordinate vectors $\boldsymbol{p}_1 = [x_1, y_1]^T$ and $\boldsymbol{p}_2 = [x_2, y_2]^T$ respectively. The Euclidean distance d between the two points is given as:

$$d = \left(\Delta x^2 + \Delta y^2\right)^{\frac{1}{2}}, \tag{6.16}$$

with:

$$\begin{array}{rcl} \Delta x & = & x_1 - x_2, \\ \Delta y & = & y_1 - y_2. \end{array} \tag{6.17}$$

Applying the principle of first order error propagation to this non-linear function gives an estimate of the variance σ_d^2 rather than the "true" variance itself. Thus, we need to determine a confidence interval associated with this first order estimate.

6.2.1.1 Statistical Model of the Point Coordinates

Each of the particular point coordinates is modelled as the sum of a perturbation-free mean value (i.e. it is assumed, that the mean value can be computed from a sufficiently large number of samples such that the uncertainty in the mean value can be neglected) and an uncertain perturbation parameter [33]:

$$\begin{array}{rcl} x_1 & = & \mu_{x_1} + e_{x_1}, \\ y_1 & = & \mu_{y_1} + e_{y_1}, \end{array} \tag{6.18}$$

$$\begin{array}{rcl} x_2 & = & \mu_{x_2} + e_{x_2}, \\ y_2 & = & \mu_{y_2} + e_{y_2}, \end{array} \tag{6.19}$$

with μ_{x_1}, μ_{y_1}, μ_{x_2} and μ_{y_2} terming the mean values and e_{x_1}, e_{y_1}, e_{x_2} and e_{y_2} denoting the perturbation parameters. To simplify matters, the vectors of the coordinate means $\boldsymbol{\mu}_p = [\mu_{x_1}, \mu_{y_1}, \mu_{x_2}, \mu_{y_2}]^T$ and perturbation parameters $\boldsymbol{e}_p = [e_{x_1}, e_{y_1}, e_{x_2}, e_{y_2}]^T$ are introduced. It is assumed that the perturbation parameters follow a common Gaussian probability density function, i.e.:

$$\boldsymbol{e}_p \sim \mathcal{N}(\boldsymbol{e}_p, \boldsymbol{o}, \Lambda_p) = \left((2\pi)^2 \left|\Lambda_p\right|\right)^{-\frac{1}{2}} \mathrm{e}^{-\frac{1}{2}\boldsymbol{e}_p^T \Lambda_p^{-1} \boldsymbol{e}_p}, \tag{6.20}$$

with the covariance matrix:

$$\Lambda_p = \begin{bmatrix} \sigma_{x_1}^2 & \sigma_{x_1y_1} & \sigma_{x_1x_2} & \sigma_{x_1y_2} \\ \sigma_{x_1y_1} & \sigma_{y_1}^2 & \sigma_{y_1x_2} & \sigma_{y_1y_2} \\ \sigma_{x_1x_2} & \sigma_{y_1x_2} & \sigma_{x_2}^2 & \sigma_{x_2y_2} \\ \sigma_{x_1y_2} & \sigma_{y_1y_2} & \sigma_{x_2y_2} & \sigma_{y_2}^2 \end{bmatrix}. \tag{6.21}$$

6.2.1.2 First Order Estimation of Error Propagation

Applying the law of first order error propagation, the variance σ_d^2 is estimated as:

$$\sigma_d^2 \approx \mathsf{J}_d \Lambda_p {\mathsf{J}_d}^T, \tag{6.22}$$

with J_d denoting the vector of first order partial derivatives of d with respect to the elements of $\boldsymbol{p} = [x_1, y_1, x_2, y_2]^T$, evaluated at the coordinate means:

$$\mathsf{J}_d = \left(\Delta\mu_x^2 + \Delta\mu_y^2\right)^{-\frac{1}{2}} \begin{bmatrix} \Delta\mu_x & \Delta\mu_y & -\Delta\mu_x & -\Delta\mu_y \end{bmatrix}. \tag{6.23}$$

Therein, $\Delta\mu_x$ and $\Delta\mu_y$ denote the differences of coordinate means:

$$\begin{aligned} \Delta\mu_x &= \mu_{x_1} - \mu_{x_2}, \\ \Delta\mu_y &= \mu_{y_1} - \mu_{y_2}. \end{aligned} \tag{6.24}$$

Thus, we can estimate the variance associated with the distance d as:

$$\sigma_d^2 \approx \left(\Delta\mu_x^2 + \Delta\mu_y^2\right)^{-1} \left(\Delta\mu_x^2\Phi_x + \Delta\mu_y^2\Phi_y + 2\Delta\mu_x\Delta\mu_y\Phi_{xy}\right), \tag{6.25}$$

with:

$$\begin{aligned} \Phi_x &= \sigma_{x_1}^2 - 2\sigma_{x_1x_2} + \sigma_{x_2}^2, \\ \Phi_y &= \sigma_{y_1}^2 - 2\sigma_{y_1y_2} + \sigma_{y_2}^2, \\ \Phi_{xy} &= \sigma_{x_1y_1} + \sigma_{x_2y_2} - \sigma_{x_1y_2} - \sigma_{y_1x_2}. \end{aligned} \tag{6.26}$$

6.2.1.3 The Approximation Error Associated with the First Order Estimate

Expanding a first order Taylor series for d around the coordinate means $\boldsymbol{\mu}_p$ gives:

$$d = \mathrm{T}_1(d) + \mathrm{R}_1(d), \tag{6.27}$$

with the first order Taylor approximation $\mathrm{T}_1(d)$ and the associated Lagrange remainder

term $\mathrm{R}_1(d)$ being:

$$\mathrm{T}_1(d) = \left(\Delta x^2 + \Delta y^2\right)^{\frac{1}{2}}\Big|_{\substack{x_1=\mu_{x_1}\\ y_1=\mu_{y_1}\\ x_2=\mu_{x_2}\\ y_2=\mu_{y_2}}} + \mathsf{J}_d|_{\substack{x_1=\mu_{x_1}\\ y_1=\mu_{y_1}\\ x_2=\mu_{x_2}\\ y_2=\mu_{y_2}}} \begin{bmatrix} x_1-\mu_{x_1}\\ y_1-\mu_{y_1}\\ x_2-\mu_{x_2}\\ y_2-\mu_{y_2}\end{bmatrix}, \tag{6.28}$$

$$\mathrm{R}_1(d) = \frac{1}{2}\begin{bmatrix} x_1-\mu_{x_1}\\ y_1-\mu_{y_1}\\ x_2-\mu_{x_2}\\ y_2-\mu_{y_2}\end{bmatrix}^T \mathsf{H}_d|_{\substack{x_1=\xi_{x_1}\\ y_1=\xi_{y_1}\\ x_2=\xi_{x_2}\\ y_2=\xi_{y_2}}} \begin{bmatrix} x_1-\mu_{x_1}\\ y_1-\mu_{y_1}\\ x_2-\mu_{x_2}\\ y_2-\mu_{y_2}\end{bmatrix}. \tag{6.29}$$

Therein, the Jacobian matrix J_d and the Hessian matrix H_d are:

$$\mathsf{J}_d = \left(\Delta x^2 + \Delta y^2\right)^{-\frac{1}{2}}\begin{bmatrix}\Delta x & \Delta y & -\Delta x & -\Delta y\end{bmatrix}, \tag{6.30}$$

$$\mathsf{H}_d = \left(\Delta x^2 + \Delta y^2\right)^{-\frac{3}{2}}\begin{bmatrix} \Delta y^2 & -\Delta x\Delta y & -\Delta y^2 & \Delta x\Delta y\\ -\Delta x\Delta y & \Delta x^2 & \Delta x\Delta y & -\Delta x^2\\ -\Delta y^2 & \Delta x\Delta y & \Delta y^2 & -\Delta x\Delta y\\ \Delta x\Delta y & -\Delta x^2 & -\Delta x\Delta y & \Delta x^2\end{bmatrix}. \tag{6.31}$$

Thus, we obtain:

$$\begin{aligned}\mathrm{T}_1(d) &= \left(\Delta\mu_x^2 + \Delta\mu_y^2\right)^{\frac{1}{2}} + \left(\Delta\mu_x^2 + \Delta\mu_y^2\right)^{-\frac{1}{2}}\left(\Delta\mu_x\Delta e_x + \Delta\mu_y\Delta e_y\right),\\ \mathrm{R}_1(d) &= \frac{1}{2}\left(\Delta\xi_x^2 + \Delta\xi_y^2\right)^{-\frac{3}{2}}\left(\Delta\xi_x^2\Delta e_y^2 + \Delta\xi_y^2\Delta e_x^2 - 2\Delta\xi_x\Delta\xi_y\Delta e_x\Delta e_y\right) \qquad (6.32)\\ &= \frac{1}{2}\left(\Delta\xi_x^2 + \Delta\xi_y^2\right)^{-\frac{3}{2}}\left(\Delta\xi_x\Delta e_y - \Delta\xi_y\Delta e_x\right)^2, \qquad (6.33)\end{aligned}$$

with:

$$\begin{aligned}\Delta e_x &= e_{x_1} - e_{x_2}, \qquad (6.34)\\ \Delta e_y &= e_{y_1} - e_{y_2},\end{aligned} \qquad \begin{aligned}\Delta\xi_x &= \xi_{x_1} - \xi_{x_2}, \qquad (6.35)\\ \Delta\xi_y &= \xi_{y_1} - \xi_{y_2}.\end{aligned}$$

The variance of the first order Taylor approximation $\mathrm{T}_1(d)$ is computed as:

$$\mathrm{V}(\mathrm{T}_1(d)) = \mathrm{E}(\mathrm{T}_1(d)^2) - \mathrm{E}(\mathrm{T}_1(d))^2, \tag{6.36}$$

whereas the required expectation values are calculated as:

$$\begin{aligned}\mathrm{E}(\mathrm{T}_1(d)) &= \mathrm{E}\left(\left(\Delta\mu_x^2 + \Delta\mu_y^2\right)^{\frac{1}{2}} + \left(\Delta\mu_x^2 + \Delta\mu_y^2\right)^{-\frac{1}{2}}\left(\Delta\mu_x\Delta e_x + \Delta\mu_y\Delta e_y\right)\right)\\ &= \left(\Delta\mu_x^2 + \Delta\mu_y^2\right)^{\frac{1}{2}}, \qquad (6.37)\\ \mathrm{E}(\mathrm{T}_1(d))^2 &= \Delta\mu_x^2 + \Delta\mu_y^2, \qquad (6.38)\\ \mathrm{E}(\mathrm{T}_1(d)^2) &= \mathrm{E}\left(\Delta\mu_x^2 + \Delta\mu_y^2 + 2\left(\Delta\mu_x\Delta e_x + \Delta\mu_y\Delta e_y\right)\right.\\ &\quad \left. + \left(\Delta\mu_x^2 + \Delta\mu_y^2\right)^{-1}\left(\Delta\mu_x^2\Delta e_x^2 + \Delta\mu_y^2\Delta e_y^2 + 2\Delta\mu_x\Delta\mu_y\Delta e_x\Delta e_y\right)\right)\\ &= \Delta\mu_x^2 + \Delta\mu_y^2 + \left(\Delta\mu_x^2 + \Delta\mu_y^2\right)^{-1}\left(\Delta\mu_x^2\Phi_x + \Delta\mu_y^2\Phi_y + 2\Delta\mu_x\Delta\mu_y\Phi_{xy}\right). \qquad (6.39)\end{aligned}$$

Note that these results are obtained utilizing the following terms (cf. Table 6.2):

$$\begin{aligned}
\mathrm{E}\left(\Delta e_x\right) &= \mathrm{E}\left(e_{x_1} - e_{x_2}\right) &&= 0,\\
\mathrm{E}\left(\Delta e_y\right) &= \mathrm{E}\left(e_{y_1} - e_{y_2}\right) &&= 0,\\
\mathrm{E}\left(\Delta e_x^2\right) &= \mathrm{E}\left(e_{x_1}^2 - 2e_{x_1}e_{x_2} + e_{x_2}^2\right) &&\\
&= \sigma_{x_1}^2 - 2\sigma_{x_1x_2} + \sigma_{x_2}^2 &&= \Phi_x,\\
\mathrm{E}\left(\Delta e_y^2\right) &= \mathrm{E}\left(e_{y_1}^2 - 2e_{y_1}e_{y_2} + e_{y_2}^2\right) &&\\
&= \sigma_{y_1}^2 - 2\sigma_{y_1y_2} + \sigma_{y_2}^2 &&= \Phi_y,\\
\mathrm{E}\left(\Delta e_x \Delta e_y\right) &= \mathrm{E}\left(e_{x_1}e_{y_1} + e_{x_2}e_{y_2} - e_{x_1}e_{y_2} - e_{y_1}e_{x_2}\right) &&\\
&= \sigma_{x_1y_1} + \sigma_{x_2y_2} - \sigma_{x_1y_2} - \sigma_{y_1x_2} &&= \Phi_{xy}.
\end{aligned}$$

Finally, the variance of the first order Taylor approximation $\mathrm{T}_1(d)$ results to:

$$\mathrm{V}(\mathrm{T}_1(d)) = \left(\Delta\mu_x^2 + \Delta\mu_y^2\right)^{-1}\left(\Delta\mu_x^2\Phi_x + \Delta\mu_y^2\Phi_y + 2\Delta\mu_x\Delta\mu_y\Phi_{xy}\right). \tag{6.40}$$

As expected, this is perfectly equivalent to Equation (6.25), the result of first order error propagation.

In order to determine the approximation error associated with $\mathrm{V}(\mathrm{T}_1(d))$, we compute the variance of the Lagrange remainder term $\mathrm{R}_1(d)$:

$$\mathrm{V}\left(\mathrm{R}_1(d)\right) = \mathrm{E}\left(\mathrm{R}_1(d)^2\right) - \mathrm{E}\left(\mathrm{R}_1(d)\right)^2. \tag{6.41}$$

The required expectation values are calculated as:

$$\mathrm{E}\left(\mathrm{R}_1(d)\right) = \frac{1}{2}\left(\Delta\xi_x^2 + \Delta\xi_y^2\right)^{-\frac{3}{2}}\left(\Delta\xi_x^2\Phi_y + \Delta\xi_y^2\Phi_x - 2\Delta\xi_x\Delta\xi_y\Phi_{xy}\right), \tag{6.42}$$

$$\begin{aligned}
\mathrm{E}\left(\mathrm{R}_1(d)\right)^2 &= \frac{1}{4}\left(\Delta\xi_x^2 + \Delta\xi_y^2\right)^{-3}\left(\Delta\xi_x^4\Phi_y^2 + \Delta\xi_y^4\Phi_x^2 + 2\Delta\xi_x^2\Delta\xi_y^2\Phi_x\Phi_y\right.\\
&\quad \left. + 4\Delta\xi_x^2\Delta\xi_y^2\Phi_{xy}^2 - 4\Delta\xi_x^3\Delta\xi_y\Phi_y\Phi_{xy} - 4\Delta\xi_x\Delta\xi_y^3\Phi_x\Phi_{xy}\right),
\end{aligned} \tag{6.43}$$

$$\begin{aligned}
\mathrm{E}\left(\mathrm{R}_1(d)^2\right) &= \mathrm{E}\left(\frac{1}{4}\left(\Delta\xi_x^2 + \Delta\xi_y^2\right)^{-3}\left(\Delta\xi_x^4\Delta e_y^4 + \Delta\xi_y^4\Delta e_x^4 + 6\Delta\xi_x^2\Delta\xi_y^2\Delta e_x^2\Delta e_y^2\right.\right.\\
&\qquad \left.\left. - 4\Delta\xi_x^3\Delta\xi_y\Delta e_x\Delta e_y^3 - 4\Delta\xi_x\Delta\xi_y^3\Delta e_x^3\Delta e_y\right)\right)\\
&= \frac{1}{4}\left(\Delta\xi_x^2 + \Delta\xi_y^2\right)^{-3}\left(3\Delta\xi_x^4\Phi_y^2 + 3\Delta\xi_y^4\Phi_x^2 + 6\Delta\xi_x^2\Delta\xi_y^2\Phi_x\Phi_y\right.\\
&\quad \left. + 12\Delta\xi_x^2\Delta\xi_y^2\Phi_{xy}^2 - 12\Delta\xi_x^3\Delta\xi_y\Phi_y\Phi_{xy} - 12\Delta\xi_x\Delta\xi_y^3\Phi_x\Phi_{xy}\right).
\end{aligned} \tag{6.44}$$

Note that these results are obtained applying the following terms (cf. Table 6.2):

$$
\begin{aligned}
\mathrm{E}\left(\Delta e_x^4\right) &= \mathrm{E}\left(e_{x_1}^4 - 4e_{x_1}^3 e_{x_2} + 6e_{x_1}^2 e_{x_2}^2 - 4e_{x_1} e_{x_2}^3 + e_{x_2}^4\right) \\
&= 3\left(\sigma_{x_1}^2 - 2\sigma_{x_1x_2} + \sigma_{x_2}^2\right)^2 &&= 3\Phi_x^2, \\
\mathrm{E}\left(\Delta e_y^4\right) &= \mathrm{E}\left(e_{y_1}^4 - 4e_{y_1}^3 e_{y_2} + 6e_{y_1}^2 e_{y_2}^2 - 4e_{y_1} e_{y_2}^3 + e_{y_2}^4\right) \\
&= 3\left(\sigma_{y_1}^2 - 2\sigma_{y_1y_2} + \sigma_{y_2}^2\right)^2 &&= 3\Phi_y^2, \\
\mathrm{E}\left(\Delta e_x^3 \Delta e_y\right) &= \mathrm{E}\left(e_{x_1}^3 e_{y_1} - e_{x_1}^3 e_{y_2} + e_{y_1} e_{x_2}^3 - e_{x_2}^3 e_{y_2}\right. \\
&\quad \left. - 3e_{x_1}^2 e_{y_1} e_{x_2} + 3e_{x_1}^2 e_{x_2} e_{y_2} + 3e_{x_1} e_{y_1} e_{x_2}^2 - 3e_{x_1} e_{x_2}^2 e_{y_2}\right) \\
&= 3\left(\sigma_{x_1}^2 - 2\sigma_{x_1x_2} + \sigma_{x_2}^2\right)\left(\sigma_{x_1y_1} + \sigma_{x_2y_2} - \sigma_{x_1y_2} - \sigma_{y_1x_2}\right) &&= 3\Phi_x\Phi_{xy}, \\
\mathrm{E}\left(\Delta e_x \Delta e_y^3\right) &= \mathrm{E}\left(e_{x_1} e_{y_1}^3 - e_{y_1}^3 e_{x_2} + e_{x_1} e_{y_2}^3 - e_{x_2} e_{y_2}^3\right. \\
&\quad \left. - 3e_{x_1} e_{y_1}^2 e_{y_2} + 3e_{y_1}^2 e_{x_2} e_{y_2} + 3e_{x_1} e_{y_1} e_{y_2}^2 - 3e_{y_1} e_{x_2} e_{y_2}^2\right) \\
&= 3\left(\sigma_{y_1}^2 - 2\sigma_{y_1y_2} + \sigma_{y_2}^2\right)\left(\sigma_{x_1y_1} + \sigma_{x_2y_2} - \sigma_{x_1y_2} - \sigma_{y_1x_2}\right) &&= 3\Phi_y\Phi_{xy}, \\
\mathrm{E}\left(\Delta e_x^2 \Delta e_y^2\right) &= \mathrm{E}\left(e_{x_1}^2 e_{y_1}^2 + e_{x_1}^2 e_{y_2}^2 + e_{y_1}^2 e_{x_2}^2 + e_{x_2}^2 e_{y_2}^2\right. \\
&\quad - 2\left(e_{x_1}^2 e_{y_1} e_{y_2} + e_{x_1} e_{y_1}^2 e_{x_2} + e_{x_1} e_{x_2} e_{y_2}^2 + e_{y_1} e_{x_2}^2 e_{y_2}\right) \\
&\quad \left. + 4e_{x_1} e_{y_1} e_{x_2} e_{y_2}\right) \\
&= \left(\sigma_{x_1}^2 - 2\sigma_{x_1x_2} + \sigma_{x_2}^2\right)\left(\sigma_{y_1}^2 - 2\sigma_{y_1y_2} + \sigma_{y_2}^2\right) \\
&\quad + 2\left(\sigma_{x_1y_1} + \sigma_{x_2y_2} - \sigma_{x_1y_2} - \sigma_{y_1x_2}\right)^2 &&= \Phi_x\Phi_y + 2\Phi_{xy}^2.
\end{aligned}
$$

Finally, the variance of the Lagrange remainder term $\mathrm{R}_1(d)$ is obtained as:

$$
\begin{aligned}
\mathrm{V}\left(\mathrm{R}_1(d)\right) &= \left(\Delta\xi_x^2 + \Delta\xi_y^2\right)^{-3} \left(\frac{1}{2}\left(\Delta\xi_x^4\Phi_y^2 + \Delta\xi_y^4\Phi_x^2\right) + \Delta\xi_x^2\Delta\xi_y^2\left(\Phi_x\Phi_y + 2\Phi_{xy}^2\right) \right. \\
&\quad \left. - 2\left(\Delta\xi_x^3\Delta\xi_y\Phi_y\Phi_{xy} + \Delta\xi_x\Delta\xi_y^3\Phi_x\Phi_{xy}\right)\right). \qquad (6.45)
\end{aligned}
$$

In order to determine a confidence interval associated with the variance $\mathrm{V}(\mathrm{T}_1(d))$, the maximum value of $\mathrm{V}\left(\mathrm{R}_1(d)\right)$ concerning $\xi_{x_1} \in (x_1, \mu_{x_1})$, $\xi_{y_1} \in (y_1, \mu_{y_1})$, $\xi_{x_2} \in (x_2, \mu_{x_2})$ and $\xi_{y_2} \in (y_2, \mu_{y_2})$ is computed. Both, $\Delta\xi_x$ as well as $\Delta\xi_y$ are dominant in the denominator of Equation (6.45). Thus, assuming $\mu_{x_1} > \mu_{x_2}$ and $\mu_{y_1} > \mu_{y_2}$, we choose the models:

$$
\begin{aligned}
\xi_{x_1} &= \mu_{x_1} - \alpha\sigma_{x_1}, \\
\xi_{x_2} &= \mu_{x_2} + \alpha\sigma_{x_2},
\end{aligned}
\qquad (6.46)
\qquad
\begin{aligned}
\xi_{y_1} &= \mu_{y_1} - \alpha\sigma_{y_1}, \\
\xi_{y_2} &= \mu_{y_2} + \alpha\sigma_{y_2},
\end{aligned}
\qquad (6.47)
$$

and obtain:

$$
\begin{aligned}
\Delta\xi_x &= \mu_{x_1} - \mu_{x_2} - \alpha\left(\sigma_{x_1} + \sigma_{x_2}\right), \\
\Delta\xi_y &= \mu_{y_1} - \mu_{y_2} - \alpha\left(\sigma_{y_1} + \sigma_{y_2}\right).
\end{aligned}
\qquad (6.48)
$$

Therein, the factor $\alpha = \{1, 2, 3\}$ specifies the level of significance associated with the confidence interval. Substituting $\Delta\xi_x$ and $\Delta\xi_y$ into Equation (6.45) gives an absolute confidence interval $b_{\mathrm{V}(\mathrm{T}_1(d))}$ associated with the first order estimate of the variance σ_d^2. In addition to this, a relative confidence interval $b_{\mathrm{V}(\mathrm{T}_1(d)),r}$ can be obtained by relating $b_{\mathrm{V}(\mathrm{T}_1(d))}$ to the first order estimate $\mathrm{V}(\mathrm{T}_1(d))$.

Both, $b_{\mathrm{V}(\mathrm{T}_1(d))}$ as well as $b_{\mathrm{V}(\mathrm{T}_1(d)),r}$ are lengthy expressions and thus, they are not listed here explicitly.

6.2.2 Numerical Verification

Two sets of data points, each consisting of 10^6 samples, are randomly generated (cf. Section 2.3.2) based on a Gaussian probability density function with coordinate mean vector:

$$\boldsymbol{\mu}_p = \begin{bmatrix} \mu_{x_1} \\ \mu_{y_1} \\ \mu_{x_2} \\ \mu_{y_2} \end{bmatrix} = \begin{bmatrix} 20 \\ 20 \\ 10 \\ 10 \end{bmatrix}, \tag{6.49}$$

and covariance matrix:

$$\Lambda_p = \begin{bmatrix} 0.5 & 0.1 & 0.05 & 0.05 \\ 0.1 & 0.3 & 0.05 & 0.05 \\ 0.05 & 0.05 & 0.5 & 0.1 \\ 0.05 & 0.05 & 0.1 & 0.3 \end{bmatrix}. \tag{6.50}$$

Note that in this example, units were omitted as they are not significant for the interpretation of the results.

At first, the Euclidean distance between all pairs of sample points as well as their variance is calculated. This value is considered to be the "true" variance σ_d^2 associated with the average Euclidean distance d between the points.

Subsequently, the first order Taylor approximation $\mathrm{T}_1(d)$ of the Euclidean distance (cf. Equation (6.25)) is determined together with the variance $\mathrm{V}(\mathrm{T}_1(d))$ associated with it (cf. Equation (6.40)). Finally, the absolute and relative confidence intervals, $b_{\mathrm{V}(\mathrm{T}_1(d))}$ and $b_{\mathrm{V}(\mathrm{T}_1(d)),r}$ respectively, are computed utilizing a significance level specified by $\alpha = 3$.

Table 6.3 gives a summary of the results obtained. As can be seen, the absolute value of the difference between the "true" variance σ_d^2 and the variance of the first order estimate of the Euclidean distance, $\mathrm{V}(\mathrm{T}_1(d))$, lies within the absolute confidence interval $b_{\mathrm{V}(\mathrm{T}_1(d))}$.

d	σ_d^2	$\mathrm{V}(\mathrm{T}_1(d))$	$\lvert\sigma_d^2 - \mathrm{V}(\mathrm{T}_1(d))\rvert$	$b_{\mathrm{V}(\mathrm{T}_1(d))}$	$b_{\mathrm{V}(\mathrm{T}_1(d)),r}$
14.16389	0.79896	0.80041	0.00145	0.00254	0.31777%

Table 6.3: Results of a Monte-Carlo experiment concerning the confidence interval associated with the variance $\mathrm{V}(\mathrm{T}_1(d))$ of the first order Taylor approximation of the Euclidean distance d between two points.

Examining Equations (6.45) and (6.48), one can see that the absolute and relative confidence intervals are related with the coordinates of the data points and thus, they are depending on the Euclidean distance between the points. In order to illustrate these characteristics, the vector of mean point coordinates $\boldsymbol{\mu}_{p_1} = [\mu_{x_1}, \mu_{y_1}]^T$ was scaled up to iteratively increase the distance d. Then, the procedure described above was repeated for each iteration.

Figure 6.1 visualizes the relative confidence interval $b_{\mathrm{V}(\mathrm{T}_1(d)),r}$ as a function of the distance d. As is clearly seen, the relative confidence interval decreases significantly with increasing distance d.

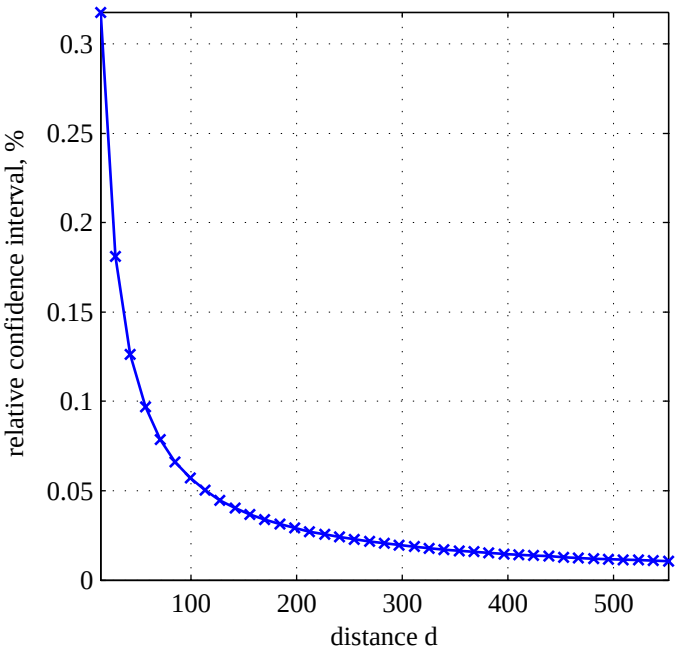

Figure 6.1: Relative confidence interval associated with the variance of the first order estimate $\mathrm{T}_1(d)$ as a function of d.

6.2.3 Computation of Inhomogeneous Point Coordinates

Given a point $\boldsymbol{p}$ on the projective plane with homogeneous coordinate vector $[u, v, w]^T$. The homogeneous coordinate vector can be a result of a preceding matrix operation, e.g. the application of a homography. It is assumed, that the coordinates are all subject to perturbation, thus there is a non-degenerate 3×3 covariance matrix Λ_{uvw} associated with them. The covariance matrix is structured as follows:

$$\Lambda_{uvw} = \begin{bmatrix} \sigma_u^2 & \sigma_{uv} & \sigma_{uw} \\ \sigma_{uv} & \sigma_v^2 & \sigma_{vw} \\ \sigma_{uw} & \sigma_{vw} & \sigma_w^2 \end{bmatrix}. \tag{6.51}$$

Computing the vector of inhomogeneous point coordinates,

$$\begin{bmatrix} x \\ y \end{bmatrix} = \frac{1}{w} \begin{bmatrix} u \\ v \end{bmatrix}, \tag{6.52}$$

obviously is a non-linear operation. Thus, applying the principle of first order error propagation merely gives an estimate of the 2×2 covariance matrix Λ_{xy} rather than the covariance matrix itself. Therefore, we need to determine confidence intervals for the particular components of the first order estimate of Λ_{xy}, which is composed as:

$$\Lambda_{xy} = \begin{bmatrix} \sigma_x^2 & \sigma_{xy} \\ \sigma_{xy} & \sigma_y^2 \end{bmatrix}. \tag{6.53}$$

6.2.3.1 Statistical Model of the Point Coordinates

Each of the homogeneous coordinates is modelled as the sum of an perturbation-free mean value, i.e. it is assumed that the mean value computed from a sufficiently large number of data sets such that its perturbation can be neglected, and an uncertain, mean-free perturbation parameter:

$$\begin{bmatrix} u \\ v \\ w \end{bmatrix} = \boldsymbol{p} = \boldsymbol{\mu}_{uvw} + \boldsymbol{e}_{uvw} = \begin{bmatrix} \mu_u \\ \mu_v \\ \mu_w \end{bmatrix} + \begin{bmatrix} e_u \\ e_v \\ e_w \end{bmatrix}. \tag{6.54}$$

Therein, $\boldsymbol{\mu}_{uvw}$ terms the vector of coordinate means μ_u, μ_v and μ_w and $\boldsymbol{e}_{uvw}$ denotes the vector of perturbation parameters e_u, e_v and e_w. Furthermore, it is assumed that the perturbation parameters follow a tri-variate Gaussian probability density function:

$$\boldsymbol{e}_{uvw} \sim \mathcal{N}(\boldsymbol{e}_{uvw}, \boldsymbol{o}, \Lambda_{uvw}) = \left((2\pi)^3 \left|\Lambda_{uvw}\right|\right)^{-\frac{1}{2}} \mathrm{e}^{-\frac{1}{2}\boldsymbol{e}_{uvw}^T \Lambda_{uvw}^{-1} \boldsymbol{e}_{uvw}}. \tag{6.55}$$

6.2.3.2 First Order Error Propagation

Applying the law of first order error propagation, the covariance matrix Λ_{xy} is estimated as:

$$\Lambda_{xy} \approx \mathsf{J}_N \Lambda_{uvw} {\mathsf{J}_N}^T, \tag{6.56}$$

with J_N denoting the Jacobian matrix of the inhomogeneous coordinate vector with respect to the homogeneous point coordinates, evaluated at the coordinate means:

$$\mathsf{J}_N = \frac{1}{\mu_w^2} \begin{bmatrix} \mu_w & 0 & -\mu_u \\ 0 & \mu_w & -\mu_v \end{bmatrix}. \tag{6.57}$$

Thus, we obtain the first order estimate of the covariance matrix Λ_{xy} as:

$$\Lambda_{xy} \approx \begin{bmatrix} \mathrm{V}(\mathrm{T}_1(x)) & \mathrm{Cov}(\mathrm{T}_1(x)\mathrm{T}_1(y)) \\ \mathrm{Cov}(\mathrm{T}_1(x)\mathrm{T}_1(y)) & \mathrm{V}(\mathrm{T}_1(y)) \end{bmatrix} \tag{6.58}$$

with:

$$\begin{aligned} \mathrm{V}(\mathrm{T}_1(x)) &= \frac{1}{\mu_w^4}\left(\mu_w^2\sigma_u^2 - 2\mu_u\mu_w\sigma_{uw} + \mu_u^2\sigma_w^2\right), \\ \mathrm{Cov}(\mathrm{T}_1(x)\mathrm{T}_1(y)) &= \frac{1}{\mu_w^4}\left(\mu_w^2\sigma_{uv} - \mu_w\left(\mu_u\sigma_{vw} + \mu_v\sigma_{uw}\right) + \mu_u\mu_v\sigma_w^2\right), \\ \mathrm{V}(\mathrm{T}_1(y)) &= \frac{1}{\mu_w^4}\left(\mu_w^2\sigma_v^2 - 2\mu_v\mu_w\sigma_{vw} + \mu_v^2\sigma_w^2\right). \end{aligned} \tag{6.59}$$

In the following sections, confidence intervals associated with the variance $\mathrm{V}(\mathrm{T}_1(x))$ and the covariance $\mathrm{Cov}(\mathrm{T}_1(x)\mathrm{T}_1(y))$ are computed according to the scheme proposed in Section 6.1. The confidence interval associated with the variance $\mathrm{V}(\mathrm{T}_1(y))$ can finally be obtained analogously to that of $\mathrm{V}(\mathrm{T}_1(x))$.

6.2.4 The Variance of an Inhomogeneous Point Coordinate

Expanding a first order Taylor series for x around the coordinate means μ_u and μ_w gives:

$$x = \mathrm{T}_1(x) + \mathrm{R}_1(x), \tag{6.60}$$

with the first order Taylor approximation $\mathrm{T}_1(x)$ and the associated Lagrange remainder term $\mathrm{R}_1(x)$ being:

$$\begin{aligned}
\mathrm{T}_1(x) &= \frac{u}{w}\Big|_{\substack{u=\mu_u\\w=\mu_w}} + \begin{bmatrix} \frac{1}{w} & -\frac{u}{w^2} \end{bmatrix}\Big|_{\substack{u=\mu_u\\w=\mu_w}} \begin{bmatrix} u-\mu_u \\ w-\mu_w \end{bmatrix} \\
&= \frac{\mu_u}{\mu_w} + \frac{e_u}{\mu_w} - \frac{\mu_u e_w}{\mu_w^2}, \qquad (6.61)
\end{aligned}$$

$$\begin{aligned}
\mathrm{R}_1(x) &= \frac{1}{2}\begin{bmatrix} u-\mu_u & w-\mu_w \end{bmatrix} \begin{bmatrix} 0 & -\frac{1}{w^2} \\ -\frac{1}{w^2} & 2\frac{u}{w^3} \end{bmatrix}\Big|_{\substack{u=\xi_u\\w=\xi_w}} \begin{bmatrix} u-\mu_u \\ w-\mu_w \end{bmatrix} \\
&= -\frac{e_u e_w}{\xi_w^2} + \frac{\xi_u e_w^2}{\xi_w^3}. \qquad (6.62)
\end{aligned}$$

The variance of the first order Taylor approximation $\mathrm{T}_1(x)$ is computed as:

$$\mathrm{V}(\mathrm{T}_1(x)) = \mathrm{E}(\mathrm{T}_1(x)^2) - \mathrm{E}(\mathrm{T}_1(x))^2, \tag{6.63}$$

Thus, we calculate:

$$\begin{aligned}
\mathrm{E}(\mathrm{T}_1(x)) &= \frac{\mu_u}{\mu_w}, \qquad (6.64)\\
\mathrm{E}(\mathrm{T}_1(x))^2 &= \frac{\mu_u^2}{\mu_w^2}, \qquad (6.65)\\
\mathrm{E}(\mathrm{T}_1(x)^2) &= \frac{\mu_u^2}{\mu_w^2} + \frac{\sigma_u^2}{\mu_w^2} - 2\frac{\mu_u\sigma_{uw}}{\mu_w^3} + \frac{\mu_u^2\sigma_w^2}{\mu_w^4}, \qquad (6.66)
\end{aligned}$$

and finally obtain:

$$\begin{aligned}
\mathrm{V}(\mathrm{T}_1(x)) &= \frac{\sigma_u^2}{\mu_w^2} - 2\frac{\mu_u\sigma_{uw}}{\mu_w^3} + \frac{\mu_u^2\sigma_w^2}{\mu_w^4} \\
&= \frac{1}{\mu_w^4}\left(\mu_w^2\sigma_u^2 - 2\mu_u\mu_w\sigma_{uw} + \mu_u^2\sigma_w^2\right). \qquad (6.67)
\end{aligned}$$

As expected, this is perfectly equivalent to the result of first order error propagation given in Equation (6.59).

6.2.4.1 The Error in the First Order Estimate

In order to determine the error in estimating the variance σ_x^2 with $\mathrm{V}(\mathrm{T}_1(x))$, we compute the variance of the Lagrange remainder term $\mathrm{R}_1(x)$:

$$\mathrm{V}\left(\mathrm{R}_1(x)\right) = \mathrm{E}\left(\mathrm{R}_1(x)^2\right) - \mathrm{E}\left(\mathrm{R}_1(x)\right)^2. \tag{6.68}$$

The required expectation values are computed as:

$$\begin{aligned} \mathrm{E}\left(\mathrm{R}_1(x)\right) &= -\frac{\sigma_{uw}}{\xi_w^2} + \frac{\xi_u \sigma_w^2}{\xi_w^3}, \\ \mathrm{E}\left(\mathrm{R}_1(x)\right)^2 &= \frac{\sigma_{uw}^2}{\xi_w^4} - 2\frac{\xi_u \sigma_w^2 \sigma_{uw}}{\xi_w^5} + \frac{\xi_u^2 \sigma_w^4}{\xi_w^6}, \\ \mathrm{E}\left(\mathrm{R}_1(x)^2\right) &= \frac{\sigma_u^2 \sigma_w^2}{\xi_w^4} + 2\frac{\sigma_{uw}^2}{\xi_w^4} - 6\frac{\xi_u \sigma_w^2 \sigma_{uw}}{\xi_w^5} + 3\frac{\xi_u^2 \sigma_w^4}{\xi_w^6}. \end{aligned} \tag{6.69}$$

These results are obtained by application of the analytical definition of expectation values given in Equation (2.22). Thus, the variance of the Lagrange remainder term results to:

$$\begin{aligned} \mathrm{V}\left(\mathrm{R}_1(x)\right) &= \frac{\sigma_u^2 \sigma_w^2}{\xi_w^4} + \frac{\sigma_{uw}^2}{\xi_w^4} - 4\frac{\xi_u \sigma_w^2 \sigma_{uw}}{\xi_w^5} + 2\frac{\xi_u^2 \sigma_w^4}{\xi_w^6} \\ &= \frac{1}{\xi_w^6}\left(\xi_w^2\left(\sigma_u^2 \sigma_w^2 + \sigma_{uw}^2\right) - 4\xi_u \xi_w \sigma_w^2 \sigma_{uw} + 2\xi_u^2 \sigma_w^4\right). \end{aligned} \tag{6.70}$$

The confidence interval associated with $\mathrm{V}(\mathrm{T}_1(x))$ is obtained as the maximum value of $\mathrm{V}\left(\mathrm{R}_1(x)\right)$ concerning $\xi_u \in (u, \mu_u)$, and $\xi_w \in (w, \mu_w)$. As ξ_u solely appears in the numerator, the model $\xi_u = \mu_u + \alpha\sigma_u$ seems to be an appropriate choice. The other parameter, ξ_w, is dominant in the denominator of Equation (6.70). Thus, we choose the model $\xi_w = \mu_w - \alpha\sigma_w$ in order to obtain a maximum value of $\mathrm{V}\left(\mathrm{R}_1(x)\right)$.

Substituting these models, we obtain the confidence level associated with the variance of the first order Taylor approximation $\mathrm{T}_1(x)$ as:

$$b_{\mathrm{V}(\mathrm{T}_1(x))} = \frac{(\mu_w - \alpha\sigma_w)^2\left(\sigma_u^2 \sigma_w^2 + \sigma_{uw}^2\right) - 4(\mu_u + \alpha\sigma_u)(\mu_w - \alpha\sigma_w)\sigma_w^2 \sigma_{uw} + 2(\mu_u + \alpha\sigma_u)^2 \sigma_w^4}{(\mu_w - \alpha\sigma_w)^6}. \tag{6.71}$$

Therein, the factor $\alpha = \{1, 2, 3\}$ specifies the level of significance associated with the confidence interval.

In order to define a relative confidence interval, we relate $b_{\mathrm{V}(\mathrm{T}_1(x))}$ to the variance $\mathrm{V}(\mathrm{T}_1(x))$ and obtain:

$$b_{\mathrm{V}(\mathrm{T}_1(x)),r} = \frac{\mu_w^4\left((\mu_w - \alpha\sigma_w)^2\left(\sigma_u^2 \sigma_w^2 + \sigma_{uw}^2\right) - 4(\mu_u + \alpha\sigma_u)(\mu_w - \alpha\sigma_w)\sigma_w^2 \sigma_{uw} + 2(\mu_u + \alpha\sigma_u)^2 \sigma_w^4\right)}{(\mu_w - \alpha\sigma_w)^6\left(\mu_w^2 \sigma_u^2 - 2\mu_u \mu_w \sigma_{uw} + \mu_u^2 \sigma_w^2\right)}. \tag{6.72}$$

6.2.5 The Covariance of two Inhomogeneous Point Coordinates

The first order estimations for the inhomogeneous point coordinates x and y are (cf. Equation (6.61)) given as:

$$\mathrm{T}_1(x) = \frac{\mu_u}{\mu_w} + \frac{e_u}{\mu_w} - \frac{\mu_u e_w}{\mu_w^2}, \tag{6.73}$$

$$\mathrm{T}_1(y) = \frac{\mu_v}{\mu_w} + \frac{e_v}{\mu_w} - \frac{\mu_v e_w}{\mu_w^2}. \tag{6.74}$$

The related expectation values are:

$$\mathrm{E}(\mathrm{T}_1(x)) = \frac{\mu_u}{\mu_w}, \tag{6.75}$$

$$\mathrm{E}(\mathrm{T}_1(y)) = \frac{\mu_v}{\mu_w}. \tag{6.76}$$

In order to derive an algebraic expression for the covariance between the two first order estimates, we compute the following expressions utilizing the terms listed in Table 6.2:

$$\mathrm{E}(\mathrm{T}_1(x))\mathrm{E}(\mathrm{T}_1(y)) = \frac{\mu_u\mu_v}{\mu_w^2}, \tag{6.77}$$

$$\mathrm{E}(\mathrm{T}_1(x)\mathrm{T}_1(y)) = \frac{\mu_u\mu_v}{\mu_w^2} + \frac{\sigma_{uv}}{\mu_w^2} - \frac{\mu_u\sigma_{vw}}{\mu_w^3} - \frac{\mu_v\sigma_{uw}}{\mu_w^3} + \frac{\mu_u\mu_v\sigma_w^2}{\mu_w^4}. \tag{6.78}$$

Thus, the first order estimation for the covariance σ_{xy} results to:

$$\begin{aligned}\mathrm{Cov}(\mathrm{T}_1(x), \mathrm{T}_1(y)) &= \mathrm{E}\left(\mathrm{T}_1(x)\mathrm{T}_1(y)\right) - \mathrm{E}(\mathrm{T}_1(x))\mathrm{E}(\mathrm{T}_1(y)) \\ &= \frac{\sigma_{uv}}{\mu_w^2} - \frac{\mu_u\sigma_{vw}}{\mu_w^3} - \frac{\mu_v\sigma_{uw}}{\mu_w^3} + \frac{\mu_u\mu_v\sigma_w^2}{\mu_w^4} \\ &= \frac{1}{\mu_w^4}\left(\mu_w^2\sigma_{uv} - \mu_w(\mu_u\sigma_{vw} + \mu_v\sigma_{uw}) + \mu_u\mu_v\sigma_w^2\right). \end{aligned} \tag{6.79}$$

As expected, this expression is perfectly equivalent to the result of first order error propagation given in Equation (6.59).

6.2.5.1 The Error in the First Order Estimate

In order to determine the error in estimating the covariance σ_{xy} with $\mathrm{Cov}(\mathrm{T}_1(x), \mathrm{T}_1(y))$, we need to compute:

$$\mathrm{Cov}(\mathrm{R}_1(x), \mathrm{R}_1(y)) = \mathrm{E}\left(\mathrm{R}_1(x)\mathrm{R}_1(y)\right) - \mathrm{E}\left(\mathrm{R}_1(x)\right)\mathrm{E}\left(\mathrm{R}_1(y)\right), \tag{6.80}$$

with the Lagrange remainder terms (cf. Equation (6.62)) being:

$$\mathrm{R}_1(x) = -\frac{e_u e_w}{\xi_w^2} + \frac{\xi_u e_w^2}{\xi_w^3}, \tag{6.81}$$

$$\mathrm{R}_1(y) = -\frac{e_v e_w}{\xi_w^2} + \frac{\xi_v e_w^2}{\xi_w^3}. \tag{6.82}$$

The required expectation values are computed utilizing the terms listed in Table 6.2:

$$\mathrm{E}\left(\mathrm{R}_1(x)\right) = -\frac{\sigma_{uw}}{\xi_w^2} + \frac{\xi_u\sigma_w^2}{\xi_w^3}, \tag{6.83}$$

$$\mathrm{E}\left(\mathrm{R}_1(y)\right) = -\frac{\sigma_{vw}}{\xi_w^2} + \frac{\xi_v\sigma_w^2}{\xi_w^3}, \tag{6.84}$$

$$\mathrm{E}\left(\mathrm{R}_1(x)\right)\mathrm{E}\left(\mathrm{R}_1(y)\right) = \frac{\sigma_{uw}\sigma_{vw}}{\xi_w^4} - \frac{\xi_u\sigma_w^2\sigma_{vw}}{\xi_w^5} - \frac{\xi_v\sigma_w^2\sigma_{uw}}{\xi_w^5} + \frac{\xi_u\xi_v\sigma_w^4}{\xi_w^6}, \tag{6.85}$$

$$\mathrm{E}\left(\mathrm{R}_1(x)\mathrm{R}_1(y)\right) = \frac{\sigma_w^2\sigma_{uv}}{\xi_w^4} + 2\frac{\sigma_{uw}\sigma_{vw}}{\xi_w^4} - 3\frac{\xi_u\sigma_w^2\sigma_{vw}}{\xi_w^5} - 3\frac{\xi_v\sigma_w^2\sigma_{uw}}{\xi_w^5} + 3\frac{\xi_u\xi_v\sigma_w^4}{\xi_w^6}. \tag{6.86}$$

Thus, the covariance of the two Lagrange remainder terms results to:

$$\begin{aligned}\mathrm{Cov}(\mathrm{R}_1(x), \mathrm{R}_1(y)) = \\ &= \frac{\sigma_w^2\sigma_{uv}}{\xi_w^4} + \frac{\sigma_{uw}\sigma_{vw}}{\xi_w^4} - 2\frac{\xi_u\sigma_w^2\sigma_{vw}}{\xi_w^5} - 2\frac{\xi_v\sigma_w^2\sigma_{uw}}{\xi_w^5} + 2\frac{\xi_u\xi_v\sigma_w^4}{\xi_w^6} \\ &= \frac{1}{\xi_w^6}\left(\xi_w^2\left(\sigma_w^2\sigma_{uv} + \sigma_{uw}\sigma_{vw}\right) - 2\xi_w\left(\xi_u\sigma_w^2\sigma_{vw} + \xi_v\sigma_w^2\sigma_{uw}\right) + 2\xi_u\xi_v\sigma_w^4\right). \quad (6.87)\end{aligned}$$

The confidence interval associated with $\mathrm{Cov}(\mathrm{T}_1(x)\mathrm{T}_1(y))$ is obtained as the maximum value of $\mathrm{Cov}(\mathrm{R}_1(x), \mathrm{R}_1(y))$ concerning $\xi_u \in (u, \mu_u)$, $\xi_v \in (v, \mu_v)$, and $\xi_w \in (w, \mu_w)$. As ξ_u and ξ_v solely appear in the numerator of $\mathrm{Cov}(\mathrm{R}_1(x), \mathrm{R}_1(y))$, the values $\xi_u = \mu_u + \alpha\sigma_u$, $\xi_v = \mu_v + \alpha\sigma_v$ are chosen. The third parameter, ξ_w, is dominant in the denominator of Equation (6.87), thus we choose the model $\xi_w = \mu_w - \alpha\sigma_w$.

After substitution of ξ_u, ξ_v and ξ_w into Equation (6.87), we obtain the absolute confidence level associated with the covariance between the two first order Taylor approximations $\mathrm{T}_1(x)$ and $\mathrm{T}_1(y)$ as:

$$\begin{aligned}b_{\mathrm{Cov}(\mathrm{T}_1(x)\mathrm{T}_1(y))} = \frac{1}{(\mu_w - \alpha\sigma_w)^6}&\left((\mu_w - \alpha\sigma_w)^2\left(\sigma_w^2\sigma_{uv} + \sigma_{uw}\sigma_{vw}\right)\right. \\ &- 2\left(\mu_w - \alpha\sigma_w\right)\left(\left(\mu_u - \alpha\sigma_u\right)\sigma_w^2\sigma_{vw} + \left(\mu_v - \alpha\sigma_v\right)\sigma_w^2\sigma_{uw}\right) \\ &\left. + 2\left(\mu_u - \alpha\sigma_u\right)\left(\mu_v - \alpha\sigma_v\right)\sigma_w^4\right). \quad (6.88)\end{aligned}$$

Therein, the factor $\alpha = \{1, 2, 3\}$ specifies the level of significance associated with the absolute confidence interval. In order to define a relative confidence interval, we can compute:

$$b_{\mathrm{Cov}(\mathrm{T}_1(x)\mathrm{T}_1(y)),r} = \frac{b_{\mathrm{Cov}(\mathrm{T}_1(x)\mathrm{T}_1(y))}}{\mathrm{Cov}(\mathrm{T}_1(x)\mathrm{T}_1(y))}. \quad (6.89)$$

As the resulting term $b_{\mathrm{Cov}(\mathrm{T}_1(x)\mathrm{T}_1(y)),r}$ is a lengthy expression, it is not listed here explicitly.

6.2.6 Numerical Verification

A set of data points consisting of 10^6 samples with homogeneous coordinate vectors was randomly generated (cf. Section 2.3.2) based on a Gaussian probability density function with coordinate mean vector:

$$\boldsymbol{\mu}_{uvw} = \begin{bmatrix} \mu_u \\ \mu_v \\ \mu_w \end{bmatrix} = \begin{bmatrix} 10 \\ 12 \\ 8 \end{bmatrix}, \tag{6.90}$$

and covariance matrix:

$$\boldsymbol{\Lambda}_{uvw} = \begin{bmatrix} 0.5 & 0.05 & 0.05 \\ 0.05 & 0.5 & 0.05 \\ 0.05 & 0.05 & 0.5 \end{bmatrix}. \tag{6.91}$$

Note that in this example, units were omitted as they are not significant for the interpretation of the results.

At first, the inhomogeneous point coordinates x and y were calculated for all of the samples. Furthermore, the mean coordinate vector $\boldsymbol{\mu}_{xy}$ as well as the covariance matrix $\boldsymbol{\Lambda}_{xy}$ of the inhomogeneous point coordinates were determined.

Subsequently, the first order estimations of the inhomogeneous point coordinates $\mathrm{T}_1(x)$ and $\mathrm{T}_1(y)$ were calculated together with the variances $\mathrm{V}(\mathrm{T}_1(x))$ and $\mathrm{V}(\mathrm{T}_1(y))$ (cf. Equation (6.67)) as well as the covariance $\mathrm{Cov}(\mathrm{T}_1(x)\mathrm{T}_1(y))$ (cf. Equation (6.79)). Finally, the absolute confidence intervals $b_{\mathrm{V}(\mathrm{T}_1(x))}$, $b_{\mathrm{V}(\mathrm{T}_1(y))}$ and $b_{\mathrm{Cov}(\mathrm{T}_1(x)\mathrm{T}_1(y))}$ as well as the relative confidence intervals $b_{\mathrm{V}(\mathrm{T}_1(x)),r}$, $b_{\mathrm{V}(\mathrm{T}_1(y)),r}$ and $b_{\mathrm{Cov}(\mathrm{T}_1(x)\mathrm{T}_1(y)),r}$ were computed with a significance level specified by $\alpha = 3$.

Table 6.4 gives a summary of the results obtained. Therein, $\boldsymbol{\Lambda}_{\mathrm{T}_1(x)\mathrm{T}_1(y)}$ terms the covariance matrix of the first order estimates $\mathrm{T}_1(x)$ and $\mathrm{T}_1(y)$, i.e.:

$$\boldsymbol{\Lambda}_{\mathrm{T}_1(x)\mathrm{T}_1(y)} = \begin{bmatrix} \mathrm{V}(\mathrm{T}_1(x)) & \mathrm{Cov}(\mathrm{T}_1(x)\mathrm{T}_1(y)) \\ \mathrm{Cov}(\mathrm{T}_1(x)\mathrm{T}_1(y)) & \mathrm{V}(\mathrm{T}_1(y)) \end{bmatrix}, \tag{6.92}$$

$\mathsf{B}_{\mathrm{T}_1(x)\mathrm{T}_1(y)}$ denotes the matrix of absolute confidence intervals:

$$\mathsf{B}_{\mathrm{T}_1(x)\mathrm{T}_1(y)} = \begin{bmatrix} b_{\mathrm{V}(\mathrm{T}_1(x))} & b_{\mathrm{Cov}(\mathrm{T}_1(x)\mathrm{T}_1(y))} \\ b_{\mathrm{Cov}(\mathrm{T}_1(x)\mathrm{T}_1(y))} & b_{\mathrm{V}(\mathrm{T}_1(y))} \end{bmatrix}, \tag{6.93}$$

and $\mathsf{B}_{\mathrm{T}_1(x)\mathrm{T}_1(y),r}$ holds the relative confidence intervals:

$$\mathsf{B}_{\mathrm{T}_1(x)\mathrm{T}_1(y),r} = \begin{bmatrix} b_{\mathrm{V}(\mathrm{T}_1(x)),r} & b_{\mathrm{Cov}(\mathrm{T}_1(x)\mathrm{T}_1(y)),r} \\ b_{\mathrm{Cov}(\mathrm{T}_1(x)\mathrm{T}_1(y)),r} & b_{\mathrm{V}(\mathrm{T}_1(y)),r} \end{bmatrix}. \tag{6.94}$$

$\boldsymbol{\mu}_{xy}$	Λ_{xy}	$\Lambda_{\mathrm{T}_1(x)\mathrm{T}_1(y)}$
$\begin{bmatrix} 1.2540 \\ 1.5049 \end{bmatrix}$	$\begin{bmatrix} 0.0082 & 0.0061 \\ 0.0061 & 0.0106 \end{bmatrix}$	$\begin{bmatrix} 0.0080 & 0.0059 \\ 0.0059 & 0.0103 \end{bmatrix}$

$\lvert\Lambda_{xy} - \Lambda_{\mathrm{T}_1(x)\mathrm{T}_1(y)}\rvert$	$\mathsf{B}_{\mathrm{T}_1(x)\mathrm{T}_1(y)}$	$\mathsf{B}_{\mathrm{T}_1(x)\mathrm{T}_1(y),r}$
$\begin{bmatrix} 0.19\ 10^{-3} & 0.18\ 10^{-3} \\ 0.18\ 10^{-3} & 0.26\ 10^{-3} \end{bmatrix}$	$\begin{bmatrix} 0.21\ 10^{-3} & 0.21\ 10^{-3} \\ 0.21\ 10^{-3} & 0.28\ 10^{-3} \end{bmatrix}$	$\begin{bmatrix} 2.55\% & 3.55\% \\ 3.55\% & 2.70\% \end{bmatrix}$

Table 6.4: Results of a Monte-Carlo experiment concerning the absolute and relative confidence intervals associated with the covariance matrix of first order estimates of inhomogeneous point coordinates $\mathrm{T}_1(x)$ and $\mathrm{T}_1(y)$.

As can be seen, the elements of the matrix $|\Lambda_{xy} - \Lambda_{\mathrm{T}_1(x)\mathrm{T}_1(y)}|$, which specify the absolute differences of the "true" covariance matrix and its first order estimate, are all within the absolute confidence intervals specified in $\mathsf{B}_{\mathrm{T}_1(x)\mathrm{T}_1(y)}$.

6.3 Summary

In this chapter, a procedure for determination of a confidence interval associated with the results of first order error propagation applied to non-linear functions $\boldsymbol{f}(\boldsymbol{x})$ was presented. The approach is based on first order Taylor series expansions of the examined functions $\boldsymbol{f}(\boldsymbol{x})$ around the mean values of the uncertain input data vector $\boldsymbol{x}$. The confidence interval being sought is computed as the variance of the Lagrange remainder term associated with the first order Taylor series.

The applicability of the procedure was outlined by means of two tasks typically arising in metric vision applications, namely:

- calculation of the Euclidean distance between two uncertain data points, and
- computation of the inhomogeneous coordinates of an uncertain data point, given the set of homogeneous point coordinates.

The results of these computations were numerically verified with Monte-Carlo experiments.

Part III

Application and Conclusion

Chapter 7

A Video-Extensometer System for Tensile Testing of Polymer Materials

This chapter deals with a digital image processing system to measure polymer materials during tensile testing. In the following, this measurement system will be referred to as video-extensometer system. Tensile properties are determined by applying a longitudinal force to the sample under test and measuring the resulting deformation of the specimen. This deformation is truly 3-dimensional, a longitudinal elongation and a shortening of the material in both dimensions orthogonal to the longitudinal axis.

The motivation for this work has arisen from the need for contactless methods for the measurement of polymer materials during tensile testing. Mechanical extensometer systems influence the characteristics of polymer materials or require extensive specimen instrumentation (e.g. strain gauges). Furthermore, they are incapable of measuring the true 3-dimensional specimen deformation. As a consequence, contact-free measurement approaches are desirable. In this connection, video-extensometer systems as well as laser extensometer systems are commonly applied to measure global tensile properties. In contrast to these two types, digital image correlation systems [3, 1] as well as laser speckle extensometers [6, 3, 1] are utilized to measure full-field deformations.

The measurement principle of laser extensometer systems, see e.g. [2, 14], is based on the diverse reflectivity of the specimen surface and the measurement marks applied to the material. These systems are inflexible compared to video-extensometer systems with respect to the diversity of evaluation possibilities at measurements on modern testing machines. The aim here was to develop a digital image processing system to measure the full 3-dimensional deformation of the samples under test. A flexible system with respect to the application on different types of specimen and material properties (e.g. reflectivity, colour, transparency) was established.

At first, the hardware setup is described together with three different acquisition configurations that can be realized with the hardware components. Subsequently, the image processing algorithm utilized to evaluate the images acquired during the tensile tests are discussed. Finally, statistical uncertainty analyses are presented, which address the extraction of the data points as well as the particular steps of the evaluation algorithms.

7.1 Image Acquisition Setup and Configurations

A schematic diagram for the hardware setup of the presented video-extensometer system is shown in Figure 7.1. The sample under test is uniaxially loaded in a universal testing machine. During the tests, image sequences are acquired with the industrial cameras mounted in front of the specimen. The system is designed to support simultaneous image acquisition of up to three monochrome cameras operating at up to 30Hz. Depending on the specific measurement task, the cameras can be arranged in a number of different configurations.

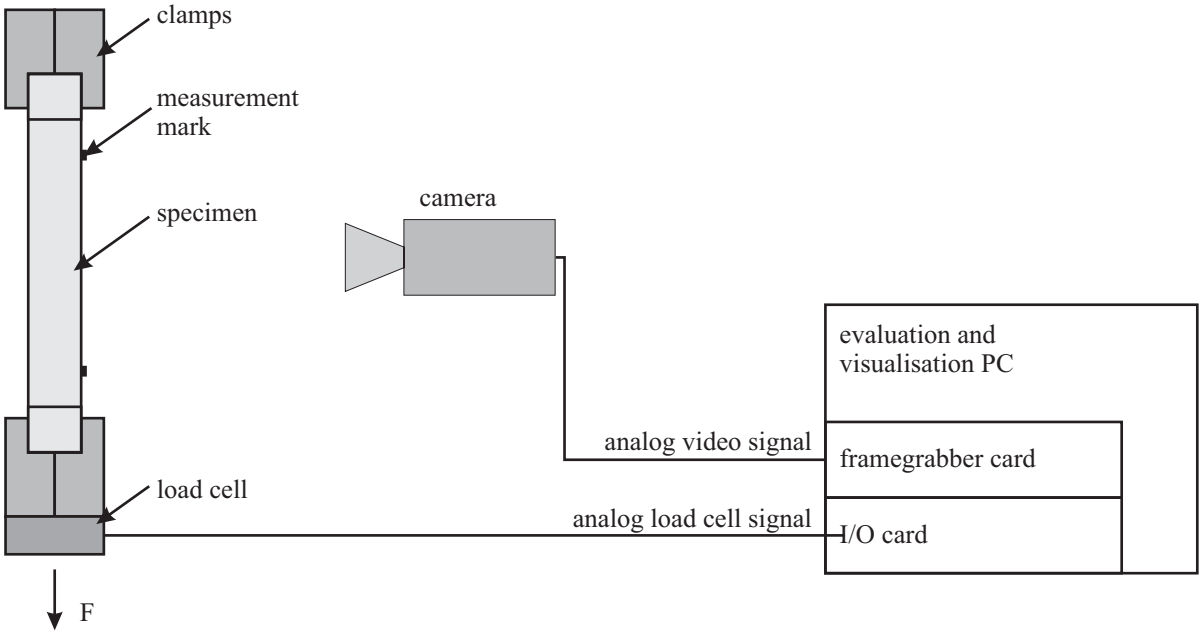

Figure 7.1: Scheme of the hardware setup realized with the video-extensometer system. The shape of the specimens typically used for tensile tests follows the ISO 527−2 standard and exhibits an initial rectangular cross-section of $10 \times 4mm^2$.

The images are captured by means of a framegrabber card located in a standard measurement PC, which additionally holds an I/O card to record the analogue output signal of the testing machine's load cell. The acquired images are evaluated offline, whereas the resulting deformation data is subsequently synchronized with the acquired load cell signal.

In the presented video-extensometer system, images are captured with *Sony XC-HR* 70[1] analogue monochrome cameras and a *Matrox Meteor 2 Multichannel*[2] analogue framegrabber card. The cameras are equipped with *Rodenstock MeVis*[3] precision lenses with focal length of 25mm or 50mm, depending on the specific measurement task. The signal from the load cell is acquired by means of a *National Instruments NI PCI-6036E*[4] I/O card.

The particular components of the measurement hardware are properties of the *Polymer*

[1] www.sonybiz.net
[2] www.matrox.com/imaging
[3] www.rodenstock.com
[4] www.ni.com

Competence Center Leoben GmbH[5] (PCCL). The system is installed at a universal testing machine of type *Instron* 4505, which belongs to the *Institute of Materials Science and Testing of Plastics*[6] at the *University of Leoben*[7]. The development work for the video-extensometer system has been accomplished at the PCCL within the strategic project S7. For further information about this project, the interested reader is referred to the corresponding work package report [19].

7.1.1 Acquisition Configurations

The video-extensometer system supports simultaneous image acquisition from up to three camera systems. These can be arranged in a number of ways in order to meet the requirements of the specific measurement task. In Figure 7.2, three different acquisition configurations are schematically visualized. There, the fields of view of the utilized camera systems are depicted with respect to a specimen, whose shape follows the ISO $527 - 2$ standard. These standardized specimens are typically used for tensile tests and exhibit an initial rectangular cross-section of $10 \times 4mm^2$. The initial measurement length is realized by means of measurement marks, which are applied to the samples by coloring the front face approximately orthogonal to the longitudinal axis, and commonly amounts to 40mm or 50mm, respectively.

Figure 7.2(a) shows the *standard* configuration with one camera focussing on the front face of the specimen. A *high-resolution* configuration is depicted in Figure 7.2(b), where two cameras observe local regions around the measurement marks applied to the specimen. As a consequence of the smaller field of view, the optical resolution is increased in comparison to the *standard* configuration.

However, a calibration procedure is required to determine the relative location of the camera systems. Both, the *standard* and the *high-resolution* configurations, enable the determination of the axial as well as the primary transversal deformation of the specimen. Figure 7.2(c) finally extends the *high-resolution* configuration by a third camera system which focusses on the second transversal dimension using an optical mirror mounted laterally to the specimen.

The 3-dimensional acquisition configuration depicted in Figure 7.2(c) enables the determination of the volumetric specimen deformation. However, the algorithm for computing the two transversal deformations are identical, the only difference is that they apply on different sets of data points. Thus, the subsequent considerations solely relate to the *standard* and the *high-resolution* configuration. For further information about the 3-dimensional setup, the interested reader is referred to a corresponding publication of the author [18].

[5] http://www.pccl.at
[6] http://www.iwpk.at
[7] http://www.unileoben.ac.at

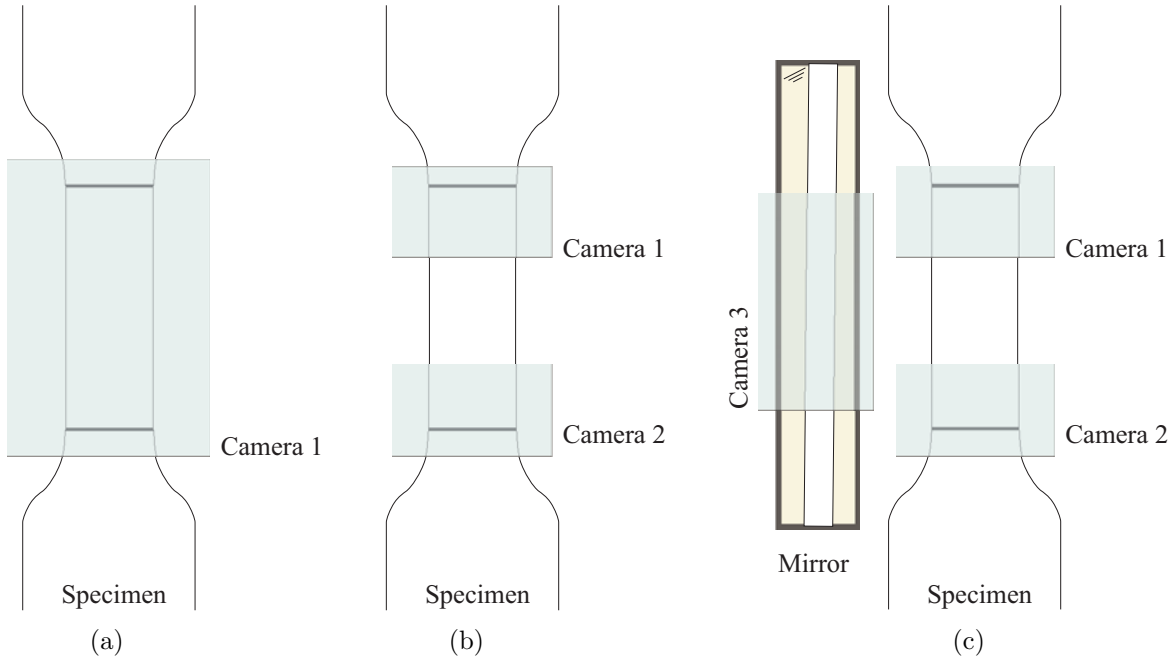

Figure 7.2: Fields of view of the cameras with respect to the specimen for (a) the standard, (b) the high-resolution, and (c) the 3-dimensional acquisition configuration. Note that in the configurations (b) and (c), two cameras are focussing on local regions around the measurement marks. As the testing machine's lower crosshead is moved downwards during the tensile testing, these fields of view are centered at points below the respective measurement marks.

7.2 Evaluation Algorithm

The sequence images acquired during the tensile testing are evaluated offline and independently of one another, whereby the evaluation algorithm for a particular image is subdivided into the following tasks:

1. determine the location of the sets of data points in the images,
2. (optional) rectification of the data points from an image coordinate system to a metric coordinate frame,
3. fitting of geometric models to the sets of data points, and
4. computation of the actual specimen dimensions.

Given the measured specimen dimensions, the longitudinal and transversal strain characteristics can be derived. Strain values are dimensionless by definition. Thus, they can be computed from specimen dimensions specified by arbitrary units of measurement, i.e. pixel units as well as metric measures.

Assuming the camera's optical axis being oriented perfectly orthogonal to the front face of the specimen. This is the situation, where any measure determined within the image coordinate system (in pixel units) can be transformed by simple multiplication with a constant factor (the pixel resolution) to a metric measure with respect to a coordinate frame on the specimen's front face.

In the *standard* setup, the camera is mounted such as to realize this design. As a result, the longitudinal and transversal strain characteristics can be directly calculated out of the measured specimen dimensions. Thus, rectification of the data points is an optional task for measurements in the *standard* configuration.

7.2.1 Extracting the Sets of Data Points

Referring to Figure 7.3 and 7.4, six sets of data points, which are termed as $S_1, \ldots, S_6$, are extracted at the specimen edges and the margins of the measurement marks, respectively.

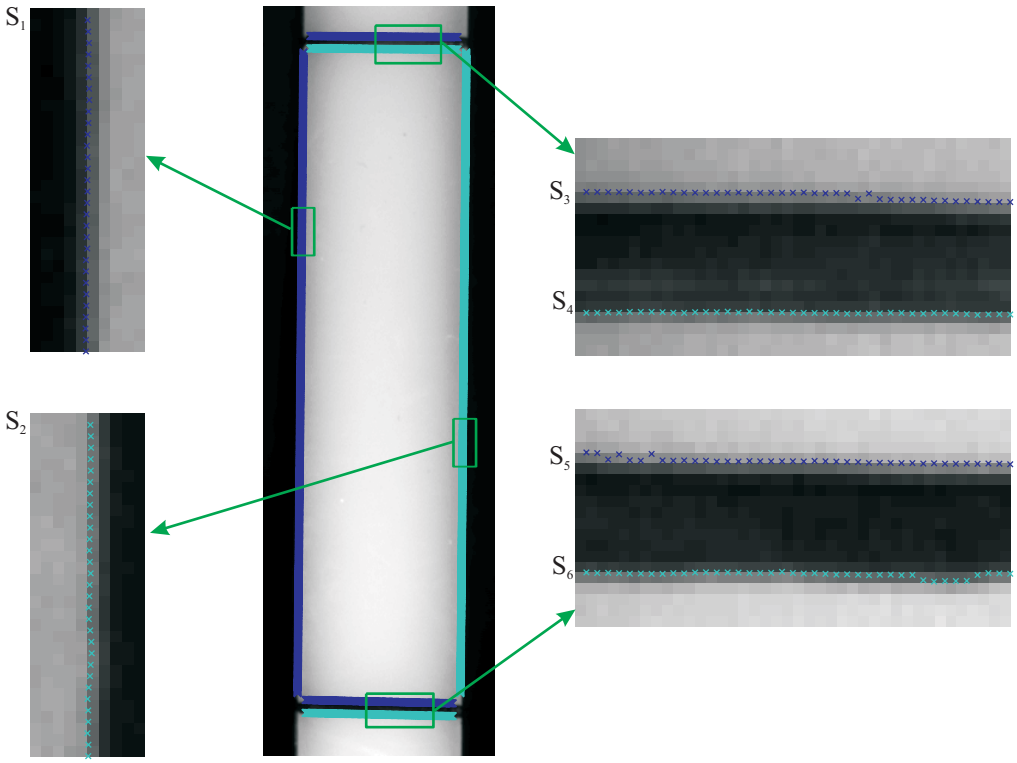

Figure 7.3: Sample image captured under the *standard* acquisition configuration. The location of the sets of data points is emphasized in magnified local image regions.

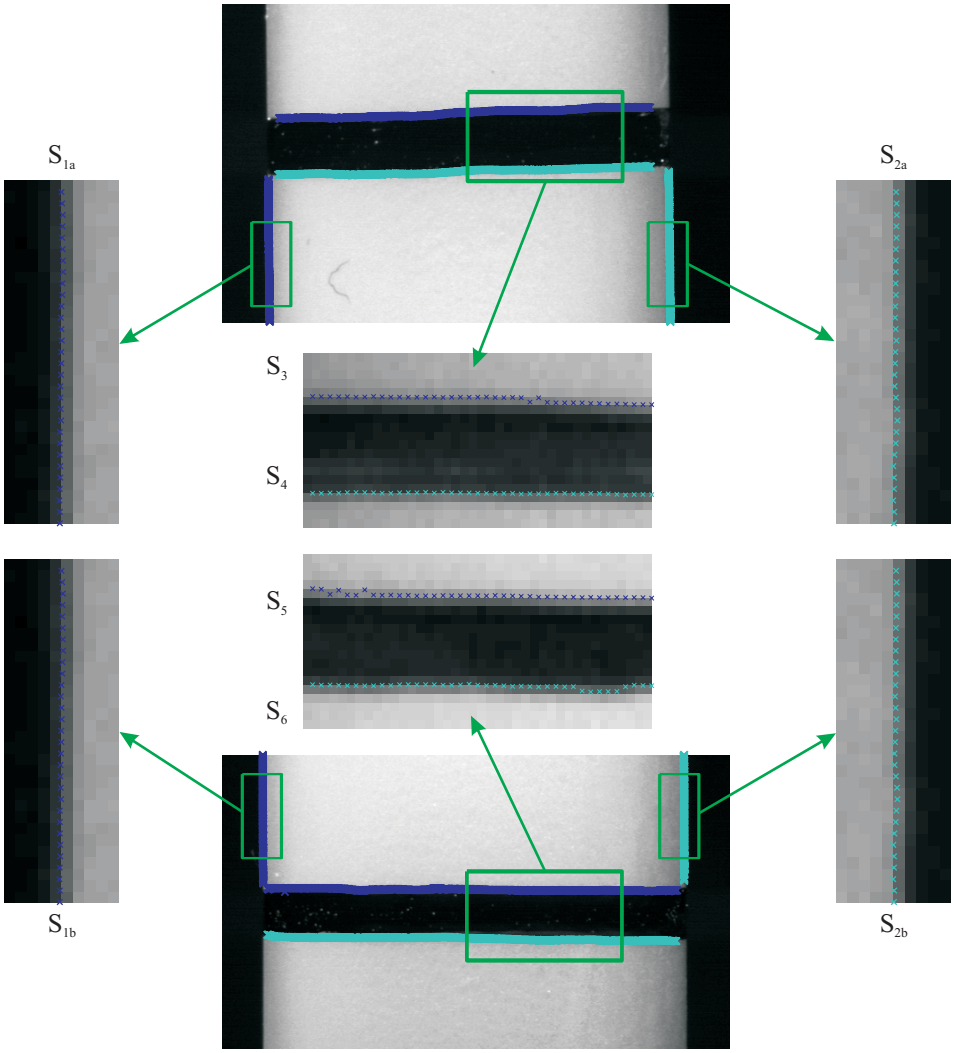

Figure 7.4: Sample images captured under the *high-resolution* acquisition configuration. The location of the sets of data points is emphasized in magnified local image regions. The fields of view of the two cameras are non-overlapping, thus a calibration procedure is required to determine their relative location.

For each of the particular images $I(x, y)$ acquired during the tensile testing, the location of the data points is determined according to the following procedure:

1. Computation of the image of absolute gradient $G(x, y)$:

$$G(x,y) = \sqrt{\left(\frac{\delta I(x,y)}{\delta x}\right)^2 + \left(\frac{\delta I(x,y)}{\delta y}\right)^2} \tag{7.1}$$

2. Extraction of the location (g_x, g_y) of maximum absolute gradient along each pixel row (for the data points at the specimen edges) and each pixel column (for the data points at the margins of the measurement marks), respectively.

3. Computation of the 2-dimensional center-of-gravity (c_x, c_y) of the gradient within a $(2s_x + 1) \times (2s_y + 1)$ image window centered at (g_x, g_y),

$$c_x = \frac{\sum_{x=g_x-s_x}^{g_x+s_x} \sum_{y=g_y-s_y}^{g_y+s_y} xG(x,y)^p}{\sum_{x=g_x-s_x}^{g_x+s_x} \sum_{y=g_y-s_y}^{g_y+s_y} G(x,y)^p}, \quad c_y = \frac{\sum_{x=g_x-s_x}^{g_x+s_x} \sum_{y=g_y-s_y}^{g_y+s_y} yG(x,y)^p}{\sum_{x=g_x-s_x}^{g_x+s_x} \sum_{y=g_y-s_y}^{g_y+s_y} G(x,y)^p}. \tag{7.2}$$

Therein, the exponent p is utilized to incorporate stronger weighting of pixels with high absolute image gradient, [43]. This procedure enables the computation of the point positions with sub-pixel accuracy. Moreover, the procedure is applicable for arbitrary specimen colour, whereas the colour of the measurement marks as well as that of the image background should be chosen to realize high image contrast.

7.2.2 Rectification of the Data Points

The homogeneous coordinate vector of a data point $\boldsymbol{p}_I$, given with respect to an image coordinate frame, is projectively transformed to a coordinate vector $\boldsymbol{p}_M$ of a planar metric coordinate system according to:

$$\boldsymbol{p}_M = \mathsf{H}\boldsymbol{p}_I. \tag{7.3}$$

Therein, the 3×3 homography matrix H describes the projective transformation of the camera's image plane to a planar, metric coordinate frame. The parameters of the homography matrix are determined in a preceding calibration process, which makes use of the DLT algorithm as described in Section 5.1.1.

A calibration target, which is depicted in Figure 7.5(a), is utilized for the calibration procedure. The target is equipped with a rectangular grid of reference bores, each of 1.5mm in diameter. The center point distances between adjacent reference bores are 4mm in each direction.

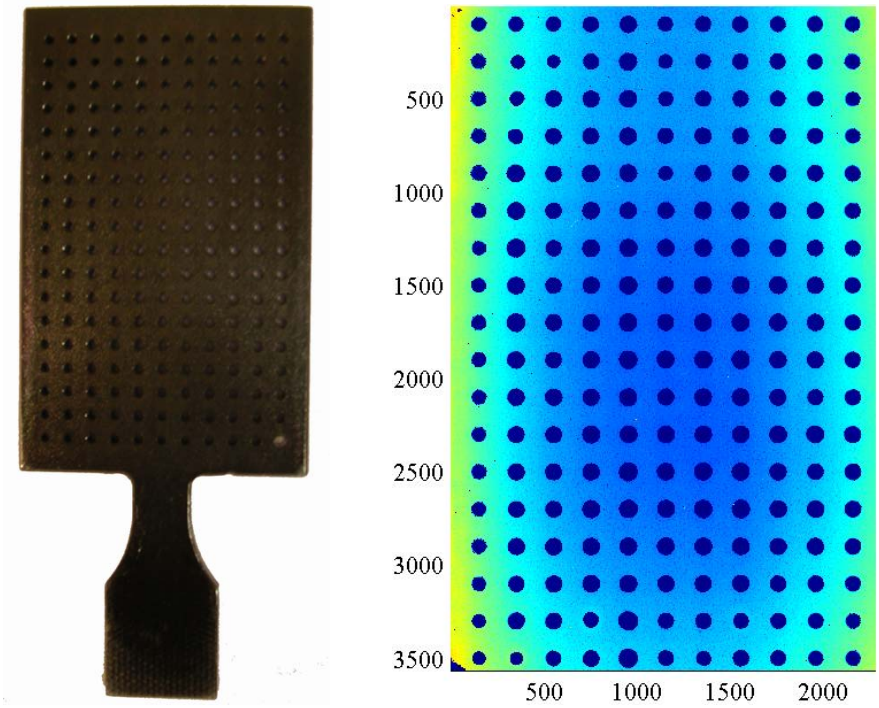

(a) (b)

Figure 7.5: The calibration target (a) utilized to determine the homography matrix, which maps points of the camera's image plane to the front face of the target. The height distribution of the front face was measured by means of a confocal microscope (b). This data provides the starting point to determine the metric coordinates of the reference bore's center points.

Prior to the calibration process, the center point coordinates of the reference bores were determined with respect to a planar, metric coordinate frame, which is located on the front face of the target. The center point coordinates were found by means of the following procedure:

- At first, the height distribution of the calibration target's front surface was measured with a confocal microscope[8] at a raster of 3500×2300 points (see Figure 7.5(b)). The distance between adjacent points of the raster was $20\mu m$ in each direction.
- By application of a contour extraction algorithm, data points at the circumference of the bores were determined.
- Finally, circular models were approximated to the data points of the particular contour objects, which directly lead to the center point coordinates of the bores.

During the calibration process, the metric center point coordinates are assigned to the image coordinates of center points extracted in the calibration images. Subsequently, the DLT algorithm is executed on the resulting pairs of corresponding points.

[8] A device of the *Fries Research & Technology GmbH* (http://www.frt-gmbh.com) was used.

7.2.3 Computation of the Specimen Dimensions

Given the sets of data points, three pairs of parallel lines are determined:

1. The lines $\boldsymbol{l}_L$ and $\boldsymbol{l}_R$ corresponding to the left and right edges of the specimen, respectively.
2. Two lines representing the upper and lower margins of the upper measurement mark.
3. Two lines representing the upper and lower margins of the lower measurement mark.

Subsequently, the parameters of three lines $\boldsymbol{l}_C$, $\boldsymbol{l}_T$, and $\boldsymbol{l}_B$ are calculated: $\boldsymbol{l}_C$ denotes a line central to the pair of parallel lines $\boldsymbol{l}_L$ and $\boldsymbol{l}_R$; $\boldsymbol{l}_T$ and $\boldsymbol{l}_B$ denote lines central to the pairs of parallel lines at the margins of the upper and lower measurement mark, respectively.

Finally, the coordinate vectors of two intersection points, $\boldsymbol{p}_T$ and $\boldsymbol{p}_B$, are computed by intersecting $\boldsymbol{l}_C$ with $\boldsymbol{l}_T$, and $\boldsymbol{l}_C$ with $\boldsymbol{l}_B$, respectively. Figure 7.6 illustrates all of the named geometric primitives with respect to magnified image regions around the measurement marks. The longitudinal specimen dimension is calculated as the Euclidean distance between the two points of intersection, $\boldsymbol{p}_T$ and $\boldsymbol{p}_B$, the transversal dimension is computed as the orthogonal distance between the two parallel lines $\boldsymbol{l}_L$ and $\boldsymbol{l}_R$.

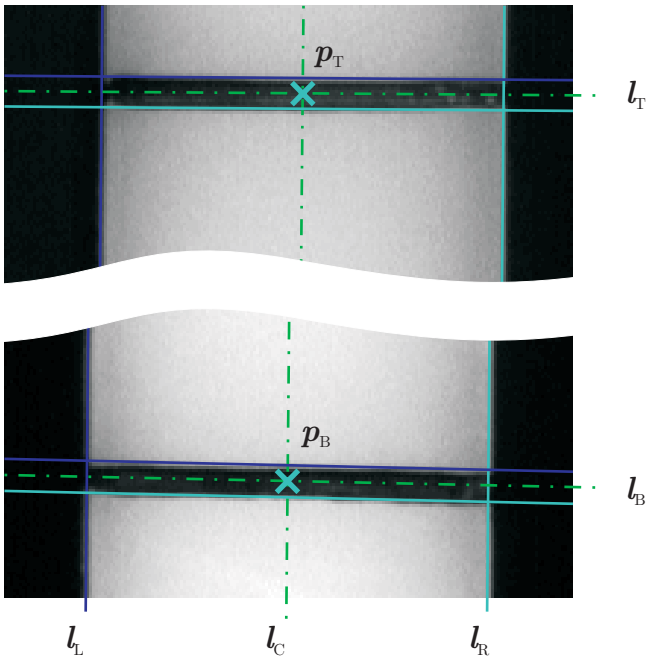

Figure 7.6: Location of the geometric primitives utilized for the evaluation procedure: Three pairs of parallel lines fitted to the sets of data points together with their corresponding central lines, $\boldsymbol{l}_C$, $\boldsymbol{l}_T$ and $\boldsymbol{l}_B$, and the two points of intersection $\boldsymbol{p}_T$ and $\boldsymbol{p}_B$.

As a result of evaluating the particular images acquired during a tensile test, the longitudinal and transversal specimen dimensions, l_i and w_i, $i = 1 \ldots n_I$, are obtained. Therein, n_I denotes the number of images being evaluated.

7.2.4 Derivation of the Strain Characteristics

In order to compute the longitudinal strain values, ε_{l_i}, as well as the transversal strain values, ε_{w_i}, $i = 1 \dots n_I$, the measured longitudinal and transversal specimen dimensions are related to the initial specimen dimensions:

$$\varepsilon_{l_i} = \frac{l_i - l_0}{l_0}, \qquad \varepsilon_{w_i} = -\frac{w_i - w_0}{w_0}. \tag{7.4}$$

Therein, l_0 and w_0 denote the initial longitudinal and transversal specimen dimensions, which are determined from images acquired prior to the start of the tensile tests.

7.2.5 Exemplary Measurement Results

A typical result obtained with the video-extensometer system is shown in Figure 7.7. Therein, the plots of the longitudinal and transversal strain characteristics as well as the tensile force applied to the sample under test are presented with respect to the measurement time. Note that the force values are scaled to fit the data range of the strain characteristics. The plots show real measurement data, i.e. no filtering has been performed. The measured data can be seen as the starting point for further investigations, as for instance the computation of Poisson's ratio, the derivation of the stress-strain diagram or the calculation of the yield point. However, the interpretation of the data with respect to tensile properties of the tested polymer material is beyond the scope of this work.

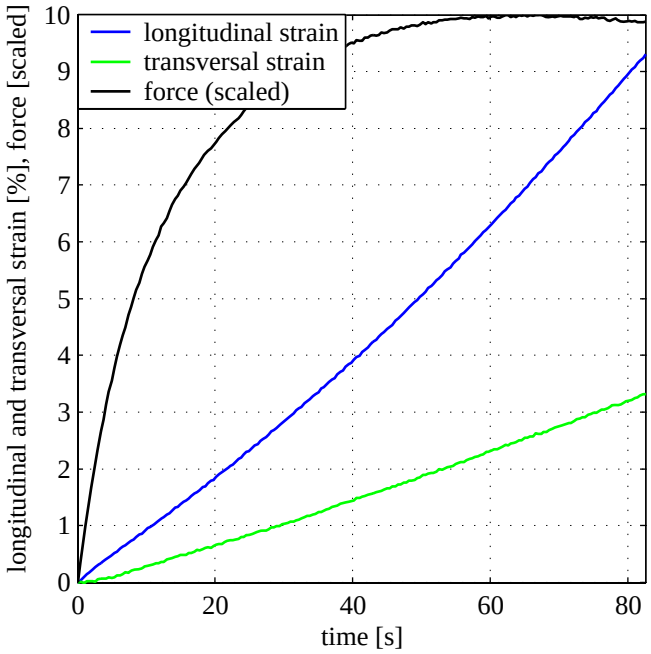

Figure 7.7: Typical results of a tensile test measured with the video-extensometer system. The data is published with permission of the Polymer Competence Center Leoben GmbH, Leoben, Austria, (http://www.pccl.at).

7.3 Derivation of the Measurement Accuracy

A series of $m = 500$ images of a specimen was acquired with an industrial camera at conditions of repeatability[9]. In Figure 7.8, a sample of the acquired image sequence is depicted.

Figure 7.8: A sample image acquired in the standard acquisition configuration.

Each of the images was evaluated independently and as a result, a population of m measurements of the six sets of data points, $S_1, \ldots, S_6$, was obtained (cf. Figure 7.3). Moreover, the vectors of average point coordinates, $\boldsymbol{\mu}_{S_1}, \ldots, \boldsymbol{\mu}_{S_6}$, as well as the associated covariance matrices, $\Lambda_{S_1}, \ldots, \Lambda_{S_6}$, were computed.

At this point, the $2n$-vector of average point coordinates, $\boldsymbol{\mu}_{S_1}$, as well as the $2n \times 2n$ covariance matrix Λ_{S_1} are shown exemplarily. Therein, n denotes the number of points inherent to the set S_1.

$$\boldsymbol{\mu}_{S_1} = \begin{bmatrix} x_1 & x_2 & \ldots & x_n & y_1 & y_2 & \ldots & y_n \end{bmatrix}^T, \quad \Lambda_{S_1} = \begin{bmatrix} \Lambda_{\boldsymbol{x}} & \mathsf{C}_{\boldsymbol{xy}} \\ \mathsf{C}_{\boldsymbol{xy}}^T & \Lambda_{\boldsymbol{y}} \end{bmatrix}, \tag{7.5}$$

with the $n \times n$ covariance matrices of the x- and y-coordinates:

$$\Lambda_{\boldsymbol{x}} = \begin{bmatrix} \sigma_{x_1}^2 & \sigma_{x_1x_2} & \ldots & \sigma_{x_1x_n} \\ \sigma_{x_1x_2} & \sigma_{x_2}^2 & \ldots & \sigma_{x_2x_n} \\ \vdots & \vdots & \ddots & \vdots \\ \sigma_{x_1x_n} & \sigma_{x_2x_n} & \ldots & \sigma_{x_n}^2 \end{bmatrix}, \quad \Lambda_{\boldsymbol{y}} = \begin{bmatrix} \sigma_{y_1}^2 & \sigma_{y_1y_2} & \ldots & \sigma_{y_1y_n} \\ \sigma_{y_1y_2} & \sigma_{y_2}^2 & \ldots & \sigma_{y_2y_n} \\ \vdots & \vdots & \ddots & \vdots \\ \sigma_{y_1y_n} & \sigma_{y_2y_n} & \ldots & \sigma_{y_n}^2 \end{bmatrix}, \tag{7.6}$$

[9] These comprise (a) the camera as well as the specimen to remain unmoved during the measurements, (b) constant parameters of the measurement setup, such as lighting intensity, lens aperture or exposure time, and (c) ideally constant environmental conditions, such as ambient light or vibrations.

and the $n \times n$ matrix of covariances between the x- and y-coordinates:

$$\mathsf{C}_{\boldsymbol{xy}} = \begin{bmatrix} \sigma_{x_1y_1} & \sigma_{x_1y_2} & \dots & \sigma_{x_1y_n} \\ \sigma_{x_2y_1} & \sigma_{x_2y_2} & \dots & \sigma_{x_2y_n} \\ \vdots & \vdots & \ddots & \vdots \\ \sigma_{x_ny_1} & \sigma_{x_ny_2} & \dots & \sigma_{x_ny_n} \end{bmatrix}. \tag{7.7}$$

Subsequently, all of the extracted sets of data points were evaluated according to the algorithm presented in Section 7.2, resulting in a number of m measurements l_i of the specimen length as well as w_i, the specimen width, $i = 1 \dots m$.

Finally, the average longitudinal and transversal specimen dimensions, μ_l and μ_w, were computed together with the associated variances, σ_l^2 and σ_w^2, and standard deviation values, σ_l and σ_w, respectively. The results obtained are listed in Table 7.1.

7.3.1 Monte-Carlo Simulations

Similar to the analysis performed in Section 4.1.4, the multivariate Gaussian distribution underlying the measurement data was numerically verified by means of Monte-Carlo simulations. For that purpose, $m = 10^4$ sets of data points $S_{1,i}, \dots, S_{6,i}$, $i = 1 \dots m$, were synthetically generated.

At first, the sets of data points were produced incorporating covariance matrices merely holding average coordinate variances along the main diagonal. In order to give an example, the $2n \times 2n$ covariance matrix (n being the number of data points inherent to S_1) utilized to generate the synthetical sets of data points $S_{1,i}$, was specified as:

$$\Lambda_{S_1} = \begin{bmatrix} \Lambda_{\boldsymbol{x}_1} & 0 \\ 0 & \Lambda_{\boldsymbol{y}_1} \end{bmatrix}, \; \Lambda_{\boldsymbol{x}_1} = \begin{bmatrix} \bar{\sigma}_{x_1}^2 & 0 & \dots & 0 \\ 0 & \bar{\sigma}_{x_1}^2 & \dots & 0 \\ \vdots & \vdots & \ddots & \vdots \\ 0 & 0 & \dots & \bar{\sigma}_{x_1}^2 \end{bmatrix}, \; \Lambda_{\boldsymbol{y}_1} = \begin{bmatrix} \bar{\sigma}_{y_1}^2 & 0 & \dots & 0 \\ 0 & \bar{\sigma}_{y_1}^2 & \dots & 0 \\ \vdots & \vdots & \ddots & \vdots \\ 0 & 0 & \dots & \bar{\sigma}_{y_1}^2 \end{bmatrix}. \tag{7.8}$$

The average coordinate variances, $\bar{\sigma}_{x_1}^2 = \sum_{i=1}^{n} \sigma_{x_{1_i}}^2$ and $\bar{\sigma}_{y_1}^2 = \sum_{i=1}^{n} \sigma_{y_{1_i}}^2$, were determined from the coordinate variances $\sigma_{x_{1_i}}^2$ and $\sigma_{y_{1_i}}^2$, $i = 1 \dots n$, which in turn were calculated from the data points extracted in the acquired image sequence. The covariance matrices incorporated to generate the remaining sets of data points, $S_{2,i}, \dots, S_{6,i}$, were determined analogously.

Subsequently, the particular sets of data points were evaluated according to the procedure described in Section 7.2, yielding m results $l_{MC1,i}$ and $w_{MC1,i}$, $i = 1 \dots m$. Furthermore, the average values, $\mu_{l_{MC1}}$ and $\mu_{w_{MC1}}$, were computed together with the associated variances, $\sigma_{l_{MC1}}^2$ and $\sigma_{w_{MC1}}^2$, and standard deviation values, $\sigma_{l_{MC1}}$ and $\sigma_{w_{MC1}}$, respectively. The results obtained are listed in Table 7.1.

The analysis was repeated with a second Monte-Carlo simulation. There, the fully occupied covariance matrices, $\Lambda_{S_1}, \dots, \Lambda_{S_6}$ (cf. Equation (7.5)), were utilized to generate the synthetical sets of data points.

The particular sets of data points were evaluated, yielding a second set of results $l_{MC2,i}$ and $w_{MC2,i}$, $i = 1 \dots m$. Again, the average values, $\mu_{l_{MC2}}$ and $\mu_{w_{MC2}}$, were computed together with the associated variances, $\sigma^2_{l_{MC2}}$ and $\sigma^2_{w_{MC2}}$, and standard deviation values, $\sigma_{l_{MC2}}$ and $\sigma_{w_{MC2}}$, respectively. The results obtained are listed in Table 7.1.

	μ_l, [pixel]	σ_l, [pixel]	μ_w, [pixel]	σ_w, [pixel]
evaluation of measurement data	560.51	0.00699	137.18	0.01807
Monte-Carlo simulation 1	560.58	0.00185	137.24	0.00291
Monte-Carlo simulation 2	560.51	0.00704	137.18	0.01759

Table 7.1: Results obtained by evaluation of the measurement data and the synthetical data of the Monte-Carlo simulations. The results are compared in terms of average values, μ_l and μ_w, as well as standard deviation values, σ_l and σ_w, of the longitudinal and transversal specimen dimensions, l and w, respectively.

Considering the listed results, the following conclusions were drawn:

- The average values of the longitudinal as well as the transversal specimen dimensions, μ_l and μ_w, are in good agreement for all of the three evaluation methods.
- Consistent for all of the three evaluation methods, the longitudinal specimen dimension is subject to lower uncertainty with respect to the transversal specimen dimension. This is a result of the stronger averaging effect caused by the significantly higher number of data points involved in the computation of the longitudinal specimen dimension.
- The standard deviation values resulting from the first Monte-Carlo simulation are significantly smaller than the standard deviation values associated with the results obtained by evaluation of the measurement data. This is a result of the simplified covariance matrices (cf. Equation (7.8)) incorporated in the generation of the data sets for the first Monte-Carlo simulation.
- Comparing the results of evaluating the measurement data and the synthetical data of the second Monte-Carlo simulation, the standard deviation values of the longitudinal as well as the transversal specimen dimension, σ_l and σ_w, are in good agreement. Thus, the fully occupied covariances matrices incorporated in generating the synthetical sets of data points for the second Monte-Carlo simulation, are considered to reflect the statistical nature of the measurement data.

As a result of these investigations, the subsequently presented analytic estimation of the error propagation through the particular steps of the evaluation algorithm is performed on the basis of fully occupied covariance matrices.

7.3.2 First Order Estimation of Error Propagation

In Chapter 4 and Chapter 6, the steps of the evaluation algorithm described in Section 7.2 were analyzed concerning first order estimation of error propagation:

- fitting a pair of parallel lines to two sets of data points (Section 4.2.2);
- calculating the orthogonal distance of two parallel lines (Section 4.2.3.1);
- computing the parameters of a line central to a pair of parallel lines (Section 4.2.3.2);
- calculating the point of intersection of two lines (Section 4.1.3.2); and
- computation of the Euclidean distance between two points (Section 6.2.1).

In order to propagate the uncertainty associated with the sets of data points, represented by the fully occupied covariance matrices, $\Lambda_{S_1}, \ldots, \Lambda_{S_6}$, to the variances associated with the longitudinal and transversal specimen dimension, $\sigma^2_{l_A}$ and $\sigma^2_{w_A}$, the procedures listed above were successively executed. Finally, the standard deviation values, σ_{l_A} and σ_{w_A}, were calculated: $\sigma_{l_A} = 0.00698$ pixel and $\sigma_{w_A} = 0.01807$ pixel.

Comparison of σ_{l_A} and σ_{w_A} with σ_l and σ_w (the results obtained by evaluating the acquired image sequence) as well as with $\sigma_{l_{MC2}}$ and $\sigma_{w_{MC2}}$ (the results of evaluating the synthetical data generated for the second Monte-Carlo simulation, cf. Table 7.1), reveal negligibly small deviations. These result from approximations inherent to the first order estimations of (a) the algorithm for fitting a pair of parallel line to two sets of data points, as well as (b) the non-linear operation of computing the Euclidean distance between two points. For information about further uncertainty analyses, the interested reader is referred to a corresponding publication of the author[17].

7.3.3 The High-Resolution Configuration

Referring to Section 7.1.1, the cameras of the video-extensometer system can be arranged to acquire images in the *high-resolution* configuration (cf. Figure 7.2(b) and Figure 7.4). In order to demonstrate the benefit (in terms of higher measurement accuracy) of this setup with respect to the *standard* configuration, the uncertainty associated with the longitudinal and transversal specimen dimension is determined and compared between the two setups.

In the *high-resolution* configuration, the standard deviation values, $\sigma_l = 0.23\mu m$ and $\sigma_w = 0.47\mu m$, were calculated by evaluating a series of $m = 500$ images acquired under conditions of repeatability (with both of the two cameras involved). In order to compare these metric values with the results obtained in the *standard* configuration, the standard deviation values listed in Table 7.1 are multiplied with a scaling factor f representing the pixel resolution for this setup: $f \approx 72.9\frac{\mu m}{pixel}$. Thus, the standard deviation values obtained for the *standard* configuration are: $\sigma_l = 0.51\mu m$ and $\sigma_w = 1.31\mu m$.

As can be seen, the achievable measurement accuracy in the *high-resolution* configuration is significantly higher than in the *standard* setup.

7.3.4 Computation of Strain Values

The longitudinal strain ε_l is computed by relating the actual specimen length l to the initial specimen length l_0 (cf. Equation (7.4)):

$$\varepsilon_l = \frac{l - l_0}{l_0} = \frac{l}{l_0} - 1. \tag{7.9}$$

In order to estimate the uncertainty (in terms of the variance $\sigma^2_{\varepsilon_l}$) associated with ε_l, the law of first order error propagation is applied:

$$\sigma^2_{\varepsilon_l} \approx \mathsf{J}_{\varepsilon_l} \Lambda_{l,l_0} \mathsf{J}^T_{\varepsilon_l}. \tag{7.10}$$

Therein, a combined covariance matrix Λ_{l,l_0} is incorporated, which holds the variances of the initial and actual specimen length, respectively:

$$\Lambda_{l,l_0} = \begin{bmatrix} \sigma^2_l & 0 \\ 0 & \sigma^2_{l_0} \end{bmatrix}. \tag{7.11}$$

Thus, it is assumed that l and l_0 are uncorrelated. The Jacobian matrix $\mathsf{J}_{\varepsilon_l}$ becomes:

$$\mathsf{J}_{\varepsilon_l} = \begin{bmatrix} \frac{1}{l_0} & -\frac{l}{l_0^2} \end{bmatrix}, \tag{7.12}$$

and the uncertainty associated with ε_l is estimated as:

$$\sigma^2_{\varepsilon_l} \approx \frac{1}{l_0^2} \left(\sigma^2_l + \sigma^2_{l_0} \left(\frac{l}{l_0} \right)^2 \right). \tag{7.13}$$

Considering Equation (7.13), the initial specimen length l_0 as well as σ^2_l, the variance associated with the actual specimen length, are to be considered as being fixed. The variance $\sigma^2_{\varepsilon_l}$ increases quadratically with l, and it increases linearly with $\sigma^2_{l_0}$, the variance associated with the determination of the initial specimen length.

As a result, the uncertainty associated with ε_l can be downsized by reducing $\sigma^2_{l_0}$. This can easily be achieved by averaging l_0 over a number of repeated measurements performed prior to the start of a tensile test. Considering a number of n measurements of the initial specimen length, $l_{0,i}$, $i = 1 \ldots n$, the uncertainty associated with the average value,

$$\bar{l_0} = \frac{1}{n} \sum_{i=1}^{n} l_{0,i}, \tag{7.14}$$

results to:

$$\sigma^2_{\bar{l_0}} = \frac{1}{n^2} \sum_{i=1}^{n} \sigma^2_{l_{0,i}}, \tag{7.15}$$

with $\sigma^2_{l_{0,i}}$ denoting the variances associated with the particular values $l_{0,i}$. Assuming these variances to be approximately equal, i.e. $\sigma^2_{l_{0,1}} \approx \sigma^2_{l_{0,2}} \approx \ldots \approx \sigma^2_{l_{0,n}} \approx \sigma^2_{l_0}$, we obtain:

$$\sigma^2_{\bar{l_0}} \approx \frac{1}{n} \sigma^2_{l_0}. \tag{7.16}$$

These considerations are analogously applicable to transversal strain values.

7.4 Conclusions

The following conclusions, regarding the uncertainty analyses described in this chapter, can be drawn:

- As numerically verified by means of Monte-Carlo simulations, the statistical nature of the sets of data points can be suitably represented by multivariate Gaussian distributions incorporating fully occupied covariance matrices.
- The uncertainty associated with the longitudinal and transversal specimen dimensions was analytically estimated by successive application of the law of first order error propagation to the particular steps of the evaluation algorithm. Comparison with results of evaluating measurement data as well as synthetical data generated for the Monte-Carlo simulations show negligibly small deviations.
- The measurement accuracy achievable with the *standard* and the *high-resolution* acquisition configuration were determined by analyzing series of images acquired at conditions of repeatability. Comparison of the results revealed that measurements performed in the *high-resolution* setup can be evaluated at significantly higher accuracy than in the *standard* configuration.
- As analytically verified by application of the law of first order propagation, a significant reduction of the uncertainty associated with strain values can be achieved by averaging the initial specimen dimensions over a number of repeated measurements.

Chapter 8

Summary, Conclusions and Future Work

8.1 Summary

A video-extensometer system has been developed, which features the following characteristics:

- The video-extensometer system enables measurement of the true specimen deformation. Due to the contactless approach, the material under test is not influenced by the measurement system.
- The system supports simultaneous image acquisition of up to three monochrome camera systems, which can be arranged in a number of different configurations. Thus, the system can be applied to different measurement tasks, e.g. measuring of longitudinal strain of a few % up to several 100%.
- In contrast to mechanical extensometer systems, the presented video-extensometer system supports measurement of the full 3-dimensional specimen deformation. For this purpose, an optical mirror can be mounted laterally to the specimen to provide a view onto the side face of the samples under test.
- The evaluation software of the presented system is flexible concerning both, the shape and the dimension of the specimen as well as the type of material testing applied to the specimen, e.g. tensile tests or compression tests.
- The evaluation algorithm is designed to meet the requirements of measuring material with diverse optical characteristics, e.g. colour, reflectivity, or transparency.
- The measurement accuracy achievable with the video-extensometer system is determined by (1) evaluation of repeated measurements, (2) Monte-Carlo simulation, and (3) analytic estimation through application of the law of first order error propagation. The results obtained with these three techniques are in good agreement.

8.2 Conclusions

The following main conclusions can be drawn from the statistical uncertainty analyses presented in this thesis:

- Three techniques for statistical uncertainty analyses have been investigated:

  1. evaluation of repeated but independent measurements,
  2. Monte-Carlo simulations based on synthetically generated data, and
  3. first order estimation of error propagation.

  The good agreement of the results obtained with these three methods reveal that the analytical approach is a suitable alternative to Monte-Carlo simulations, which may be computationally expensive. This is verified for tasks typically arising in metric vision systems as well as for the image processing algorithm specific for the video-extensometer system.

- The statistical nature of the sets of data points can be suitably modelled by multivariate Gaussian distributions incorporating fully occupied covariance matrices. This is numerically verified through Monte-Carlo simulations, where synthetical data is generated by means of this statistical model. Moreover, the first order estimates of error propagation were computed taking the fully occupied covariance matrices into account.

- The algorithms for fitting a line as well as a pair of parallel lines to sets of noisy data points are investigated in detail concerning first order error propagation. Thereby, the uncertainty associated with the parameters of the fitted lines is determined numerically, i.e. by evaluation of repeated but independent measurements, as well as analytically through successive application of the law of first order error propagation to the particular steps of the evaluation algorithms. The results of the analytically computed uncertainty estimates show negligibly small deviations, which are explained by the approximations inherent to the analytical approach.

- The direct linear transformation (DLT) algorithm for estimating the parameters of plane-to-plane homographies based on point correspondences is analyzed concerning first order error propagation. The uncertainty associated with the homography parameters is determined numerically as well as analytically. A calibration target with a rectangular raster of reference bores is presented. The target is utilized for the calibration procedure of the video-extensometer system. It is shown that the uncertainty associated with the homography parameters may be significantly reduced, if the homography is computed based on a set of points of intersection of the rectangular raster instead of the reference bores center points.

8.3 Future Work

In the author's opinion, there are a number of open issues directly related with the work presented in this thesis:

1. Monte-Carlo simulations are based on synthetical data, produced by means of random number generators. Thereby the matrix square root or alternatively, the Cholesky decomposition of the covariance matrix, which describes the statistical model underlying the data to be generated, is required. Especially for covariance matrices of high dimensions, i.e. $n \gtrsim 500$ with n being the dimensionality of the covariance matrix, these matrix factorizations become instable due to numerical reasons. As a result, alternative approaches such as the *modified Cholesky decomposition* as well as algorithms for estimating Cholesky triangles, would be desirable in these situations [55, 56].

2. All of the uncertainty analyses presented in this thesis are based on the assumption of Gaussian distributed data. Actually, the underlying normal probability density functions were verified with statistical tests, such as the χ^2-test and the Kolmogorov-Smirnov test. However, a more general approach would be to avoid the need for knowledge about the underlying statistical model. This could be achieved by analyzing the spectral characteristics of the acquired measurement data. This information would then act as the starting point for statistical uncertainty analyses.

3. First order error propagation is a popular means for estimating the uncertainty associated with the outcomes of explicit as well as implicit functions, as it enables the application of efficient linear algebra methods. However, when applied to functions non-linear in the input parameters, the law of first order error propagation is analytically not exact. In these situations, alternative approaches such as error propagation of second or higher order, which would lead to the incorporation of tensor algebra techniques, would be desirable.

4. The presented video-extensometer system can be flexibly applied to different types of material testing, among others: tensile tests and compression tests. The specimens utilized for compression tests are initially of cylindrical shape. Depending on the material, the charging construction as well as the friction between the specimen and the charging construction, the contour lines of the samples under test deform into convex, straight or concave shapes. As a result, the images acquired during the compression test could be evaluated by approximation of symmetric spline curves. The development of the image processing algorithms as well as the determination of the uncertainty associated with the results is considered as an open issue.

Appendix A

Derivation of Statistical Quantities

A.1 Variance and Covariance

The variance $V(X)$ of a random variable X can be reformulated as:

$$\begin{aligned} \mathrm{V}(X) &= \mathrm{E}\left((X-\mathrm{E}(X))^2\right) \\ &= \mathrm{E}\left((X-\mathrm{E}(X))\,(X-\mathrm{E}(X))\right) \\ &= \mathrm{E}\left(X^2-2X\mathrm{E}(X)+\mathrm{E}(X)^2\right) \\ &= \mathrm{E}\left(X^2\right)-2\mathrm{E}(X)^2+\mathrm{E}(X)^2 \\ &= \mathrm{E}\left(X^2\right)-\mathrm{E}(X)^2. \end{aligned} \tag{A.1}$$

The covariance $\mathrm{Cov}(X,Y)$ of two random variables X and Y is similarly derived:

$$\begin{aligned} \mathrm{Cov}(X,Y) &= \mathrm{E}\left((X-\mathrm{E}(X))\,(Y-\mathrm{E}(Y))\right) \\ &= \mathrm{E}\left(XY-\mathrm{E}(X)Y-\mathrm{E}(Y)X+\mathrm{E}(X)\mathrm{E}(Y)\right) \\ &= \mathrm{E}\left(XY\right)-2\mathrm{E}(X)\mathrm{E}(Y)+\mathrm{E}(X)\mathrm{E}(Y) \\ &= \mathrm{E}\left(XY\right)-\mathrm{E}(X)\mathrm{E}(Y). \end{aligned} \tag{A.2}$$

A.2 Covariance Matrix

The covariance matrix $V(\boldsymbol{X})$ of a random vector $\boldsymbol{X}$ is reformulated as:

$$\begin{aligned} \mathrm{V}(\boldsymbol{X}) &= \mathrm{E}\left(\left(\boldsymbol{X}-\mathrm{E}(\boldsymbol{X})\right)\left(\boldsymbol{X}-\mathrm{E}(\boldsymbol{X})\right)^T\right) \\ &= \mathrm{E}\left(\boldsymbol{X}\boldsymbol{X}^T-\boldsymbol{X}\mathrm{E}(\boldsymbol{X})^T-\mathrm{E}(\boldsymbol{X})\boldsymbol{X}^T+\mathrm{E}(\boldsymbol{X})\mathrm{E}(\boldsymbol{X})^T\right) \\ &= \mathrm{E}\left(\boldsymbol{X}\boldsymbol{X}^T\right)-\mathrm{E}(\boldsymbol{X})\mathrm{E}(\boldsymbol{X})^T-\mathrm{E}(\boldsymbol{X})\mathrm{E}(\boldsymbol{X})^T+\mathrm{E}(\boldsymbol{X})\mathrm{E}(\boldsymbol{X})^T \\ &= \mathrm{E}\left(\boldsymbol{X}\boldsymbol{X}^T\right)-\mathrm{E}(\boldsymbol{X})\mathrm{E}(\boldsymbol{X})^T. \end{aligned} \tag{A.3}$$

A.3 Sample Variance and Sample Covariance

The sample variance σ_x^2 of a population of samples x_i can be reformulated as:

$$\begin{aligned}
\sigma_x^2 &= \frac{1}{n_R - 1}\left(\sum_{i=1}^{n_R}\left(x_i - \mu_x\right)^2\right) \\
&= \frac{1}{n_R - 1}\left(\sum_{i=1}^{n_R}\left(x_i^2 - 2\mu_x x_i + \mu_x^2\right)\right) \\
&= \frac{1}{n_R - 1}\left(\sum_{i=1}^{n_R}\left(x_i^2\right) - 2\mu_x\left(\sum_{i=1}^{n_R} x_i\right) + n_R\mu_x^2\right) \\
&= \frac{1}{n_R - 1}\left(\sum_{i=1}^{n_R}\left(x_i^2\right) - 2n_R\mu_x^2 + n_R\mu_x^2\right) \\
&= \frac{1}{n_R - 1}\left(\sum_{i=1}^{n_R}\left(x_i^2\right) - n_R\mu_x^2\right) \qquad \text{(A.4)} \\
&= \frac{1}{n_R - 1}\left(\sum_{i=1}^{n_R}\left(x_i^2\right) - \frac{1}{n_R}\left(\sum_{i=1}^{n_R} x_i\right)^2\right). \qquad \text{(A.5)}
\end{aligned}$$

The sample covariance σ_{xy} of two sample populations x_i and y_i is derived analogously:

$$\begin{aligned}
\sigma_{xy} &= \frac{1}{n_R - 1}\left(\sum_{i=1}^{n_R}\left(x_i - \mu_x\right)\left(y_i - \mu_y\right)\right) \\
&= \frac{1}{n_R - 1}\left(\sum_{i=1}^{n_R}\left(x_i y_i - x_i\mu_y - y_i\mu_x + \mu_x\mu_y\right)\right) \\
&= \frac{1}{n_R - 1}\left(\sum_{i=1}^{n_R}\left(x_i y_i\right) - \mu_y\left(\sum_{i=1}^{n_R} x_i\right) - \mu_x\left(\sum_{i=1}^{n_R} y_i\right) + n_R\mu_x\mu_y\right) \\
&= \frac{1}{n_R - 1}\left(\sum_{i=1}^{n_R}\left(x_i y_i\right) - n_R\mu_x\mu_y - n_R\mu_x\mu_y + n_R\mu_x\mu_y\right) \\
&= \frac{1}{n_R - 1}\left(\sum_{i=1}^{n_R}\left(x_i y_i\right) - n_R\mu_x\mu_y\right) \qquad \text{(A.6)} \\
&= \frac{1}{n_R - 1}\left(\sum_{i=1}^{n_R}\left(x_i y_i\right) - \frac{1}{n_R}\sum_{i=1}^{n_R} x_i \sum_{i=1}^{n_R} y_i\right). \qquad \text{(A.7)}
\end{aligned}$$

A.4 Sample Covariance Matrix

The sample covariance matrix $\Lambda_{\boldsymbol{x}}$ of a population of sample vectors $\boldsymbol{x}_i$ is reformulated as:

$$\begin{aligned}
\Lambda_{\boldsymbol{x}} &= \frac{1}{n_R-1}\left(\sum_{i=1}^{n_R}\left(\boldsymbol{x}_i-\boldsymbol{\mu}_{\boldsymbol{x}}\right)\left(\boldsymbol{x}_i-\boldsymbol{\mu}_{\boldsymbol{x}}\right)^T\right)\\
&= \frac{1}{n_R-1}\left(\sum_{i=1}^{n_R}\left(\boldsymbol{x}_i{\boldsymbol{x}_i}^T-\boldsymbol{x}_i{\boldsymbol{\mu}_{\boldsymbol{x}}}^T-\boldsymbol{\mu}_{\boldsymbol{x}}\boldsymbol{x}_i^T+\boldsymbol{\mu}_{\boldsymbol{x}}{\boldsymbol{\mu}_{\boldsymbol{x}}}^T\right)\right)\\
&= \frac{1}{n_R-1}\left(\sum_{i=1}^{n_R}\left(\boldsymbol{x}_i{\boldsymbol{x}_i}^T\right)-\left(\sum_{i=1}^{n_R}\boldsymbol{x}_i\right){\boldsymbol{\mu}_{\boldsymbol{x}}}^T-\boldsymbol{\mu}_{\boldsymbol{x}}\left(\sum_{i=1}^{n_R}\boldsymbol{x}_i^T\right)+n_R\boldsymbol{\mu}_{\boldsymbol{x}}{\boldsymbol{\mu}_{\boldsymbol{x}}}^T\right)\\
&= \frac{1}{n_R-1}\left(\sum_{i=1}^{n_R}\left(\boldsymbol{x}_i{\boldsymbol{x}_i}^T\right)-n_R\boldsymbol{\mu}_{\boldsymbol{x}}{\boldsymbol{\mu}_{\boldsymbol{x}}}^T-n_R\boldsymbol{\mu}_{\boldsymbol{x}}{\boldsymbol{\mu}_{\boldsymbol{x}}}^T+n_R\boldsymbol{\mu}_{\boldsymbol{x}}{\boldsymbol{\mu}_{\boldsymbol{x}}}^T\right)\\
&= \frac{1}{n_R-1}\left(\sum_{i=1}^{n_R}\left(\boldsymbol{x}_i{\boldsymbol{x}_i}^T\right)-n_R\boldsymbol{\mu}_{\boldsymbol{x}}{\boldsymbol{\mu}_{\boldsymbol{x}}}^T\right) \qquad \text{(A.8)}\\
&= \frac{1}{n_R-1}\left(\sum_{i=1}^{n_R}\left(\boldsymbol{x}_i{\boldsymbol{x}_i}^T\right)-\frac{1}{n_R}\sum_{i=1}^{n_R}\boldsymbol{x}_i\sum_{i=1}^{n_R}{\boldsymbol{x}_i}^T\right). \qquad \text{(A.9)}
\end{aligned}$$

Appendix B

Algebraic and Central Moments of Univariate Gaussian Distributions

In the following sections, algebraic as well as central moments of the univariate Gaussian probability density function are derived. The univariate Gaussian distribution is characterized by:

$$\mathcal{N}(x, \mu, \sigma) = \frac{1}{\sigma\sqrt{2\pi}} \mathrm{e}^{-\frac{(x-\mu)^2}{2\sigma^2}}. \tag{B.1}$$

B.1 The First Algebraic Moment

The first algebraic moment of a univariate Gaussian probability density function is defined as:

$$\begin{aligned} \mathrm{M}_1(x) &= \mathrm{E}(x) \\ &= \int_{x=-\infty}^{\infty} x \frac{1}{\sigma\sqrt{2\pi}} \mathrm{e}^{-\frac{(x-\mu)^2}{2\sigma^2}} \,\mathrm{d}x. \end{aligned} \tag{B.2}$$

With the substitution, $z = \frac{x-\mu}{\sigma}$, and thus $x = \sigma z + \mu$ as well as $\mathrm{d}x = \sigma \,\mathrm{d}z$, we obtain:

$$\begin{aligned} \mathrm{M}_1(x) &= \frac{1}{\sigma\sqrt{2\pi}} \int_{z=-\infty}^{\infty} (\sigma z + \mu) \,\mathrm{e}^{-\frac{z^2}{2}} \sigma \,\mathrm{d}z \\ &= \frac{\sigma}{\sqrt{2\pi}} \underbrace{\int_{z=-\infty}^{\infty} z \mathrm{e}^{-\frac{z^2}{2}} \,\mathrm{d}z}_{0} + \frac{\mu}{\sqrt{2\pi}} \underbrace{\int_{z=-\infty}^{\infty} \mathrm{e}^{-\frac{z^2}{2}} \,\mathrm{d}z}_{\sqrt{2\pi}} \\ &= \mu. \end{aligned} \tag{B.3}$$

Notice that the results of the two integrals above are obtained considering the uneven characteristic of the function $z\mathrm{e}^{-\frac{z^2}{2}}$ as well as the following definitions (see Bronstein [7]):

$$\int_{z=0}^{\infty} z^n \mathrm{e}^{-az^2} = \begin{cases} \frac{\sqrt{\pi}\prod_{j=0}^{k-1}(2j+1)}{2^{k+1}a^{\frac{k+1}{2}}} & \dots \quad n = 2k, \\ \frac{k!}{2a^{k+1}} & \dots \quad n = 2k+1, \end{cases} \tag{B.4}$$

$$\int_{z=0}^{\infty} \mathrm{e}^{-a^2z^2} = \frac{\sqrt{\pi}}{2a}, \tag{B.5}$$

which hold for any $k, n \in \mathbb{N}$ and $a > 0$. Here, $\mathbb{N}$ is defined as the set of the natural numbers including 0.

B.2 The Second Central Moment

The second central moment of a univariate Gaussian probability density function is determined as follows:

$$\begin{aligned} \mathrm{M}_2(x) &= \mathrm{E}\left((x-\mu)^2\right) \\ &= \int_{x=-\infty}^{\infty} (x-\mu)^2 \frac{1}{\sigma\sqrt{2\pi}} \mathrm{e}^{-\frac{(x-\mu)^2}{2\sigma^2}} \,\mathrm{d}x \\ &= \frac{1}{\sigma\sqrt{2\pi}} \int_{z=-\infty}^{\infty} \sigma^2 z^2 \mathrm{e}^{-\frac{z^2}{2}} \sigma \,\mathrm{d}z \\ &= \frac{\sigma^2}{\sqrt{2\pi}} \underbrace{\int_{z=-\infty}^{\infty} z^2 \mathrm{e}^{-\frac{z^2}{2}} \,\mathrm{d}z}_{\sqrt{2\pi}} \\ &= \sigma^2. \end{aligned} \tag{B.6}$$

The results are obtained utilizing again the substitution $z = \frac{x-\mu}{\sigma}$, and thus $x = \sigma z + \mu$ as well as $\mathrm{d}x = \sigma \,\mathrm{d}z$. Moreover, the integrals listed in Equation (B.4) are incorporated.

B.3 The Third Central Moment

The third central moment is defined as:

$$\begin{aligned} \mathrm{M}_3(x) &= \mathrm{E}\left((x-\mu)^3\right) \\ &= \int_{x=-\infty}^{\infty} (x-\mu)^3 \frac{1}{\sigma\sqrt{2\pi}} \mathrm{e}^{-\frac{(x-\mu)^2}{2\sigma^2}} \,\mathrm{d}x. \end{aligned} \tag{B.7}$$

Incorporating once again the substitution $z = \frac{x-\mu}{\sigma}$, and thus $x = \sigma z + \mu$ as well as $\mathrm{d}x = \sigma\,\mathrm{d}z$, we obtain:

$$\begin{aligned} \mathrm{M}_3(x) &= \frac{1}{\sigma\sqrt{2\pi}} \int_{z=-\infty}^{\infty} \sigma^3 z^3 \mathrm{e}^{-\frac{z^2}{2}} \sigma\,\mathrm{d}z \\ &= \frac{\sigma^3}{\sqrt{2\pi}} \underbrace{\int_{z=-\infty}^{\infty} z^3 \mathrm{e}^{-\frac{z^2}{2}}\,\mathrm{d}z}_{0} \\ &= 0. \end{aligned} \tag{B.8}$$

The final result is obtained considering the uneven characteristic of the function $z^3\mathrm{e}^{-\frac{z^2}{2}}$.

B.4 The Fourth Central Moment

The fourth central moment is determined as:

$$\begin{aligned} \mathrm{M}_4(x) &= \mathrm{E}\left((x-\mu)^4\right) \\ &= \int_{x=-\infty}^{\infty} (x-\mu)^4 \frac{1}{\sigma\sqrt{2\pi}} \mathrm{e}^{-\frac{(x-\mu)^2}{2\sigma^2}}\,\mathrm{d}x \\ &= \frac{1}{\sigma\sqrt{2\pi}} \int_{z=-\infty}^{\infty} \sigma^4 z^4 \mathrm{e}^{-\frac{z^2}{2}} \sigma\,\mathrm{d}z \\ &= \frac{\sigma^4}{\sqrt{2\pi}} \int_{z=-\infty}^{\infty} z^4 \mathrm{e}^{-\frac{z^2}{2}}\,\mathrm{d}z. \end{aligned} \tag{B.9}$$

Once again the substitution $z = \frac{x-\mu}{\sigma}$, and thus $x = \sigma z + \mu$ as well as $\mathrm{d}x = \sigma\,\mathrm{d}z$, is utilized for this derivation. Now applying integration by parts with:

$$\begin{aligned} u &= z^3, & & & u' &= 3z^2, \\ v' &= z\mathrm{e}^{-\frac{z^2}{2}}, & \text{and further:} & & v &= -\mathrm{e}^{-\frac{z^2}{2}}, \end{aligned}$$

we obtain (incorporating the integral definition specified in Equation (B.4)):

$$\begin{aligned} \mathrm{M}_4(x) &= \frac{3\sigma^4}{\sqrt{2\pi}} \underbrace{\int_{z=-\infty}^{\infty} z^2 \mathrm{e}^{-\frac{z^2}{2}}\,\mathrm{d}z}_{\sqrt{2\pi}} \\ &= 3\sigma^4. \end{aligned} \tag{B.10}$$

Appendix C

The Pseudo-Inverse Matrix

According to Gallier[22], the general definition of the pseudo-inverse A^+ of a rectangular $m \times n$ matrix A,

$$\mathsf{A} = \begin{bmatrix} a_{11} & \dots & a_{1n} \\ \vdots & \ddots & \vdots \\ a_{m1} & \dots & a_{mn} \end{bmatrix}, \tag{C.1}$$

is given as:

$$\mathsf{A}^+ = \mathsf{V}\mathsf{S}^+\mathsf{U}^T. \tag{C.2}$$

Note that the pseudo-inverse A^+ is of dimensionality $n \times m$. The required matrices, V, S and U, are obtained from the singular value decomposition of A, i.e.: $\mathsf{A} = \mathsf{U}\mathsf{S}\mathsf{V}^T$. Therein, the $n \times m$ diagonal matrix S^+ is structured as:

$$\begin{aligned} \mathsf{S}^+ &= \begin{bmatrix} \lambda_1 & 0 & \dots & 0 & 0 & \dots & 0 \\ 0 & \lambda_2 & \dots & 0 & 0 & \dots & 0 \\ \vdots & \vdots & \ddots & \vdots & \vdots & \ddots & \vdots \\ 0 & 0 & \dots & \lambda_n & 0 & \dots & 0 \end{bmatrix} \quad \text{for } m > n, \text{or:} \\ \mathsf{S}^+ &= \begin{bmatrix} \lambda_1 & 0 & \dots & 0 \\ 0 & \lambda_2 & \dots & 0 \\ \vdots & \vdots & \ddots & \vdots \\ 0 & 0 & \dots & \lambda_m \\ 0 & 0 & \dots & 0 \\ \vdots & \vdots & \ddots & \vdots \\ 0 & 0 & \dots & 0 \end{bmatrix} \quad \text{for } m \leq n. \end{aligned} \tag{C.3}$$

Therein, the diagonal elements λ_i, $i = 1 \dots p$, and $p = \min(m, n)$, are:

$$\lambda_i = \begin{cases} \frac{1}{\sigma_i} & \dots \quad i = 1 \dots r, \\ 0 & \dots \quad i = r+1 \dots p, \end{cases} \tag{C.4}$$

where the σ_i denote the singular values of A and r specifies the rank of A. Moreover, U identifies an $n \times n$ matrix, whose columns are the eigenvectors of $\mathsf{A}\mathsf{A}^T$. Analogously, V denotes an $m \times m$ matrix, whose columns represent the eigenvectors of $\mathsf{A}^T\mathsf{A}$.

Given the special case of A being a quadratic, symmetric matrix of dimensionality m. Then, there exists an orthogonal $m \times m$ matrix U, i.e. $\mathsf{U}\mathsf{U}^T = \mathsf{U}^T\mathsf{U} = \mathrm{I}_m$, as well as a diagonal matrix S being structured as:

$$\mathsf{S} = \begin{bmatrix} \lambda_1 & 0 & \dots & 0 & 0 & \dots & 0 \\ 0 & \lambda_2 & \dots & 0 & 0 & \dots & 0 \\ \vdots & \vdots & \ddots & \vdots & \vdots & \ddots & \vdots \\ 0 & 0 & \dots & \lambda_p & 0 & \dots & 0 \\ 0 & 0 & \dots & 0 & 0 & \dots & 0 \\ \vdots & \vdots & \ddots & \vdots & \vdots & \ddots & \vdots \\ 0 & 0 & \dots & 0 & 0 & \dots & 0 \end{bmatrix}, \tag{C.5}$$

such that:

$$\mathsf{A} = \mathsf{U}\mathsf{S}\mathsf{U}^T. \tag{C.6}$$

In this situation, the pseudo-inverse A^+ is computed as:

$$\mathsf{A}^+ = \mathsf{U}\mathsf{S}^+\mathsf{U}^T, \tag{C.7}$$

with:

$$\mathsf{S}^+ = \begin{bmatrix} \frac{1}{\lambda_1} & 0 & \dots & 0 & 0 & \dots & 0 \\ 0 & \frac{1}{\lambda_2} & \dots & 0 & 0 & \dots & 0 \\ \vdots & \vdots & \ddots & \vdots & \vdots & \ddots & \vdots \\ 0 & 0 & \dots & \frac{1}{\lambda_p} & 0 & \dots & 0 \\ 0 & 0 & \dots & 0 & 0 & \dots & 0 \\ \vdots & \vdots & \ddots & \vdots & \vdots & \ddots & \vdots \\ 0 & 0 & \dots & 0 & 0 & \dots & 0 \end{bmatrix}. \tag{C.8}$$

Proof: Following Gallier[22], the pseudo-inverse A^+ of an arbitrary matrix A is characterized by the following four equations, which are commonly known as the Moore-Penrose conditions:

$$\begin{aligned} \mathsf{A}\mathsf{A}^+\mathsf{A} &= \mathsf{A}, && \text{(C.9)} \\ \mathsf{A}^+\mathsf{A}\mathsf{A}^+ &= \mathsf{A}^+, && \text{(C.10)} \\ \left(\mathsf{A}\mathsf{A}^+\right)^T &= \mathsf{A}\mathsf{A}^+, && \text{(C.11)} \\ \left(\mathsf{A}^+\mathsf{A}\right)^T &= \mathsf{A}^+\mathsf{A}. && \text{(C.12)} \end{aligned}$$

Thus, we need to verify these conditions for the quadratic, symmetric matrix A:

Condition 1 **(Equation** (C.9)**):**

$$\begin{aligned} \mathsf{A}\mathsf{A}^+\mathsf{A} &= \left(\mathsf{U}\mathsf{S}\mathsf{U}^T\right)\left(\mathsf{U}\mathsf{S}^+\mathsf{U}^T\right)\left(\mathsf{U}\mathsf{S}\mathsf{U}^T\right) \\ &= \mathsf{U}\underbrace{\mathsf{S}\,\mathsf{S}^+\,\mathsf{S}}_{\mathsf{S}}\mathsf{U}^T \\ &= \mathsf{U}\mathsf{S}\mathsf{U}^T \\ &= \mathsf{A}. \end{aligned} \tag{C.13}$$

Condition 2 **(Equation** (C.10)**):**

$$\begin{aligned} \mathsf{A}^{+}\mathsf{A}\mathsf{A}^{+} &= \left(\mathsf{U}\mathsf{S}^{+}\mathsf{U}^{T}\right)\left(\mathsf{U}\mathsf{S}\mathsf{U}^{T}\right)\left(\mathsf{U}\mathsf{S}^{+}\mathsf{U}^{T}\right) \\ &= \mathsf{U}\underbrace{\mathsf{S}^{+}\,\mathsf{S}\,\mathsf{S}^{+}}_{\mathsf{S}^{+}}\mathsf{U}^{T} \\ &= \mathsf{U}\mathsf{S}^{+}\mathsf{U}^{T} \\ &= \mathsf{A}^{+}. \end{aligned} \tag{C.14}$$

Condition 3 **(Equation** (C.11)**):**

$$\begin{aligned} \left(\mathsf{A}\mathsf{A}^{+}\right)^{T} &= \left(\left(\mathsf{U}\mathsf{S}\mathsf{U}^{T}\right)\left(\mathsf{U}\mathsf{S}^{+}\mathsf{U}^{T}\right)\right)^{T} \\ &= \left(\mathsf{U}\mathsf{S}\mathsf{S}^{+}\mathsf{U}^{T}\right)^{T} \\ &= \mathsf{U}\underbrace{\mathsf{S}^{+}\,\mathsf{S}}_{\mathsf{S}\mathsf{S}^{+}}\mathsf{U}^{T} \\ &= \mathsf{U}\mathsf{S}\mathsf{S}^{+}\mathsf{U}^{T} \\ &= \mathsf{U}\mathsf{S}\mathsf{I}\mathsf{S}^{+}\mathsf{U}^{T} \\ &= \mathsf{U}\mathsf{S}\mathsf{U}^{T}\mathsf{U}\mathsf{S}^{+}\mathsf{U}^{T} \\ &= \mathsf{A}\mathsf{A}^{+}. \end{aligned} \tag{C.15}$$

Condition 4 **(Equation** (C.12)**):**

$$\begin{aligned} \left(\mathsf{A}^{+}\mathsf{A}\right)^{T} &= \left(\left(\mathsf{U}\mathsf{S}^{+}\mathsf{U}^{T}\right)\left(\mathsf{U}\mathsf{S}\mathsf{U}^{T}\right)\right)^{T} \\ &= \left(\mathsf{U}\mathsf{S}^{+}\mathsf{S}\mathsf{U}^{T}\right)^{T} \\ &= \mathsf{U}\underbrace{\mathsf{S}\,\mathsf{S}^{+}}_{\mathsf{S}^{+}\mathsf{S}}\mathsf{U}^{T} \\ &= \mathsf{U}\mathsf{S}^{+}\mathsf{S}\mathsf{U}^{T} \\ &= \mathsf{U}\mathsf{S}^{+}\mathsf{I}\mathsf{S}\mathsf{U}^{T} \\ &= \mathsf{U}\mathsf{S}^{+}\mathsf{U}^{T}\mathsf{U}\mathsf{S}\mathsf{U}^{T} \\ &= \mathsf{A}^{+}\mathsf{A}. \end{aligned} \tag{C.16}$$

As all of the Moore-Penrose conditions are properly fulfilled, we have verified that the pseudo-inverse matrix A^{+} of A can actually be computed according to: $\mathsf{A}^{+} = \mathsf{U}\mathsf{S}^{+}\mathsf{U}^{T}$.

List of Figures

2.1 Illustration of the concept of precision and bias errors by means of an image processing example. . . . 14

3.1 Illustration of the duality principle in the projective plane. Points and lines represent dual geometric objects in the homogeneous point and line space, respectively. . . . 25

3.2 A population of random points with associated confidence ellipses (left) and the population of dual lines with associated dual confidence hyperbolae (right). . . . 34

4.1 A sample of the image series acquired with an industrial camera (left) and the corresponding image of absolute gradient (right). . . . 43

4.2 Confidence envelopes of the line envelopes described by the covariance matrices $\Lambda_{\boldsymbol{l}_{A,1}}$ (left), $\Lambda_{\boldsymbol{l}_{A,2}}$ (central) and $\Lambda_{\boldsymbol{l}_{A,3}}$ (right), opposed to that represented by $\Lambda_{\boldsymbol{l}}$. . . . 47

4.3 An image series was acquired with an industrial camera under conditions of repeatability. A sample of the image series showing an object with two parallel edges (left) and the corresponding image of absolute gradient (right). 54

5.1 A sample image of a calibration target acquired with an industrial camera. The target exhibits a rectangular grid of reference bores with diameters of 1.5mm. The distance between center points of adjacent reference bores is 4mm in each direction. . . . 63

5.2 The center points of the reference bores together with the approximated sets of parallel and orthogonal lines as well as the resulting intersection points. . . . 66

5.3 Comparison of the uncertainty associated with the given center points and the calculated intersection points. Note that the confidence ellipses were plotted incorporating a scaling factor of $f = 1000$. . . . 67

6.1 Relative confidence interval associated with the variance of the first order estimate $\mathrm{T}_1(d)$ as a function of d. . . . 79

7.1 Scheme of the hardware setup realized with the video-extensometer system. The shape of the specimens typically used for tensile tests follows the ISO $527-2$ standard and exhibits an initial rectangular cross-section of $10\times4mm^2$. 89

7.2 Fields of view of the cameras with respect to the specimen for (a) the standard, (b) the high-resolution, and (c) the 3-dimensional acquisition configuration. Note that in the configurations (b) and (c), two cameras are focussing on local regions around the measurement marks. As the testing machine's lower crosshead is moved downwards during the tensile testing, these fields of view are centered at points below the respective measurement marks. 91

7.3 Sample image captured under the *standard* acquisition configuration. The location of the sets of data points is emphasized in magnified local image regions. 92

7.4 Sample images captured under the *high-resolution* acquisition configuration. The location of the sets of data points is emphasized in magnified local image regions. The fields of view of the two cameras are non-overlapping, thus a calibration procedure is required to determine their relative location. 93

7.5 The calibration target (a) utilized to determine the homography matrix, which maps points of the camera's image plane to the front face of the target. The height distribution of the front face was measured by means of a confocal microscope (b). This data provides the starting point to determine the metric coordinates of the reference bore's center points. 95

7.6 Location of the geometric primitives utilized for the evaluation procedure: Three pairs of parallel lines fitted to the sets of data points together with their corresponding central lines, $\boldsymbol{l}_C$, $\boldsymbol{l}_T$ and $\boldsymbol{l}_B$, and the two points of intersection $\boldsymbol{p}_T$ and $\boldsymbol{p}_B$. 96

7.7 Typical results of a tensile test measured with the video-extensometer system. The data is published with permission of the Polymer Competence Center Leoben GmbH, Leoben, Austria, (http://www.pccl.at). 97

7.8 A sample image acquired in the standard acquisition configuration. 98

List of Tables

3.1 Mahalanobis distance values typically utilized for visualizations in the 2- as well as the 3-dimensional space. 31

4.1 Covariance matrices associated with a homogeneous 3-vector of line parameters, determined by Monte-Carlo experiments (left column) and application of first order error propagation (right column). 46

4.2 Comparison of the results of an uncertainty analysis concerning the orthogonal distance between a pair of parallel lines. The average orthogonal distance μ_d as well as the associated variance σ_d^2 were obtained by evaluation of the measurement data, whereas the variance $\sigma_{d_A}^2$ was analytically estimated. 56

5.1 Partial derivatives of the distinct elements $a_{1_{ij}}$ of sub-matrix A_1. 61

5.2 Partial derivatives of the distinct elements $a_{2_{ij}}$ of sub-matrix A_2. 61

5.3 Partial derivatives of the distinct elements $a_{3_{ij}}$ of sub-matrix A_3. 62

5.4 Partial derivatives of the distinct elements $a_{4_{ij}}$ of sub-matrix A_4. 62

6.1 Significance levels p associated with confidence intervals, assuming Gaussian distributed data. 71

6.2 A list of functions $f(e_{x_1}^{k_1}, e_{x_2}^{k_2}, e_{x_3}^{k_3}, e_{x_4}^{k_4})$ with corresponding expectation values. The expectation values were computed by means of the analytical definition of expectation values and integrating out the parameters e_{x_i}. . . 72

6.3 Results of a Monte-Carlo experiment concerning the confidence interval associated with the variance $\mathrm{V}(\mathrm{T}_1(d))$ of the first order Taylor approximation of the Euclidean distance d between two points. 78

6.4 Results of a Monte-Carlo experiment concerning the absolute and relative confidence intervals associated with the covariance matrix of first order estimates of inhomogeneous point coordinates $\mathrm{T}_1(x)$ and $\mathrm{T}_1(y)$. 86

7.1 Results obtained by evaluation of the measurement data and the synthetical data of the Monte-Carlo simulations. The results are compared in terms of average values, μ_l and μ_w, as well as standard deviation values, σ_l and σ_w, of the longitudinal and transversal specimen dimensions, l and w, respectively. 100

Author's Publications

Conference Publications

1. E. Fauster, and P. O'Leary, "Methods of Statistical Uncertainty Analysis Applied to Evaluation Algorithms of a Video-Extensometer System", in *Image Processing: Machine Vision Applications*, Proceedings of IS&T / SPIE 20th Annual Symposium on Electronic Imaging, SPIE Vol. 6813, 2008. Article in press.

2. T. Suesut, P. O'Leary, P. Schalk, E. Fauster, "Real-Time Geometric Surface Inspection", presented at the International Conference on Engineering, Applied Science, and Technology (ICEAST), 2007, Bangkok, Thailand.

3. N. Koller, R. Ofner, P. O'Leary, and E. Fauster, "Optical Servoing for Industrial Surface Machining", in *Machine Vision Applications in Industrial Inspection XIV*, Proceedings of IS&T / SPIE 18th Annual Symposium on Electronic Imaging, SPIE Vol. 6070, pp. 1-11, 2006.

4. E. Fauster, P. Schalk, and P. O'Leary, "Evaluation and Calibration Methods for the Application of a Video-Extensometer to Tensile Testing of Polymer Materials", in *Machine Vision Applications in Industrial Inspection XIII*, Proceedings of IS&T / SPIE 17th Annual Symposium on Electronic Imaging, SPIE Vol. 5679, pp. 187-198, 2005.

5. P. Schalk, E. Fauster, and P. O'Leary, "High-Temperature Video-Extensometry for Material Testing of Refractories", in *Machine Vision Applications in Industrial Inspection XIII*, Proceedings of IS&T / SPIE 17th Annual Symposium on Electronic Imaging, SPIE Vol. 5679, pp. 129-139, 2005.

6. M. Weiss, A. Schiller, P. O'Leary, E. Fauster, and P. Schalk, "*Development of a Distributed Vision System for Industrial Conditions*", Sixth International Conference on Quality Control by Artificial Vision, Gatlingburg, USA: SPIE, 2003.

7. E. Fauster, P. Schalk, and M. Tratnig, "*Calibration Method for Light Sectioning Measurement Systems*", 2nd WSEAS International Conference on Signal, Speech and Image Processing, Skiathos, Greece: WSEAS Press, 2002.

Journal Publication

1. P. Schalk, E. Fauster, P. O'Leary, and M. Weiss, "*Framework for automatic quality control in industrial environments using distributed image processing*", Journal of Electronic Imaging, vol. 13, no. 3, 2004.

Symposium Publications

1. R. Ofner, E. Fauster, P. Schalk, and N. Koller, "*Optische Inspektion für die automatische Bearbeitung von Langprodukten*", Industrielles Symposium Mechatronik, Linz, 2007

2. E. Fauster, N. Koller, R. Ofner, and P. O'Leary, "*Optical Inspection of Steel Bars for Automatic Grinding of Surface Defects*", XXV. Verformungskundliches Kolloquium, Planneralm, Donnersbach, Austria, 2006

3. P. Schalk, M. Weiss, E. Fauster, and P. O'Leary, "*Videoextensometrie als Messverfahren zur Prüfung glühender Werkstoffe*", XXIII. Verformungskundliches Kolloquium, Planneralm, Donnersbach, Austria, 2004.

Technical Papers

1. M. Weiss, A. Schiller, P. O'Leary, E. Fauster, and P. Schalk, "*A Distributed Vision System for Quality Control at a Wire Rolling Mill*", Society of Manufacturing Engineers, USA, 2003.

Oral Presentations

1. Methods of Statistical Uncertainty Analysis Applied to Evaluation Algorithms of a Video-Extensometer System, IS&T / SPIE 20th Annual Symposium on Electronic Imaging, San Jose, California, USA, 2008

2. Optical Inspection of Steel Bars for Automatic Grinding of Surface Defects, XXV. Verformungskundliches Kolloquium, Planneralm, Donnersbach, Austria, 2006

3. Evaluation and Calibration Methods for the Application of a Video-Extensometer to Tensile Testing of Polymer Materials, IS&T / SPIE 17th Annual Symposium on Electronic Imaging, San Jose, California, USA, 2005

4. Calibration Method for Light Sectioning Measurement Systems, 2nd WSEAS International Conference on Signal, Speech and Image Processing, Skiathos, Greece, 2002

References

[1] Dantec Dynamics, Strain and Stress Measurements, 2008. Online available: http://www.dantecdynamics.com.

[2] Fiedler Optoelektronik GmbH, Laserextensometer, 2008. Online available: http://www.fiedler-oe.de.

[3] GOM - Gesellschaft für optische Messtechnik, Industrielle 3D-Messtechnik, 2008. Online available: http://www.gom.com.

[4] Instron Deutschland GmbH, Non-contacting Video Extensometers, 2008. Online available: http://www.instron.de.

[5] Messphysik Materials Testing GmbH, Video Extensometer, 2008. Online available: http://www.messphysik.com.

[6] Steinbichler Optotechnik GmbH, Verformungs- und Schwingungsanalyse, 2008. Online available: http://www.steinbichler.de.

[7] I. N. Bronstein and K. A. Semendjajew. *Taschenbuch der Mathematik*. Verlag Nauka, 25. Auflage, 1991. ISBN: 3-87144-492-8.

[8] J. C. Clarke. Modelling Uncertainty: A Primer. Technical Report 2161/98, Department of Engineering Science, Oxford University, 1998.

[9] A. Criminisi. Modelling and Using Uncertainties in Video Metrology. Report, Department of Engineering Science, University of Oxford, 1997.

[10] A. Criminisi. *Accurate Visual Metrology from Single and Multiple Uncalibrated Images*. PhD Thesis, University of Oxford, 1999.

[11] A. Criminisi, I. Reid, and A. Zisserman. A plane measuring device. *Image and Vision Computing (IVC)*, 17(8):625–634, 1999.

[12] A. Criminisi, I. Reid, and A. Zisserman. Single View Metrology. *International Journal of Computer Vision*, 40(2):123–148, 2000.

[13] G. Csurka, C. Zeller, Z. Zhang, and O. Faugeras. Characterizing the Uncertainty of the Fundamental Matrix. *Computer Vision and Image Understanding*, 68(1):18–36, 1997.

[14] B. Dogan and M. Horstmann. Laser scanner displacement measurement at high temperatures. *The International Journal of Pressure Vessels and Piping*, 80(7):427–434, 2003.

[15] O. Faugeras. *Three-Dimensional Computer Vision*. The MIT Press, Cambridge, Massachusetts, 2001. ISBN: 0-262-06158-9.

[16] O. Faugeras, Q.-T. Luong, and T. Papadopoulou. *The Geometry of Multiple Images*. MIT Press, Cambridge, MA, USA, 2001b. ISBN: 0-262-06220-8.

[17] E. Fauster and P. O'Leary. Methods of Statistical Uncertainty Analysis Applied to Evaluation Algorithms of a Video-Extensometer System. In *Image Processing: Machine Vision Applications*, pages ??–??, San Jose, California, USA, 2008. SPIE Vol. 6813. ISBN: ??

[18] E. Fauster, P. Schalk, and P. O'Leary. Evaluation and Calibration Methods for the Application of a Video-Extensometer to Tensile Testing of Polymer Materials. In *Machine Vision Applications in Industrial Inspection XIII*, pages 187–198, San Jose, California, USA, 2005. SPIE Vol. 5679. ISBN: 0-8194-5652-7.

[19] E. Fauster, R. Steinberger, and Z. Major. Development and Implementation of Non-Contact Strain and Deformation Test Methods for Polymeric Materials and Components. Work package report WPR-S.07-01, Polymer Competence Center Leoben GmbH, 2005.

[20] R. S. Figliola and D. E. Beasley. *Theory and Design for Mechanical Measurements*. John Wiley and Sons Inc., third edition, 2000. ISBN: 0-471-35083-4.

[21] W. Förstner. Uncertainty and Projective Geometry. In E. Bayro-Corrochano, editor, *Handbook of Geometric Computing: Applications in Pattern Recognition, Computer Vision, Neuralcomputing, and Robotics*, pages 493–534. Springer-Verlag, 2005.

[22] J. Gallier. *Geometric Methods and Applications: For Computer Science and Engineering*. Springer Verlag, 2001. ISBN: 0-387-95044-3.

[23] A. Gfrerrer. Computational Geometry in Metric Image Processing, Lecture Notes. Graz, University of Technology, 2003.

[24] G. H. Golub and C. F. V. Loan. *Matrix Computations*. Johns Hopkins Series in the Mathematical Sciences. The Johns Hopkins University Press, third edition, 1996. ISBN: 0-8018-5414-8.

[25] R. C. Gonzalez and R. E. Woods. *Digital Image Processing*. Addison-Wesley, 1993. ISBN: 0-201-60078-1.

[26] C. M. Grinstead and J. L. Snell. *Introduction to Probability*. American Mathematical Society, second edition, 2003.

[27] R. M. Haralick. Propagating Covariance in Computer Vision. In *12'th International Conference on Pattern Recognition*, pages 493–498, Jerusalem, Israel, 1994.

[28] M. Harker. Computation of homographies. In W. Clocksin, A. Fitzgibbon, and P. Torr, editors, *British Machine Vision Conference 2005*, volume 1, pages 310–319, Oxford, UK, 2005.

[29] M. Harker and P. O'Leary. Direct Estimation of Homogeneous Vectors: An Ill-Solved Problem in Computer Vision. In *5th Indian Conference on Computer Vision, Graphics and Image Processing (ICVGIP)*, pages 919–930, Madurai, India, 2006.

[30] M. Harker and P. O'Leary. Fitting Specific Conics to Scattered Data via Explicit Polynomials. In *IEEE 1'st International Conference on Signal and Image Processing*, pages 489 – 494, Karnataka, India, 2006.

[31] M. Harker, P. O'Leary, and P. Zsombor-Murray. Incremental Matrix Orthogonalization with an Application to Curve Fitting. In C. A. Bouman and E. L. Miller, editors, *Computational Imaging III*, pages 354–361, San Jose, California, USA, 2005. SPIE, Volume 5674. ISBN: 9780819456472.

[32] R. Hartley and A. Zisserman. *Multiple View Geometry*. Cambridge University Press, second edition, 2003. ISBN: 0-521-54051-8.

[33] S. Heuel. *Uncertain Projective Geometry*. Lecture Notes in Computer Science. Springer Verlag, 2004. ISBN: 3-540-22029-1.

[34] S. H. Joseph. Unbiased Least Squares Fitting of Circular Arcs. *Graphical Models and Image Processing*, 56(5):424–432, 1994.

[35] K. Kanatani. *Statistical Optimization for Geometric Computation*. Dover Publications Inc., 1996. ISBN: 0-486-44308-6.

[36] F. Klein. *Elementarmathematik vom höheren Standpunkte aus II*. Die Grundlehren der mathematischen Wissenschaften in Einzeldarstellungen, Band 15, 1925. Springer Verlag, Dritte Auflage, Nachdruck 1968, 1925.

[37] N. Koller. *Fully Automated Repair of Surface Flaws using an Artificial Vision Guided Robotic Grinder*. PhD Thesis, University of Leoben, Leoben, Austria, 2007.

[38] P. L'Ecuyer. Uniform Random Number Generators: A Review. In *Winter Simulation Conference*, pages 127–134, 1997. URL: citeseer.ist.psu.edu/106404.html.

[39] P. L'Ecuyer. Random Number Generation. In J. Banks, editor, *Chapter 4 of the Handbook on Simulation*, pages 93–137. Wiley, 1998. URL: citeseer.ist.psu.edu/630842.html.

[40] S. Marple. *Digital Spectral Analysis with Applications*. Prentice-Hall Signal Processing Series. Prentice-Hall, 1987. ISBN: 0-13-214149-3.

[41] J. L. Mundy and A. Zisserman. Appendix – Projective Geometry for Machine Vision. In *Geometric Invariances in Computer Vision*. MIT Press, Cambridge, 1992.

[42] B. Ochoa and S. Belongie. Covariance propagation for guided matching. In *International Workshop on Statistical Methods in Multi-Image and Video Processing*, Graz, Austria, 2006.

[43] R. Ofner. *Three-Dimensional Measurement via the Light-Sectioning Method*. PhD Thesis, University of Leoben, Leoben, Austria, 2000.

[44] P. O'Leary. Fitting Geometric Models in Image Processing using Grassmann Manifolds. In *Machine Vision Applications in Industrial Inspection X*, San Jose, California, USA, 2002.

[45] P. O'Leary, M. Harker, and P. Zsombor-Murray. Direct and least square fitting of coupled geometric objects for metric vision. *IEE Proceedings - Vision, Image, and Signal Processing*, 152(6), 2005.

[46] P. O'Leary and P. Zsombor-Murray. Direct and Specific Least-Square Fitting of Hyperbolae and Ellipses. *Journal of Electronic Imaging*, 13(3):492–503, 2004.

[47] L. Piegl and W. Till. *The NURBS Book*. Monographs in Visual Communication. Springer Verlag, 2nd Edition, 1997. ISBN: 3-540-61545-8.

[48] W. Press, S. Teukolsky, W. Vetterling, and B. Fannery. *Numerical Recipes in C*. Cambridge University Press, Cambridge, 1995. ISBN: 0-521-43108-5.

[49] L. Sachs. *Angewandte Statistik*. Springer Verlag, Achte Ausgabe, 1997. ISBN: 3-540-60494-4.

[50] P. Schalk. *Metric Vision Methods for Material and Product Inspection*. PhD Thesis, University of Leoben, Leoben, Austria, 2007.

[51] H. Schmidt. Was ist Genauigkeit? Zum Einfluß systematischer Abweichungen auf Meß- und Ausgleichungsergebnisse. Technischer Bericht, Geodätisches Institut, RWTH Aachen, 1997.

[52] J. G. Semple and G. T. Kneebone. *Algebraic Projective Geometry*. Oxford University Press, 2005. ISBN: 0198503636.

[53] M. Sonka, V. Hlavac, and R. Boyle. *Image Processing, Analysis, and Machine Vision*. Thomson Publishing, second edition, 1999. ISBN: 0-534-95393-X.

[54] M. Tratnig. *Calibration and Registration Approaches for Light-Sectioning Setups Featuring Small Fields of View*. PhD Thesis, University of Leoben, Leoben, Austria, 2005.

[55] B. Triggs. A New Approach to Geometric Fitting, 1997. Online available: http://citeseer.ist.psu.edu/triggs97new.html.

[56] J. Wang and C. Liu. Generating multivariate mixture of normal distributions using a modified cholesky decomposition. In *Proceedings of the 38th conference on Winter simulation*, pages 342 – 347, Monterey, Ca, USA, 2006. ISBN: 1-4244-0501-7.

[57] Z. Zhao and F. G. Perey. The Covariance Matrix of Derived Quantities and their Combinations. Technical Report ORNL/TM-12106, Oak Ridge National Laboratory, 1992.

[58] Zsombor-Murray and P. Hayes. Grassmannian Reduction of Quadratic Forms. In *17th Canadian Congress of Applied Mechanics (CANCAM 1999)*, pages 313–314, Hamilton, Ontario, Canada, 1999.